Ground state simulations of chains of confined rotors with dipolar interaction

by

Wenxue Zhang

A thesis
presented to the University of Waterloo
in fulfillment of the
thesis requirement for the degree of
Doctor of Philosophy
in
Chemistry - Quantum Information

Waterloo, Ontario, Canada, 2026

© Wenxue Zhang 2026

Examining Committee Membership

The following served on the Examining Committee for this thesis. The decision of the Examining Committee is by majority vote.

Supervisor(s):	Pierre-Nicholas Roy Professor, Dept. of Chemistry, University of Waterloo
External Examiner:	Anne McCoy Professor, University of Washington
Internal-External Member:	Mohamed Hibat-Allah Assistant Professor, Dept. of mathematics, University of Waterloo
Examiner:	Jonathan Baugh Professor, Dept. of chemistry, University of Waterloo
Additional Examiner(s):	Marcel Nooijen Professor, Dept. of chemistry, University of Waterloo

Author's Declaration

This thesis consists of material all of which I authored or co-authored: see Statement of Contributions included in the thesis. This is a true copy of the thesis, including any required final revisions, as accepted by my examiners.

I understand that my thesis may be made electronically available to the public.

Statement of Contributions

Chapter 1 (Introduction): P.-N. Roy provided critical manuscript reviews and structural suggestions.

Chapter 2 (Path Integral Monte Carlo Methodology): This chapter is reproduced based on my published paper "Path integral Monte Carlo in a discrete variable representation with Gibbs sampling: dipolar planar rotor chain". My co-author Shaeer Moeed contributed significantly to the development of the formalisms. P.-N. Roy offered editing guidance, and Prof. Marcel Nooijen provided insightful feedback during a thesis committee meeting.

Chapter 3 (Quantum Critical Behavior): This chapter is reproduced based on my second paper to be published "Quantum critical behavior of chains of hindered dipolar rotors". Shaeer Moeed co-developed the introductory section through active discussion, Hui Li contributed valuable insights regarding ferroelectric properties integrated into the article, and P.-N. Roy provided comprehensive manuscript editing.

Chapter 4 (Stacked Rotor Model): This chapter builds upon the foundational stacked rotor model originally constructed by Tobias Serwatka. P.-N. Roy contributed through detailed technical discussions and editing of the manuscript text.

Abstract

In this work, we investigate the quantum rotational dynamics and phase behavior of a water-confined system characterized by an internal planar rotor model. Inelastic neutron scattering (INS) experiments reveal distinct temperature and momentum transfer dependencies inherent to quantum tunneling, with the tunneling margins delineating a prominent quantum phase transition. To systematically model these phenomena, we implement a theoretical approach on linear chains of planar rotors, comprehensively mapping the system's behavior by sweeping both the sixfold potential strength (V_6) and the inter-rotor interaction strength. Our simulations successfully demonstrate a 1D quantum phase transitions between ordered and disordered phases, while effectively capturing the characteristics of the associated quantum-critical regime. These findings provide crucial insights into the interplay between spatial confinement, pinning potentials, and quantum delocalization in molecular rotor networks.

Acknowledgements

First and foremost, I would like to express my deepest gratitude to my supervisor, Pierre-Nicholas Roy, for his creative ideas and profound source code, extraordinary guidance, continuous support, and encouragement throughout my doctoral research. He played a foundational role in shaping my academic growth, providing invaluable insights at every stage of this project. From helping me define my core research direction to rigorously reviewing my code and manuscripts, P.-N.'s patience and high academic standards have profoundly influenced the way I approach physics and problem-solving. I am truly fortunate to have had the privilege of learning under his mentorship.

I would also like to extend my sincere appreciation to the members of my thesis committee Prof. Marcel Nooijen, Assistant Prof. Mohamed Hibat-Allah, Prof. Jonathan Baugh and external examiners-Prof. Anne McCoy for their invaluable evaluation and generous support. Their collective expertise played a pivotal role in refining the quality and rigor of this work. I am especially grateful for their constructive discussions, which helped me clarify complex concepts, identify logical errors, and address critical gaps in my analysis. Furthermore, their extraordinary patience in introducing foundational background knowledge in areas where I was initially unfamiliar has greatly broadened my scientific horizons. Secondly, I would acknowledge the rest of the Roy's group, Dr. Tobias Serwatka, Estevao De Oliveira, and Shaeer Moeed for developing such a genius simulation field and valuable discussion we had about quantum simulation techniques during the PhD program. I would like to thank Senior Doc. Ruiqi Li for helping to promote the understanding of the formula. Their constructive criticism, intellectual generosity, and dedication have left a lasting mark on both this dissertation and my development as an independent researcher.

At last I would like to express my sincere gratitude to my mother for taking care of my daily life while writing this thesis. As well as my group members Megan Dawson, Azharuddin Alfaz Sarfraz Mohammed, Nithin Aaron and Jacob Chausse for their continued encouragement. Thank you all for your time, dedication, and invaluable guidance.

Use of Artificial Intelligence Disclosure

I acknowledge the use of Generative Artificial Intelligence and Large Language Models (LLMs) in the preparation of this thesis. Specifically, ChatGPT, Claude, and Gemini were used for the following purposes:

- **Language Refinement and Proofreading**: LLMs were used exclusively as editing aids to correct grammar, spelling, and phrasing. AI-generated suggestions were critically reviewed and revised to ensure academic rigor and accurately reflect my thoughts.
- **Ideation and Methodological Framing**: LLMs were utilized to support brainstorming and assist in articulating and connecting research hypotheses and questions.
- **Data and Visualization Assistance**: Gemini was additionally employed to assist with basic data handling and initial image processing tasks.

All underlying research concepts, theoretical developments, computational implementations, data analysis, and conclusions remain entirely the original work of the author.

Summary of AI Tools and Versions Used

Model/Version	Contribution
ChatGPT-4o (May 22nd Version)	Grammar and spelling correction, text proofreading
Claude Sonnet 4.6	Brainstorming and hypothesis formulation
Gemini 1.5 Pro	Brainstorming, initial data processing, and image processing

Dedication

This is dedicated to the one I love.

Table of Contents

Examining Committee Membership ii

Author's Declaration iii

Statement of Contributions iv

Abstract v

Acknowledgements vi

Use of Artificial Intelligence Disclosure vii

Dedication viii

List of Figures xiii

List of Tables xvii

List of Abbreviations xviii

1 Introduction 1

1.1 Quantum Mechanics for Planar Rotor 3

1.1.1 Hamiltonian and free rotor propagator . . . 3
1.1.2 Angular-momentum and ladder operators . . . 5
1.1.3 Six-fold potential . . . 6
1.2 Exact Diagonalization . . . 8
1.3 Density Matrix Renormalization Group . . . 9
1.3.1 Singular Value Decomposition(SVD) . . . 10
1.3.2 Matrix Product States (MPS) Formulation . . . 13
1.3.3 The Sweep Algorithm and Application Scenarios . . . 13
1.4 Path Integral Monte Carlo . . . 14
1.4.1 Path Integral Ground States . . . 19
1.4.2 Discrete Variable Representation . . . 20
1.5 Outline of this thesis . . . 21

2 Path integral Monte Carlo in a discrete variable representation with Gibbs sampling: dipolar planar rotor chain 23

2.1 Introduction . . . 24
2.2 Methodology . . . 26
2.2.1 Dipolar planar Rotor Chain . . . 26
2.2.2 Path Integrals For Rotors . . . 27
2.2.3 PIGS Estimators . . . 30
2.2.4 Grid Representation: from Path Integrals to Path Sums . . . 32
2.2.5 Gibbs Sampling The Many Body Distribution . . . 33
2.3 Results and Discussion . . . 35
2.3.1 Imaginary Time Step Convergence . . . 36
2.3.2 Reciprocal Temperature Convergence . . . 37

2.3.3 Many-Body Extension . . . 37
2.3.4 Correlation analysis . . . 38
2.3.5 Beyond 1d lattices and Nearest Neighbor Interactions . . . 39
2.4 Concluding Remarks . . . 41

3 Quantum critical behavior in chains of hindered dipolar planar rotors 51
3.1 Introduction . . . 52
3.2 Theory . . . 54
3.2.1 System Hamiltonian . . . 54
3.2.2 Estimators . . . 56
3.3 Results and Discussion . . . 59
3.3.1 Monomer . . . 59
3.3.2 Longer chains: $N = 50$ . . . 62
3.3.3 Connection to beryl parameters . . . 68
3.4 Concluding Remarks . . . 70

4 Orientational ordering of stacked chains of dipolar rotors in a hexagonal crystal field 71
4.1 Introduction . . . 72
4.2 The model and its symmetry . . . 75
4.2.1 System Hamiltonian . . . 75
4.2.2 Momentum representation . . . 77
4.2.3 Residual symmetry . . . 77
4.3 Results . . . 78
4.3.1 Two rotors: exact diagonalization . . . 78

4.3.2 Longer chains: DMRG 82
4.3.3 Connection to beryl parameters 86
4.4 Concluding Remarks 88

5 Conclusions **90**

5.1 Future Work 93
5.1.1 Finite-size scaling 93
5.1.2 Finite-temperature simulations 95
5.1.3 Extension toward a three-dimensional beryl model 97

References **101**

List of Figures

1.1 A general schematic diagram of dipole-dipole interaction 4

2.1 Schematic representation of a chain of equally spaced planar rotors. 26

2.2 Convergence of the DVR-NMM E_0 with τ compared to ED results with maximum number of DVR grid points $L = 11$, $\beta = 10.0$ and $g = 0.6$ for $N = 2$ (top panel). Fit of the $\tau > 0.17$ results and extrapolation to $\tau = 0$ (bottom panel). 43

2.3 Same as Fig. 2.2 for $N = 3$ here. 44

2.4 Convergence of the DVR-NMM E_0 with β compared to ED for $N = 2$ and $g = 1.0$. The NMM results were computed by fitting a sequence of seven DVR-NMM estimates corresponding to $\tau_t = 0.18 + 0.01t$ for $0 \leq t \leq 7, t \in \mathbb{Z}$ using: $E_\tau = E_0 + a\tau^2 + b\tau^4$. $\beta = 4.0$ appears to be sufficient for convergence. We use $\beta = 10.0$ for our analysis (highlighted in the figure). 45

2.5 Ground state energy as a function of the coupling strength g computed using NMM for $N = 2$ and $N = 3$. The solid lines indicate the ED results while the points specify the NMM estimates (evaluated by extrapolating E_0 NMM estimates for small τ to 0). In both cases, the τ-extrapolated DVR-NMM results converge to the ED results for all $g \in (0.1, 2.0)$. 46

2.6 Ground state energy for $N = 100$, $P = 49$ computed using PIGS with DVR-Gibbs sampling. DMRG results plotted for comparison. 47

2.7 Correlation for $N = 100$, $P = 49$ computed using PIGS with DVR-Gibbs sampling. DMRG results are plotted for comparison. 48

2.8 Angular distributions of the middlde beads (top panel) and end beads (bottom panel) for $N = 100$ with interactions strengths $g = 0.1, 0.5, 1.0$. 49

2.9 Markov chain autocorrelation for the M-H and Gibbs sampling algorithms computed using the orientational correlation for $g = 0.1$ (left panel), $g = 0.5$ (middle panel) and $g = 1.0$ (right panel). All three simulations used $N = 100$, $P = 48$ and 50000 simulation steps. 50

3.1 Schematic of a coplanar chain of dipolar planar rotors, each subject to a six-fold hindering potential. 54

3.2 Energy levels of a single rotor in a six-fold potential with the barrier height $A = 20$; Ω_i denotes the degeneracy of each level. Based on the convergence tests, $m_{\max} = 16$ is used. 60

3.3 Number of states below the barrier (n_{bb}) as a function of the six-fold (reduced) barrier height A. 61

3.4 Von Neumann entropy $S_{\rm vN}$ as a function of g for $A = 0, 20, 40, 60, 80$, and $N = 50$. 63

3.5 Binder cumulant U_x as a function of the dipolar coupling g for $A = 0, 20, 40, 60, 80$ and $N = 50$. 64

3.6 Critical coupling g_c as a function of the reduced barrier height A. Symbols: g_c from the maximum gradient of the Binder ratio at $N = 50$ (Fig. 3.5). Solid line: the scaling form $g_c = a\,\Delta(A)$ of Eq. (3.14) with $a = 0.49$, where $\Delta(A) = E_1 - E_0$ is the tunneling splitting of the monomer Hamiltonian of Eq. (3.3). The $A = 0$ point is not included in the fit; the form nevertheless recovers the free-rotor value $g_c \approx 1/2$ there, since $\Delta(0) = 1$. The shaded band marks the beryl barrier range $A \approx 16$–18 from inelastic neutron scattering,[45] where the fit gives $g_c \approx 0.44$. 65

3.7 Critical coupling g_c as a function of the inverse reduced barrier height $1/A$. Symbols: g_c extracted from the maximum gradient of the Binder ratio at $N = 50$ (Fig. 3.5). Solid line: the single-parameter form $g_c = a\,\Delta(A)$ with $a = 0.49$, where $\Delta(A) = E_1 - E_0$ is the tunneling splitting of the monomer Hamiltonian of Eq. (3.3). The line extrapolates the phase boundary at both ends: for $A \to \infty$ ($1/A \to 0$) the splitting, and with it g_c, vanishes exponentially, while for $A \to 0$ ($1/A \to \infty$) it approaches the free-rotor limit $g_c = 1/2$ (dashed line), since $\Delta(0) = 1$ exactly. The shaded band marks the barrier range $A \approx 16$–18 inferred for water in beryl from inelastic neutron scattering,[45] for which the scaling form gives $g_c \approx 0.43$. 67

4.1 Schematic of the stacked chain, each panel showing one rotor of the stack viewed along the channel axis. The dipole of rotor i is the in-plane unit vector $(\hat{x}_i, \hat{y}_i) = (\cos\phi_i, \sin\phi_i)$, drawn as an arrow. Left: the free chain, in which the rotor may point in any direction and the dipolar coupling alone acts, leaving the continuous U(1) symmetry unbroken. Right: the same chain with the six-fold crystal field superimposed, whose six minima confine the dipole towards the edges of the hexagonal cage and reduce U(1) to $\mathbb{Z}_6$. 74

4.2 Exact results for two rotors at barrier heights $A = 20$, 40 and 60: (a) ground-state energy E_0, (b) entanglement entropy S_{vN} across the single bond, and (c) Binder ratio U_x of the staggered polarization, against the dipolar coupling g. Dashed lines indicate the ordered-phase values $\ln 6$ and $1/2$. 80

4.3 The six largest Schmidt values λ_n across the bond of the two-rotor chain at $A = 60$, against g. The dashed line marks $1/6$. The weights approach a common value in the pattern 1–2–2–1 λ_2 and λ_3 coincide, as do λ_4 and λ_5, and the markers of each degenerate pair are offset along g so that both remain visible. 81

4.4 Ground-state energy E_0, entanglement entropy S_{vN} at the central bond, and Binder ratio U_x of the staggered polarization, against the dipolar coupling g for $A = 20$, 40 and 60 at $N = 10$. Dashed lines mark $\ln 6$ and $1/2$. 84

4.5 The six largest Schmidt values at the central bond against g, for $A = 60$ at $N = 10$. The dashed line marks 1/6. As in the two-rotor case, the weights approach a common value in the pattern 1–2–2–1. 85

5.1 Periodically arranged water molecules in beryl of cross-section perpendicular to the cavity channel. 94

5.2 Periodically arranged water molecules in beryl of cross-section horizontal to the cavity channel. 94

5.3 Schematic diagram of hexagonal beryl crystal cavity shows a cross-section along the channel direction. 98

5.4 The potential well inside a single cavity of beryl is calculated in CP2K with the PBE functional and the 6-31(G) basis set. 99

List of Tables

3.1 Convergence of the single-rotor tunneling splitting $\Delta = E_1 - E_0$ with respect to the size of the angular-momentum basis. Values obtained at $m_{\max} = 16$ are compared with converged results ($m_{\max} = 90$). 59

3.2 Reported values of the in-plane orientational barrier for type-I water in beryl. The different methods extract different quantities (see text). For orientation, 1 meV ≈ 8.07 cm$^{-1} \approx 11.6$ K. 66

4.1 Approach of the two-rotor ground state to the ordered limit. g_S and g_U are the couplings at which the entanglement entropy and the Binder ratio first come within 1% of $\ln 6$ and $1/2$. The last two columns give their values at the largest coupling computed, $g_{\max}$. 79

4.2 Couplings at which the entanglement entropy and the Binder ratio of the ten-rotor chain first come within 1% of $\ln 6$ and $1/2$, with their values at the largest coupling computed. The corresponding two-rotor couplings from Table 4.1 are repeated for comparison. 83

4.3 Critical coupling g_c of the stacked chain at $N = 10$, taken from the steepest gradient of the Binder ratio. Comparison is made with the coupling $g = 7.2$ estimated for water in beryl. 87

List of Abbreviations

1D one-dimensional 13, 14, 98

3D three-dimensional 98

CNT carbon nanotube 1, 90

DFT Density Functional Theory 3, 90, 98, 99

DMC Diffusion Monte Carlo 14, 16

DMRG Density Matrix Renormalization Group 1, 3, 9, 10, 12–14, 22, 90–92, 95, 97, 98

DVR Discrete Variable Representation 2, 20, 21, 90, 91

ED Exact Diagonalization 3, 8, 9, 19, 91

FID Free Induction Decay 99

HPC high-performance computing 90

MC Monte Carlo 98

MD Molecular Dynamics 1, 2, 90

MH Metropolis-Hastings 2, 90, 91

MPS Matrix Product State 13, 15

NMM Numerical Matrix Multiplication 91

NQE Nuclear Quantum Effect 2, 3

PIGS Path Integral Ground State 2, 3, 19, 20, 90, 98

PIMC Path Integral Monte Carlo 3, 16, 19, 21, 90, 91, 93, 95, 97, 98

QMC Quantum Monte Carlo 16, 95

QPT Quantum Phase Transition 22

RB-DMC rigid-body Diffusion Monte Carlo 16

SVD Singular Value Decomposition 10–13, 15

SWCNT single-walled carbon nanotube 1

Chapter 1

Introduction

Spectral analysis indicates that, in confined environments, the properties of water are altered by the embedded substrate, which reduces molecular degrees of freedom and causes surprising quantum behavior.[1–4] Among these phenomena, what most captivated us is the ferroelectric phase observed in confined water molecules. The goal of this thesis is to develop and test methods for chains of confined rotors and to learn their limitations. Also in order to observe the nature of the symmetry breaking, we adapted Density Matrix Renormalization Group (DMRG) for the coplanar and stacked rotor chains. Some of the molecules can remain aligned in a certain orientation after the external electric field is withdrawn. The collective structural, dynamical and entanglement behaviors are abnormal compared with those in bulk states. For example, water confined within a single-walled carbon nanotubes (SWCNTs) self-assembles into a unique tubular n-gon ice structure, which is a highly correlated collective phase.[5] Accordingly, properties such as the vibrational density of states and the optical conductivity of water trapped in beryl have also been studied and exhibit distinct absorption peaks compared with liquid water.[3,6,7] This suggests that beryl can serve as a platform for modeling and studying various features including dipole coupling, quantum tunneling and symmetry breaking. As a powerful computational paradigm, Molecular Dynamics (MD) simulations are particularly well-suited for analyzing the physical trajectories and statistical mechanics of molecular systems, such as water molecules confined within carbon nanotube (CNT).[5,8]

Previous classical MD simulations have shown that ice nanotubes with an odd number of faces can exhibit spontaneous ferroelectric polarization along the tube axis under the geometric constraints of the "ice rule".[9–14] Pure single-particle quantum eigenstates discovered in embedded fullerenes[15–22] serve as an ideal, hydrogen-bond-free physical counterpart to an isolated rotor. Crucially, quantum nuclei affect the structure in a manner similar to that of rising temperature, resulting from the restoration of the complete hydrogen-bond network during the freezing process. However, nature is fundamentally quantum. When classical methods fail, it becomes necessary to treat the nuclei quantum mechanically by including Nuclear Quantum Effects (NQEs).[23,24] Recently, researchers have applied empirical force fields to "open-path" integral molecular dynamics methods to calculate the momentum distributions of protons in ice and water.[25,26] Although the calculated distributions agree with the experimental results in many aspects–the faster decay in ice reflects the redshift of the OH stretching frequency—they fail to reproduce the shorter tails observed in ice, suggesting that the empirical potential lacks transferability.[27–29]

Furthermore, how to use these properties to encode and decode qubits in rotor chains of water confined in beryl is a more compelling question for us. Through our research we know that the competition between quantum tunneling and dipolar coupling plays out as a different variation on the same fundamental theme: competition between the kinetic and potential energy. Suppose there is a critical coupling g_c that separates the tunneling-dominated phase from the dipolar-coupling-dominated phase. When $g < g_c$, quantum tunneling dominates the system dynamics over the hexagonal hindrance, and water behaves as a tunneling state (disordered phase) with a $\mathbb{Z}_2$ symmetry. In contrast, when $g > g_c$, the system enters an ordered phase: for the coplanar chain the broken symmetry is the discrete $\mathbb{Z}_2$, while for the stacked chain the relevant symmetry is the continuous $\mathbb{U}(1)$.

This thesis systematically investigates the interactions between molecular rotation, NQE, and confining geometries.[9,18,29–38] Earlier Path Integral Ground State (PIGS) simulations used continuous angles with Metropolis-Hastings (MH) sampling.[31,32,39–42] In this thesis, we developed PIGS with the Discrete Variable Representation (DVR) grid and Gibbs (rejection-free) sampling. By adapting and applying advanced computational methods capable of explicitly handling the coupling of translational and rotational degrees of freedom, we provide a rigorous quantum mechanical foundation for ferroelectricity in one-

dimensional nanotubes.[6,10,43] In addition to thermodynamic characteristics, NQEs is also of great significance for explaining spectroscopy, tunneling effects, and collective phenomena.[28,29] In advanced modern ab initio simulations, the electronic structure of molecules is calculated "in real time" using Density Functional Theory (DFT). To understand NQE, the main existing methods include Exact Diagonalization (ED), DMRG, Path Integral Monte Carlo (PIMC) and PIGS.

1.1 Quantum Mechanics for Planar Rotor

1.1.1 Hamiltonian and free rotor propagator

According to quantum chemistry,[44] the Hamiltonian of a given system $\hat{H}$ contains translational, rotational and vibrational kinetic-energy operators and the potential.

$$\hat{H} = \hat{T}^{trans} + \hat{T}^{rot} + \hat{T}^{vib} + \hat{V} \tag{1.1}$$

Neglecting $\hat{T}^{trans}$ and $\hat{T}^{vib}$, only the rotational kinetic energy remains. When the radius is fixed, the orientation is defined only by the angle of rotation ϕ, and the kinetic energy operator takes the following form:

$$\hat{T}^{rot} = -B\frac{\partial^2}{\partial\phi^2} \tag{1.2}$$

where $B = \hbar^2/(2I)$ is the rotational constant and I is the moment of inertia. We first consider the free rotation of a single planar rotor, confined to the xy-plane and rotating about the z-axis. The planar rotor is equivalent to a particle on a ring, whose normalized eigenfunction is given by Eq.(1.3):

$$\Psi_m(\phi) = \frac{1}{\sqrt{2\pi}}e^{im\phi} \tag{1.3}$$

A dipole in physics or chemistry refers to any system or object that has two opposite and equal charges separated by a distance. When two dipoles are close together, the dipole-dipole potential favours aligned configurations. If many dipoles align to the same direction,

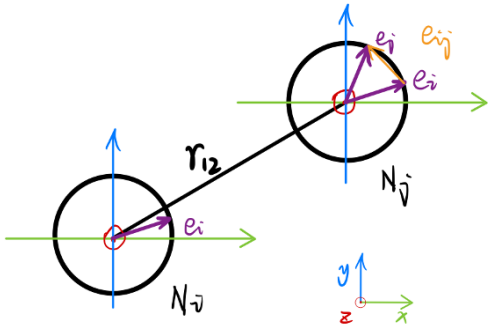


Figure 1.1: A general schematic diagram of dipole-dipole interaction

they form a ferroelectric phase. We focus on only two dipoles as the simplest model. For two rotors with the same dipole moment μ, with unit orientations e_i and e_j at angles θ_1 and θ_2 with respect to the x-axis, separated by r_{ij}, the potential energy of the two dipoles has the following form:

$$\hat{V}_{ij} = (\frac{\mu^2}{4\pi\epsilon_0})(\frac{\cos\theta_{12} - 3\cos(\theta_1)\cos(\theta_2)}{|r_i - r_j|^3}) \tag{1.4}$$

where the θ_{12} is the angle difference of the two dipoles. From the definition of the dot product, $\cos\theta_{12}$ can be written as $\frac{e_i \cdot e_j}{|e_i||e_j|}$. Since these are unit vectors, as Fig. 1.1 shows, the dipolar interaction between dipoles e_i and e_j becomes:

$$\hat{V}_{ij} = (\frac{\mu^2}{4\pi\epsilon_0})(\frac{\vec{e_i} \cdot \vec{e_j} - 3(\vec{e_i} \cdot \vec{e_{ij}})(\vec{e_j} \cdot \vec{e_{ij}})}{|r_i - r_j|^3}) \tag{1.5}$$

In the above equation, e_{ij} denotes the unit vector along the line joining dipoles i and j. The direction joining the dipoles is defined as:

$$\hat{e}_{ij} = \frac{(r_i - r_j)}{|r_i - r_j|} \tag{1.6}$$

In the geometry of the coplanar chain, the two dipoles lie in a common plane and the separation vector points along the x-axis, so that $\hat{e}_{ij} = \hat{x}$. The projections onto the separation direction are then simply the x-components of the unit orientation vectors,

$\vec{e}_i \cdot \hat{e}_{ij} = x_i$ and $\vec{e}_j \cdot \hat{e}_{ij} = x_j$, while the dot product of the two orientations is $\vec{e}_i \cdot \vec{e}_j = x_i x_j + y_i y_j$. Substituting these into the general form above, the interaction simplifies to:

$$\begin{aligned} \hat{V}_{ij} &= \frac{\mu^2}{4\pi\epsilon_0 R^3}\left(\vec{e}_i \cdot \vec{e}_j - 3\, x_i x_j\right) \\ &= \frac{\mu^2}{4\pi\epsilon_0 R^3}\left(x_i x_j + y_i y_j - 3\, x_i x_j\right) \\ &= \frac{\mu^2}{4\pi\epsilon_0 R^3}\left(y_i y_j - 2\, x_i x_j\right) \end{aligned} \tag{1.7}$$

where $R = |r_i - r_j|$ is the distance between the two dipoles. With $x_i = \cos\phi_i$ and $y_i = \sin\phi_i$, the angular factor becomes $\sin\phi_i \sin\phi_j - 2\cos\phi_i \cos\phi_j$, which is the coplanar form used in Chapters 2 and 3; the prefactor $\mu^2/(4\pi\epsilon_0 R^3)$ is absorbed there into the dimensionless coupling g.

1.1.2 Angular-momentum and ladder operators

Before we dive into the details of the method, we propose some of the notation that may be included in later Chapters. Firstly, we introduce the Orbital angular momentum (OAM) operators in angular basis representation:

$$\hat{L}_i \left|m\right\rangle = m_i \left|m_i\right\rangle \tag{1.8}$$

while the raising/Lowering operators:

$$\hat{E}_i^{\pm} \left|m_i\right\rangle = \left|m_i \pm 1\right\rangle \tag{1.9}$$

where in the above equation, the $|m\rangle$ is the angular basis in Dirac notation. What we are interested in here is the dipole-dipole interaction.

A ladder operator in quantum mechanics acts on a state and increases or decreases the eigenvalue of another operator. Suppose that two operators $\hat{X}$ and $\hat{E}$ have the commutation relation:

$$[\hat{E}, \hat{X}] = \hat{E}\hat{X} - \hat{X}\hat{E} = c\hat{X} \tag{1.10}$$

for some scalar c, if $|n\rangle$ is an eigenstate of $\hat{E}$ with eigenvalue equation

$$\hat{E}\,|n\rangle = n\,|n\rangle \tag{1.11}$$

Then, the operator $\hat{X}$ acts on $|n\rangle$ such that the eigenvalue shifts by c.

$$\begin{aligned}\hat{E}\hat{X}\,|n\rangle &= \left(\hat{X}\hat{E} + [\hat{E},\hat{X}]\right)|n\rangle \\ &= \hat{X}\hat{E}\,|n\rangle + [\hat{E},\hat{X}]\,|n\rangle \\ &= \hat{X}n\,|n\rangle + c\hat{X}\,|n\rangle \\ &= (n+c)\hat{X}\,|n\rangle\end{aligned}$$

In other words, if $|n\rangle$ is an eigenstate of $\hat{E}$ with eigenvalue n, then $\hat{X}\,|n\rangle$ is also an eigenstate of $\hat{E}$ with eigenvalue $n+c$, unless $\hat{X}\,|n\rangle = 0$. The operator $\hat{X}$ is a raising operator for E if c is real and positive, and $\hat{X}$ is a lowering operator for E if c is real and negative. In our case of $\hat{E}^{\pm}$, $c = 1$. Next, we can derive from our dipole-dipole interaction using the property of ladder operator by substituting $x = \frac{E^+ + E^-}{2}$ and $y = \frac{E^+ - E^-}{2i}$ in V_{ij}:

$$\hat{V}_{ij} = \frac{\mu^2}{4\pi\epsilon_0}\Big[\frac{E_i^+ - E_i^-}{2i}\frac{E_j^+ - E_j^-}{2i} - 2\frac{E_i^+ + E_i^-}{2}\frac{E_j^+ + E_j^-}{2}\Big] \tag{1.12}$$

$$= -\frac{\mu^2}{4\pi\epsilon_0}\frac{(3E_i^+E_j^+ + E_i^+E_j^- + E_i^-E_j^+ + 3E_i^-E_j^-)}{4} \tag{1.13}$$

1.1.3 Six-fold potential

Having established the form and consequences of the dipole interaction, we now turn to a separate ingredient of the model. As mentioned in the introduction, water molecules naturally move within confined frameworks in nature, such as in beryl and cordierite. One of their key characteristics is that the water molecules experience a sixfold potential field resulting from sixfold symmetry of the crystal skeleton. Unlike the dipolar term, which couples different degrees of freedom through an interaction, this contribution is a local anisotropy defined at each site individually. Its role is therefore conceptually distinct and

is introduced separately through a cos function. We emphasize how it is derived from first principles with Dirac notation. Recall the Euler's equation:

$$e^{i\phi} = \cos(\phi) + i\sin(\phi) \tag{1.14}$$

similarly, it is obvious that:

$$e^{-i\phi} = \cos(\phi) - i\sin(\phi) \tag{1.15}$$

And in $|m\rangle$ basis, it turns to:

$$e^{im\phi} = \cos(m\phi) + i\sin(m\phi) \tag{1.16}$$

The above is the case of the free rotors. But the beryl channel presents a six-fold symmetric potential to the water dipole.[1,45] Therefore, we model it by an on-site potential h_V that applies a six-fold potential to each rotor. The expression of external potential in many-body basis would be:

$$V(\phi) = -\frac{A}{2}(\cos 6\phi - 1) \tag{1.17}$$

Then we act the on-site potential operator h_V onto the angular momentum basis $|m\rangle$, where the local degree of freedom is described by a planar rotor in Eq.(1.3). We then use the variations of Euler's formula introduced above:

$$\cos(6\phi) = \frac{1}{2}(e^{i6\phi} + e^{-i6\phi}) \tag{1.18}$$

so the matrix elements are $\langle m'|\cos(6\phi)|m\rangle = \frac{1}{2}(\delta_{m',m+6} + \delta_{m',m-6})$. So in this basis, the six-fold potential is not diagonal; it couples angular momentum states differing by $\Delta m = \pm 6$. The dipole interaction is an inter-site coupling term, while the six-fold on-site potential is local. So its matrix elements should be diagonal in angle basis, and off-diagonal with $\Delta m = \pm 6$ in angular momentum basis.

$$\begin{aligned}
&\sum_{m,m'} |m\rangle \langle m| \cos 6\phi \, |m'\rangle \langle m'| \\
&= \sum_{m,m'} |m\rangle \frac{1}{2}(\delta_{m,m'+6} + \delta_{m,m'-6}) \langle m'| \\
&= \sum_{m} \big(|m\rangle \langle m-6| + |m\rangle \langle m+6| \big)
\end{aligned}$$

Note that in the last line the term $|m\rangle\langle m-6|$, which comes from $\delta_{m,m'+6}$, acts as a raising operator: it raises m by 6. The term $|m\rangle\langle m+6|$, which comes from $\delta_{m,m'-6}$, acts as a lowering operator: it lowers m by 6. To see this, recall the definition of the Kronecker delta:

$$\delta_{m,m'+6} = \begin{cases} 1, m = m' + 6 \\ 0, m \neq m' + 6 \end{cases} \tag{1.19}$$

and

$$\delta_{m,m'-6} = \begin{cases} 1, m = m' - 6 \\ 0, m \neq m' - 6 \end{cases} \tag{1.20}$$

1.2 Exact Diagonalization

ED is a powerful numerical technique used to obtain the exact eigenstates and energies of a quantum system. In this approach, the Hamiltonian is expressed in matrix form and diagonalized computationally, from which the exact ground energies and corresponding eigenstates are directly obtained, allowing for the subsequent evaluation of various physical properties.[46,47] Since stationary states are energy eigenstates, the lowest-energy eigenstate is by definition the ground state. For a given Schrödinger equation

$$\hat{H}|\Psi_n\rangle = E_n|\Psi_n\rangle \tag{1.21}$$

Where $\hat{H}$ is the Hamiltonian matrix, E_n are the eigenvalues with ascending order energy $E_0 \leq E_1 \leq E_2 \cdots \leq E_n$. Each energy E_n has a corresponding eigenstate $|\psi_n\rangle$. Before the calculation, a proper basis needs to be carefully selected. The basis needs to be a complete basis for the Hilbert space. Then, we build a Hamiltonian matrix to compute all matrix elements with a Hilbert space dimension of d:

$$H_{ij} = \langle i|\hat{H}|j\rangle \tag{1.22}$$

Next, for a small matrix of up to 12 water molecules, a full diagonalization is enough to get the ground state and its corresponding eigenvector. However, because the dimension of the Hilbert space grows exponentially with the size of the quantum system, full diagonalization

is strictly limited to systems with few degrees of freedom. An iteratively sparse matrix diagonalization is usually utilized to take the place of full diagonalization, for instance, Lanczos[48,49] or Arnoldi.[50] For example, if $\hat{O}$ is an observable, its thermal expectation value is expressed with eigenstates $|n\rangle$ and energy E_n of a given Hamiltonian:

$$\langle O\rangle = \frac{1}{Z}\sum_n e^{-\beta E_n}\,\langle n|O|n\rangle \tag{1.23}$$

where $Z = \sum_n e^{-\beta E_n}$ is the canonical partition function. If the observable can be written down in the initial basis for the problem, then this sum can be evaluated after transforming to the basis of eigenstates. The results of many small clusters ED can be combined to obtain more accurate information about systems in the thermodynamic limit using a numerical linked-cluster expansion. Basis set methods based on ED can yield exact results and reduce the requirements for the symmetry of the system being simulated. But for a many-body system, the increases in system scale render the exponential computational complexity prohibitive for extensive applications. Once diagonalization returns the eigenvalues E_n and eigenvectors $|\psi_n\rangle$, the lowest-energy eigenvector is selected as the ground state (taking care with degeneracies).

1.3 Density Matrix Renormalization Group

DMRG is another numerical variational technique that allows the physical system to converge to its ground state physical quantities when its size is slowly increased, while discarding irrelevant information to keep the Hilbert space size manageable. It is also a very powerful and successful numerical algorithm in modern condensed matter physics and quantum chemistry.[51,52] Proposed in 1992 by Steven R. White, it was initially developed to address the failure of traditional renormalization groups when dealing with strongly-correlated one-dimensional quantum lattice models(such as the Heisenberg and Hubbard models). In quantum mechanics, the combined state space is the tensor product of the individual spaces:

$$\mathcal{H}_{total} = \mathcal{H}_1 \otimes \mathcal{H}_2 \tag{1.24}$$

The main concern of quantum many body physics is the fact that the Hilbert space grows exponentially with system size. In other words, suppose a one-dimensional chain of N particles with local dimension d, whose dimension of Hilbert space is d^N. Consider a quantum system partitioned into two subsystems: a system block A and an environment block B. The total pure state of the combined system $|\Psi\rangle$ can be decomposed using the Schmidt decomposition:

$$|\Psi\rangle = \sum_{i=1}^{\chi} \lambda_i |\phi_i^A\rangle \otimes |\phi_i^B\rangle \tag{1.25}$$

where $|\phi_i^A\rangle$ and $|\phi_i^B\rangle$ form the orthonormal bases for blocks A and B, respectively, and $\lambda_i \geq 0$ are the Schmidt coefficients satisfying the normalization factor $\sum_i \lambda_i^2 = 1$. The reduced density matrix for the system block A is obtained by tracing out the subsystem B:

$$\rho_A = \mathrm{Tr}_B(|\Psi\rangle\langle\Psi|) = \sum_{i=1}^{\chi} \lambda_i^2 |\phi_i^A\rangle\langle\phi_i^A| \tag{1.26}$$

The eigenvalues $w_i = \lambda_i^2$ represent the probability weights of the corresponding eigenstates. In the truncation step, DMRG retains only the M eigenstates with the largest eigenvalues. Taking the "system block + environment block" approach as an example of intuitive basic steps of DMRG: Start with the left and right "blocks" respectively (usually iterating from smaller systems). Then, add a small number of degrees of freedom (grow) in the middle and obtain the target state for the synthesized system (usually using variational/diagonalization). Construct the reduced density matrix (ρ_{block}) of the system block. Next, calculate the eigenvalues of (ρ), sort them by size, and retain the largest eigenspace (equivalent to retaining the main entanglement contribution). After that, update the block with the retained truncated representation, and continue iterating until convergence.

1.3.1 Singular Value Decomposition(SVD)

One essential element is Singular Value Decomposition (SVD). We review here the essential aspects of that method. In linear algebra, singular value decomposition is a mathematical technique used to factorize a non-square matrix into three distinct matrices, uncovering valuable properties into the properties of the original matrix. It is widely used in various

fields such as data science, signal processing, and statistics. While the spectral theorem guarantees that any symmetric (or Hermitian) matrix can be diagonalized by an orthogonal (or unitary) matrix, SVD extends this geometric intuition to any arbitrary matrix $A \in \mathbb{C}^{m\times n}$. The SVD allows any rectangular matrix A to be factorized into three matrices $A = U\Sigma V^\dagger$, where U and $V^\dagger$ are semi-unitary matrices and Σ is a diagonal matrix containing the non-negative singular values σ_i, whose squares σ_i^2 are the eigenvalues of $A^\dagger A$. The columns of V and U form orthonormal bases for the input and output spaces, respectively, and Σ scales each input direction by its singular value. So for a reshaped bipartite wavefunction $\sigma_i^2 = w_i$ are the Schmidt weights (eigenvalues of ρ_A).[53]

Proof: The vectors $\{v_1,v_2,\cdots, v_n\}$ are the eigenvectors of $A^\dagger A$ and form the columns of the unitary matrix V. Then we examine the norm of the transformed vector Av_i to construct the left singular vectors:

$$||Av_i||^2 = \sigma_i^2 \tag{1.27}$$

This implies that:

1. for $1 \leq i \leq r$, where $\sigma_i > 0$, the length of Av_i is σ_i.
2. for $r+1 \leq i \leq n$, where $\sigma_i = 0$, we have $Av_i = 0$.

For the non-zero singular values ($1 \leq i \leq r$), we can define a set of normalized vectors $u_i \in \mathbb{C}^m$ in the co-domain:

$$u_i = \frac{1}{\sigma_i}Av_i \Rightarrow Av_i = \sigma_i u_i \tag{1.28}$$

we must verify that these newly defined vectors $u_1,u_2,\cdots,u_r$ are orthonormal. For any $1 \leq i,j \leq r$ we have :

$$u_i^\dagger u_j = \big(\frac{1}{\sigma_i}Av_i\big)^\dagger\big(\frac{1}{\sigma_j}Av_j\big) = \frac{1}{\sigma_i\sigma_j}v_i^\dagger A^\dagger A v_j = \frac{\sigma_j^2}{\sigma_i\sigma_j}v_i^\dagger v_j = \frac{\sigma_j}{\sigma_i}\delta_{ij} = \delta_{ij} \tag{1.29}$$

where δ_{ij} is the Kronecker delta. Thus, they form an orthonormal set. We can extend this set to form a complete orthonormal basis for $\mathbb{C}^m$, denoting the full set as $u_1,u_2,\cdots,u_m$, which forms the columns of the unitary matrix $U \in \mathbb{C}^{m\times m}$. Following that we can express

the relation $Av_i = \sigma_i u_i$ for all $i = 1, 2, \cdots, n$ simultaneously using matrix notation. Let V be the matrix containing v_i as columns, and U be the matrix containing u_i as columns. Then:

$$AV = A \begin{pmatrix} | & | & & | \\ v_1 & v_2 & \dots & v_n \\ | & | & & | \end{pmatrix} = \begin{pmatrix} | & | & & | \\ \sigma_1 u_1 & \sigma_2 u_2 & \dots & 0 \\ | & | & & | \end{pmatrix} \tag{1.30}$$

This right-hand side of Eq.(1.3.1) can be factored into the matrix U multiplied by an $m \times n$ pseudo-diagonal matrix Σ , where $\Sigma \in \mathbb{R}^{m \times n}$ has the singular values σ_i on its main diagonal and zeros elsewhere:

$$\Sigma = \begin{pmatrix} \sigma_1 & 0 & \dots & 0 & \dots & 0 \\ 0 & \sigma_2 & \dots & 0 & \dots & 0 \\ \vdots & \vdots & \ddots & \vdots & & \vdots \\ 0 & 0 & \dots & \sigma_r & \dots & 0 \\ \vdots & \vdots & & \vdots & \ddots & \vdots \\ 0 & 0 & \dots & 0 & \dots & 0 \end{pmatrix} \tag{1.31}$$

Since V is a unitary matrix($VV^\dagger = I$), we can multiply both sides of $AV = U\Sigma$ by $V^\dagger$ from the right, yielding the final SVD expression:

$$A = U\Sigma V^\dagger \tag{1.32}$$

This completes the formal proof and derivation of the SVD.[54] Its primary function is not to obtain the eigenvalues of the original matrix, but to perfectly decompose any complex linear transformation(non-diagonal, or even non-square matrices) into three standard steps:"rotation-diagonal stretching-rotation." It provides a metric for measuring the extent to which a system extends along the principal axis, as well as a tool for calculating the Schmidt coefficient.

In DMRG, when we flatten the wavefunction into a matrix A, this A is usually not a square matrix at all. The singular values σ_i obtained by performing SVD on A represent

the square roots of the eigenvalues of the reduced density matrix $\rho_A = AA^\dagger$ of subsystem A (i.e., $\sigma_i^2 = w_i$, where ω_i is the probability of occupying a state). If we were to directly compute the eigenvalues of A, it would not even match; only by obtaining the square roots of the eigenvalues via SVD can we calculate the entanglement entropy and perform physical truncation.

1.3.2 Matrix Product States (MPS) Formulation

In modern quantum information language, the success of DMRG is deeply understood through the framework of Matrix Product State (MPS) and Tensor Networks. The relationship between MPS and DMRG is as follows: DMRG controls the bond dimension of MPS while sweeping through the MPS. This also explains why DMRG is particularly suitable for one dimension–MPS is very efficient for one-dimensional low-energy states. A many-body wave function for a chain of N sites can be exactly expressed as:

$$|\Psi\rangle = \sum_{\sigma_1,\ldots,\sigma_N} M_1^{\sigma_1} M_2^{\sigma_2} \ldots M_N^{\sigma_N} |\sigma_1, \ldots, \sigma_N\rangle \tag{1.33}$$

where σ_i denotes the local physical state at site i, and $M_i^{\sigma_i}$ are matrices of dimension $D \times D$. The parameter D is known as the bond dimension, which controls the maximum amount of entanglement that can be captured by the ansatz.

According to the area law for the entanglement entropy in one-dimensional (1D) gapped systems, the entanglement entropy S between two halves of the chain remains bounded as the system size increases. Since the required bond dimension scales as $D \sim e^S$, a finite and manageable bond dimension D is sufficient to approximate the ground state with extraordinary precision. This makes the MPS representation exceptionally efficient for 1D systems.

1.3.3 The Sweep Algorithm and Application Scenarios

The standard finite-system DMRG algorithm operates via an iterative sweeping procedure of SVD over MPS:

- **Initialization:** Construct a small chain and grow it using the infinite-system DMRG algorithm until the target size N is reached.
- **Left-to-Right Sweep:** Optimize the matrices site by site from the left boundary to the right boundary. At each step, a local effective Hamiltonian is formed, and the local tensors are updated using standard Lanczos or Davidson solvers.
- **Right-to-Left Sweep:** Reverse the direction and sweep back from right to left, repeating the optimization to ensure global convergence of the ground-state energy.

This phase optimizes the energy of ground state on a lattice of fixed total length lattice L by iteratively performing left-to-right and right-to-left sweeps.

While DMRG yields nearly exact results for 1D chains and quasi-1D ladders (such as the Hubbard model, Heisenberg model, and quantum spin chains), its application to two-dimensional (2D) systems is constrained by the area law. In 2D, the entanglement entropy scales with the boundary width ($S \sim L$), causing the required bond dimension to scale exponentially as $D \sim e^L$. Despite this challenge, modern 2D DMRG remains highly competitive for cylindrical geometries up to moderate widths, providing crucial benchmarks for exploring frustrated magnets, topological orders, and high-temperature superconductivity phase diagrams.

1.4 Path Integral Monte Carlo

Many enlightening simulation schemes have been developed for rotor-based Monte Carlo simulations. In 1975, Anderson introduced the Diffusion Monte Carlo (DMC) method to determine the ground-state energy of the H_3^+ molecular ion via a random walk algorithm.[55] Verified by the variational method, this simulation successfully controlled the energy error to within 0.013 Hartree with a computation time of approximately 30 minutes. Anderson also noted that computational requirements could be further reduced through more efficient step selection procedures and intelligent code design. While standard DMC maps random walks to the three-dimensional motions of all atoms, Gregory et al.[56] introduced Rigid

Algorithm 1 Sweeping Optimization Procedure for 1D Lattice

Require: Initial tensors of MPS, physical operator O

Ensure: Optimized matrix tensors M^{σ}

$N \leftarrow$ Length of Chain ▷ Initialize the lattice size
Initialize left and right environment caches
for $i = 1$ **to** $N - 1$ **do** ▷ Rightward sweeping loop
    Extract the local tensor for the i-th site
    Solve the local effective Hamiltonian for the lowest eigenvalue problem
    Update the tensor M^{σ_i}
    Perform SVD on M^{σ_i}
    Gauge-shift the residual weights to the $(i+1)$-th site
end for
$t \leftarrow 0$
while $t <$ Max_Iterations **do**
    Perform backward (leftward) sweeping optimization
    if energy change $<$ tolerance criterion **then**
        break ▷ Convergence reached, exit loop
    end if
    $t \leftarrow t + 1$
end while
return M^{σ}

Body Diffusion Monte Carlo (rigid-body Diffusion Monte Carlo (RB-DMC)) in 1995 to simulate water dimers and trimers, incorporating the sampling of energy splits between different symmetry states.

However, since the wave function of the system beyond the ground state has nodes, this will make it difficult for DMC to simulate non-ground state systems. Scientists have considered PIMC simulation a potent tool in studying many-body quantum systems at finite temperatures rather than only the ground state.[57–78] One can also further extend the approach to solve for excited states and compute quantum entanglement properties.[31,79–83] Furthermore, we plan to change the sampling of continuous angular variables to a discrete simulation on grids. This will allow the use of histograms to store the density matrix in order to reduce the computational complexity and further improve the efficiency of simulation calculations. A promising area of investigation is to use discretized angular coordinates on grids for rotational Quantum Monte Carlo (QMC) sampling. This idea will be explored in the later chapters. To systematically investigate how molecular rotation affects the phase states of trapped dipole molecules in various environments (such as magneto-optical traps, optical lattices, and low-temperature solid-state or plastic crystalline phases), we hereby extend the PIMC method to simultaneously account for rotational degrees of freedom, although the PIMC method has traditionally been limited to continuous systems involving only translational motion. The essential elements of PIGS are presented here; the approach is described in detail in Chapter 2.

We assume that the Hamiltonian takes the form $\hat{H} = \hat{T} + V(R)$, where T is the total kinetic energy operator for N particles, and V is the potential energy between the N particles, which depends on the coordinates R of all the degrees of freedom of the particles in the system. In thermal equilibrium, the probability of a given state i being occupied is $e^{-\beta E_i}$. Here, the $\beta = \frac{1}{k_B T}$ is the inverse temperature with Boltzmann constant k_B. The eigenvalues and eigenfunctions of this Hamiltonian are E_i and ψ_i. Therefore, the approximations of expectation values can be expressed in terms of the operator $\hat{O}$ and the trial state,

$$\langle \hat{O} \rangle = \frac{\langle \Psi_T | e^{-\beta \hat{H}/2} \hat{O} e^{-\beta \hat{H}/2} | \Psi_T \rangle}{\langle \Psi_T | e^{-\beta \hat{H}} | \Psi_T \rangle} \tag{1.34}$$

The density matrix in angular space is given by:

$$\rho(\phi, \phi'; \beta) = \langle \phi | e^{-\beta \hat{H}} | \phi' \rangle = \sum_i \Psi_i(\phi) \Psi_i^*(\phi') e^{-\beta E_i} \tag{1.35}$$

In general, the above density matrix $\rho(\phi, \phi'; \beta)$ is a function of the rotation angles ϕ and ϕ'. But in the angular basis representation, the partition function depends on the configuration $\Omega = (\phi_1, \phi_2, \phi_3, \cdots, \phi_N)$:

$$Z = \int d\phi \rho(\phi, \phi; \beta) \tag{1.36}$$

and the expectation value of $\hat{O}$ is

$$\langle \hat{O} \rangle = \frac{\int d\phi d\phi' \rho(\phi, \phi'; \beta) \langle \phi | \hat{O} | \phi' \rangle}{Z} \tag{1.37}$$

The ground state wavefunction is then obtained through the relationship (ignoring normalization)

$$\Psi_0(\phi) = \int d\phi' G(\phi, \phi'; \beta/2) \Psi_T(\phi'), \tag{1.38}$$

where the propagator, also known as the integration kernel, is:

$$G(\phi, \phi'; \beta/2) = \langle \phi | e^{-\beta \hat{H}/2} | \phi' \rangle \tag{1.39}$$

The free rotor imaginary time propagator for a single planar rotor for an imaginary time interval τ, which forms a part of the short time propagator, is well known and is given by:

$$G_0^{(1)}(\phi, \phi'; \tau) = \langle \phi | e^{-\tau \hat{H}} | \phi' \rangle = \frac{1}{2\pi} \sum_{m=-\infty}^{\infty} e^{im(\phi - \phi')} e^{-\tau B m^2}, \tag{1.40}$$

where ϕ and ϕ' are orientations of the rotor and $B = \hbar^2/(2I)$ is the rotational constant.

Writing the density operator as a product of P factors yields the path integral formula for the many-body density matrix. This is the Trotter factorization, where the Trotter number P is a positive integer.

$$e^{-\beta \hat{H}} = (e^{-\tau \hat{H}})^P \tag{1.41}$$

in above equation, each imaginary time step is $\tau = \frac{\beta}{P}$. Then, the density matrix with a convolutional property in the position representation can be expressed as a path integral:

$$\rho(\phi_0, \phi'_P; \beta) = \int \cdots \int d\phi_1 d\phi_2 \cdots d\phi_{P-1} \rho(\phi_0, \phi_1; \tau)\rho(\phi_1, \phi_2; \tau) \cdots \rho(\phi_{P-1}, \phi_P; \tau) \quad (1.42)$$

In the limit $P \to \infty$, this factorization becomes exact. However, for a Hamiltonian that contains both kinetic and potential terms, the factors cannot easily be obtained by multiplication because $\hat{T}$ and $\hat{V}$ do not commute $[\hat{T}, \hat{V}] \neq 0$ i.e.

$$e^{-\tau(\hat{T}+\hat{V})} \neq e^{-\tau\hat{T}} e^{-\tau\hat{V}} \quad (1.43)$$

The Trotter formula holds if $\hat{T}$, $\hat{V}$ and $\hat{T} + \hat{V}$, are self-adjoint and bounded from below. The following formula is an example of symmetrized Trotter formula:

$$e^{-\beta(\hat{T}+\hat{V})} = \prod_{i=1}^{P} [e^{-\tau\hat{V}/2} e^{-\tau\hat{T}} e^{-\tau\hat{V}/2}] + O(P\tau^3) \quad (1.44)$$

where the potential between nearest neighbors is given in Eq.(1.7). Invoking the rigid-rotor approximation, after freezing vibration and separating translation, the motion restricted to a plane leaves a one-angle rotational problem governed entirely by ϕ. And the density matrix ρ in terms of potential is given by the one step propagation as following:

$$\rho_{\beta+\tau} = \rho_\beta \rho_\tau \quad (1.45)$$

Now in a bead picture we can specify the P as the number of time-slices. Then, inserting $P-1$ resolutions of identity in position basis yields for the density operator matrix elements,

$$\rho(\phi^1, \phi^{P+1}; \beta) = \int d\phi \prod_{i=1}^{P} \rho(\phi_i, \phi_{i+1}; \tau) \quad (1.46)$$

We can utilize the Trotter formula Eq.(1.44) and density matrix Eq.(1.42) to obtain the finite temperature partition function.

$$Z = \lim_{P\to\infty} \int d\phi \prod_{i=1}^{P} \rho_V^i(\tau/2) \rho_T^{i,i+1}(\tau) \rho_V^{i+1}(\tau/2) \quad (1.47)$$

For a propagator of a chain of free rotors, a more detailed decomposition is given as:

$$\rho_T(\phi^i, \phi^{i+1}; \tau) = \prod_{j=1}^{N} \langle \phi_j^i | e^{-\tau T_j} | \phi_j^{i+1} \rangle \tag{1.48}$$

We can similarly factor the potential energy operator since for adjacent rotors, the potential is counted pairwise:

$$\rho_V^{\phi_i}(\tau/2) = \prod_{j=1}^{N-1} e^{-\tau V(\phi_j^i, \phi_{j+1}^i)/2} \tag{1.49}$$

Now, with the path integral Monte Carlo, the partition function of this Hamiltonian can be factorized into a product of density matrices with two indices. Note that superscripts represent bead numbers and subscripts are used for representing particle numbers.

$$Z = \lim_{P\to\infty} \int d\phi \prod_{i=1}^{P} \prod_{j=1}^{N-1} \rho_V(\phi_j^i, \phi_{j+1}^i; \tau/2) \rho_T(\phi_j^i, \phi_j^{i+1}; \tau) \rho_V(\phi_j^{i+1}, \phi_{j+1}^{i+1}; \tau/2) \tag{1.50}$$

1.4.1 Path Integral Ground States

Rotational PIMC can be adapted to ground state situations with some modifications of the path topology to yield the PIGS method.[84–95] The accuracy of PIGS simulations has been verified by the ED method for water molecule simulations.

Assume that $\Psi_T(R)$ is the initial trial function and $\Psi_0(R)$ is the ground state wavefunction, with ground state energy E_0 and excited-state energies E_j. For example, the energy estimator under imaginary time $\tau = it/\hbar$:

$$E_\tau = \frac{\langle \Psi_\tau | \hat{H} | \Psi_\tau \rangle}{\langle \Psi_\tau | \Psi_\tau \rangle} \tag{1.51}$$

A PIGS can also be derived from the PIMC algorithm by expanding a trial wavefunction $\Psi_T(R)$

$$\Psi_T(R) = \sum_{j=0}^{\infty} c_j \phi_j(R) \tag{1.52}$$

Provided the overlap c_0 is non-zero, the propagated wavefunction at imaginary time τ is:

$$\Psi_\tau(\phi) = e^{-\tau\hat{H}}\Psi_T(\phi) \tag{1.53}$$

$$= e^{-\tau E_0}\left[c_0\Psi_0(\phi) + \sum_{j=1}^{\infty} c_j e^{-\tau(E_j - E_0)}\Psi_j(\phi)\right] \tag{1.54}$$

From this expansion it is obvious that the efficiency of the PIGS algorithm convergence depends on the overlap. The sum of the squared moduli of the c_j is 1 because the wavefunctions are normalized. $c_0 = \langle\Psi_0|\Psi_T\rangle$ controls the overlap between the ground state Ψ_0 and the trial state Ψ_T. The gaps $e^{-\tau(E_j - E_0)}$ suppress the excited states in the second term in the square bracket. The excited-state terms for $j \geq 1$ decay, which yields better ground state convergence. The excited states contained in $\Psi_T(\phi)$ decay out during the imaginary time propagation.

In the $\tau \to \infty$ limit, $\Psi_T(\phi)$ gradually decays as it propagates through imaginary time. For finite τ, E_τ provides an upper bound to the exact eigenenergy. This implies that a reliable estimate of E_0 can be obtained by extrapolating E_τ to $\tau \to \infty$.

1.4.2 Discrete Variable Representation

In the case of DVR, a continuous coordinate can be replaced by a periodic angular grid, making the potential operator diagonal, while the kinetic operator becomes a matrix that couples grid points. The conversion from the continuous basis to a discretized basis lies in the choice of grid points.

$$|\phi_\alpha\rangle = |2\pi\alpha/L\rangle \quad \text{with} \quad L = 2m_{max} + 1, \tag{1.55}$$

where α is an integer grid index and the grid spacing is $\Delta\phi = 2\pi/L$. The potential energy operator is therefore simplified as:

$$\hat{V}_{\alpha\alpha'} = \hat{V}(\phi_\alpha)\delta_{\alpha\alpha'} \tag{1.56}$$

In this case, the potential $\hat{V}_{\alpha\alpha'}$ can be stored in a diagonal matrix as:

$$\mathbf{V} = \begin{pmatrix} V_1 & 0 & \dots & 0 & \dots & 0 \\ 0 & V_2 & \dots & 0 & \dots & 0 \\ \vdots & \vdots & \ddots & \vdots & & \vdots \\ 0 & 0 & \dots & V_i & \dots & 0 \\ \vdots & \vdots & & \vdots & \ddots & \vdots \\ 0 & 0 & \dots & 0 & \dots & V_L \end{pmatrix} \tag{1.57}$$

The one-body kinetic energy operator in the DVR representation is expressed as:

$$\hat{T} = B\left[\sum_{\alpha} \frac{m_{max}(m_{max}+1)}{3} |\alpha\rangle \langle\alpha| + \sum_{\alpha\neq\alpha'} (-1)^{\Delta\alpha} \frac{\cos(\pi\Delta\alpha/L)}{2\sin^2(\pi\Delta\alpha/L)} |\alpha\rangle \langle\alpha'|\right] \tag{1.58}$$

Therefore, the matrix format of kinetic energy operator has the form:

$$\mathbf{T}_{DVR} = \begin{pmatrix} c_0 & c_1 & c_2 & \dots & c_{L-1} \\ c_{-1} & c_0 & c_1 & \dots & c_{L-2} \\ c_{-2} & c_{-1} & c_0 & \dots & c_{L-3} \\ \vdots & \vdots & \vdots & \ddots & \vdots \\ c_{-(L-1)} & c_{-(L-2)} & c_{-(L-3)} & \dots & c_0 \end{pmatrix} \tag{1.59}$$

In this notation, α denotes the point indices in ϕ representation, $\Delta\alpha = \alpha - \alpha'$ is the index difference, $\Delta\phi = 2\pi/L$ is the spacing, m_{max} is the Fourier representation cutoff, and $L = 2m_{max} + 1$ is the total number of grid points.

1.5 Outline of this thesis

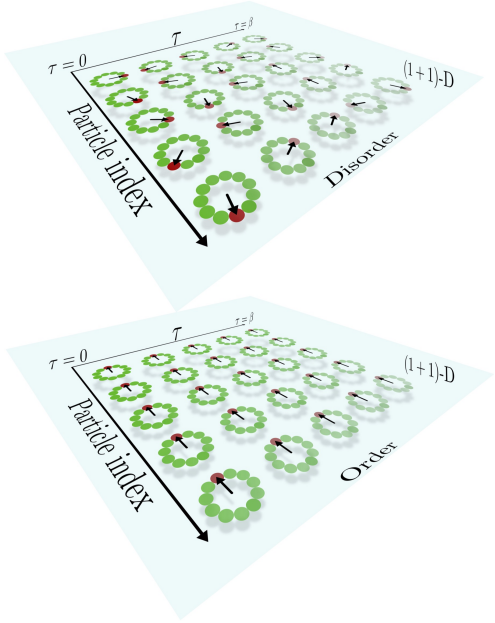
Following the present introduction, Chapter 2 contains the description of a new ground state PIMC approach to simulate chains of planar rotors using the DVR. The theoretical formalism along with algorithmic details and illustrative simulations are presented. In Chapter 3, the generalization to hindered rotors is presented. There, a one-body six-fold potential inspired by recent experimental and theoretical work on water confined to beryl

is added to the co-planar chain Hamiltonian. The DMRG method is used to assess the dependence of the Quantum Phase Transition (QPT) on the barrier height. It is found that the $\mathbb{Z}_2$ symmetry is broken by the transition and a larger barrier leads to earlier QPT to a ferroelectric phase. In Chapter 4, the techniques presented in Chapter 3 are adapted to the case of the stacked rotor chain. Without a hindering potential, the chain has $\mathbb{U}(1)$ symmetry. It is found that the presence of a six-fold potential breaks this $\mathbb{U}(1)$ symmetry leading to a $\ln 6$ value of the entanglement entropy in the ordered phase. The order is antiferroelectric. Conclusions and a perspective for future work are presented in Chapter 5.

Chapter 2

Path integral Monte Carlo in a discrete variable representation with Gibbs sampling: dipolar planar rotor chain

This chapter has been reproduced from Wenxue Zhang, Muhammad Shaeer Moeed, Andrew Bright, Tobias Serwatka, Estevao De Oliveira, Pierre-Nicholas Roy, "Path integral Monte Carlo in a discrete variable representation with Gibbs sampling: Dipolar planar rotor chain", Journal of Chemical Physics **162**, 014106 (2025), with the permission of AIP Publishing.[96]



2.1 Introduction

The simulation of correlated many-body quantum systems is both of great relevance and also a challenging task. Of particular interest is the case of confined dipolar molecules, where intermolecular interactions can lead to rich quantum phases. For example, water molecules trapped in beryl[3,45,97,98] or cordierite[4] crystals exhibit intriguing features such as ferroelectricity, quantum tunneling, and collective excitations. Ferroelectricity has also been observed in water inside carbon nanotubes.[5] Moreover, a quasi-phase transition has been reported for the specific case of water trapped in (6, 5) carbon nanotubes.[12]

Simulations play a key role in our understanding of these systems, and the inclusion of quantum effects is of prime importance. The treatment of rotational degrees of freedom is required in order to model the above systems. It is possible to describe the many-body states of correlated dipolar rotors using exact diagonalization (ED) techniques when a few molecules are present.[17,19] For large systems, the exponential growth of the Hilbert space makes ED calculations impractical. For one-dimensional chain systems, tensor network

techniques have successfully been used to compute the ground state of collections of dipolar linear rotors,[51,52] chains of rotating water molecules[33] with ferroelectric[9] and quantum critical behavior,[35,36] as well as entangled dipolar planar rotor chains.[38,99] Beyond one-dimensional chains, optimizing tensor networks of Matrix Product State (MPS) form[100] using techniques such as the Density Matrix Renormalization Group (DMRG) method[101] becomes prohibitively expensive.

In order to simulate higher dimensional systems such as 2-d molecular lattices or 3-d crystals of confined molecular rotors, alternate approaches are needed. The Path Integral Monte Carlo (PIMC) method[57,102] is a very powerful tool that is amenable to the simulation of general systems in arbitrary dimensions. The generalization of PIMC to molecular rotations is well established[103] and has been used to simulate the ground state of correlated dipolar linear rotors in 1-d[31,32,39,40] and 2-d[41] lattices, and chains of rotating water molecules.[42] Path integral simulations of molecular systems are usually performed in the continuous position representation. As an alternative, Xiao and Poirier have suggested the use of a Discrete Variable Representation (DVR)[104,105] for PIMC simulations.[106,107] Makri and co-workers have also used a DVR for real-time path integral calculations.[108–114] When using a DVR, the path *integral* becomes a path *sum*.

Here, we propose a PIMC approach for the simulation of dipolar rotor systems based on rejection free Gibbs sampling.[115,116] The approach is tested on linear chains of planar rotors of varying sizes and interaction strengths to showcase the suitability of the approach to simulate both ordered and disordered phases, as well as quantum critical regions. The remainder of this paper is organized as follows: in Sec. 2.2, we present methodological details such as the form of the Hamiltonian, the path integral ground state (PIGS) formulation for rotors, the DVR representation, and the Gibbs sampling technique. We present and discuss results in Sec. 2.3, followed by concluding remarks in Sec. 2.4.

2.2 Methodology

2.2.1 Dipolar planar Rotor Chain

We consider a linear chain of N identical planar rotors with nearest neighbors dipole-dipole interactions. For this model, the rotations are constrained to the xy-plane and the linear chain has coplanar orientation along the x-axis as depicted in Fig. 2.1.

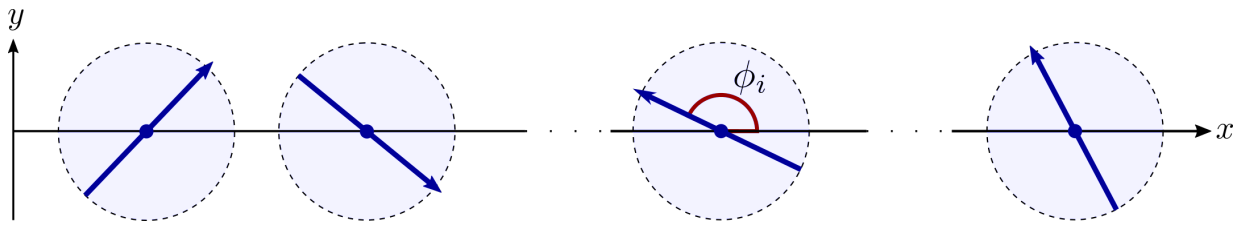


Figure 2.1: Schematic representation of a chain of equally spaced planar rotors.

The Hamiltonian for this system is,

$$\hat{H} = \sum_{i=1}^{N} \hat{L}_{z,i}^2 + g \sum_{i=1}^{N-1} \left[\hat{y}_i \hat{y}_{i+1} - 2\hat{x}_i \hat{x}_{i+1} \right] , \tag{2.1}$$

The first term denotes the rotational kinetic energy, with $\hat{L}_{z,i}^2$ being the angular momentum corresponding to the i-th site. The second term represents the local dipole-dipole interaction of strength g between rotors, and $\hat{x}_i$, $\hat{y}_i$ are the Cartesian components of a unit vector $\hat{e}(\phi_i)$ parametrized by the angle ϕ_i of the i-th dipole. We use units where $\hbar = 1$, and $B = 1$ to keep the expression with reduced units. In the angular position basis, the Hamiltonian becomes,

$$\hat{H} = \hat{T} + g\hat{V} = -\sum_{i=1}^{N} \frac{\partial^2}{\partial \phi_i^2} + g \sum_{i=1}^{N-1} \hat{V}_{i,i+1} \tag{2.2}$$

where the potential between neighboring rotors is given by,

$$\hat{V}_{i,i+1} = \sin(\hat{\phi}_i) \sin(\hat{\phi}_{i+1}) - 2\cos(\hat{\phi}_i) \cos(\hat{\phi}_{i+1}) \, . \tag{2.3}$$

Here, $\hat{\phi}_i$ represents angular position operators acting on the continuous basis set $\{|\phi_i\rangle\}$, for $\phi_i \in \{0, 2\pi\}$. It is important to notice that a further investigation of the system properties involves the explicit calculation of the matrix elements of the Hamiltonian of Eq. (2.2).

2.2.2 Path Integrals For Rotors

Here, we briefly review the PIGS[117] framework to set the stage and fix our path integral notation. To this end, consider the thermal density matrix for our many-body system given by $e^{-\beta\hat{H}}$, where $\beta = 1/k_B T$ is the reciprocal temperature. We can compute the ground state expectation value of an arbitrary operator $\hat{O}$ using a trial wavefunction $|\psi_T\rangle$ and taking the limit as $\beta \to \infty$ as follows

$$\langle \hat{O} \rangle = \lim_{\beta\to\infty} \frac{\langle \psi_T | e^{-\beta\hat{H}/2} \hat{O} e^{-\beta\hat{H}/2} | \psi_T \rangle}{Z_0(\beta)} \tag{2.4}$$

If the trial state has non-zero overlap with the ground state of the system, the estimator defined by Eq. (2.4) converges to the ground state expectation value of $\hat{O}$.

For simplicity, we first construct our path integral using the partition function and then discuss the ground state energy PIGS estimator in a separate section. To this end, consider the trace evaluated in the angular position basis $\{|\phi_i\rangle\}_{1\leq i\leq N}$,

$$Z(\beta) = \int d\boldsymbol{\phi}\ \rho(\boldsymbol{\phi}, \boldsymbol{\phi}, \beta) \tag{2.5}$$

where $(S^1)^N$ is the direct product of N circles (S^1) representing the N-body configuration space, $\boldsymbol{\phi} = (\phi_1, \phi_2, ..., \phi_N)$ is an arbitrary point in the N-body configuration space, and $\rho(\boldsymbol{\phi}, \boldsymbol{\phi}, \beta)$ represents the diagonal elements of the density matrix in the position basis,

$$\rho(\boldsymbol{\phi}, \boldsymbol{\phi}, \beta) = \langle \phi_1, \phi_2, ..., \phi_N | \, e^{-\beta\hat{H}} \, | \phi_1, \phi_2, ..., \phi_N \rangle \tag{2.6}$$

To compute the above matrix elements of the density operator exactly, we would need to exponentiate the Hamiltonian. This is intractable for large systems due to the exponential scaling of the Hilbert space dimension with the number of rotors in the chain. However,

note that we can express the low temperature density operator in terms of high temperature density operators using the convolution property,

$$e^{-\beta\hat{H}} = (e^{-(\beta/P)\hat{H}})^P = (e^{-\tau\hat{H}})^P \tag{2.7}$$

where P is some positive integer (representing the number of time-slices), and $\tau = \beta/P$ is the imaginary time. Then, inserting $P-1$ angular position basis resolutions of identity yields for the density operator matrix elements,

$$\rho(\boldsymbol{\phi}^1, \boldsymbol{\phi}^{P+1}, \beta) = \int d\vec{\boldsymbol{\phi}} \prod_{i=1}^{P} \rho(\boldsymbol{\phi}^i, \boldsymbol{\phi}^{i+1}, \tau) \tag{2.8}$$

where $\vec{\boldsymbol{\phi}} = (\boldsymbol{\phi}^1, ..., \boldsymbol{\phi}^{P+1})$. Note that superscripts in our notation are reserved for bead numbers whereas subscripts will be used to represent particle numbers. We can now approximate the high-temperature density using the symmetrized Trotter formula which gives

$$e^{-\tau\hat{H}} = e^{-\tau\hat{V}/2} e^{-\tau\hat{T}} e^{-\tau\hat{V}/2} + \mathcal{O}(\tau^3) \tag{2.9}$$

Here, $\hat{T}$ is the kinetic energy operator and $\hat{V}$ is the potential energy operator. This particular symmetric splitting allows us to use the fact that the potential is diagonal in the position basis to express the density matrix as follows,

$$\rho(\boldsymbol{\phi}^i, \boldsymbol{\phi}^{i+1}, \tau) \approx \rho_T^{i,i+1}(\tau)\ \rho_V^i(\tau/2)\ \rho_V^{i+1}(\tau/2) \tag{2.10}$$

where

$$\rho_V^i(\tau/2) = \rho_V(\boldsymbol{\phi}^i, \tau/2) = e^{-\tau V(\boldsymbol{\phi}^i)/2} \tag{2.11}$$

$$\rho_T^{i,i+1}(\tau) = \rho_T(\boldsymbol{\phi}^i, \boldsymbol{\phi}^{i+1}, \tau) = \left\langle \boldsymbol{\phi}^i \right| e^{-\tau\hat{T}} \left| \boldsymbol{\phi}^{i+1} \right\rangle \tag{2.12}$$

Using Eqs. (2.5), (2.8) and (2.10), we finally get for the finite temperature partition function,

$$Z = \lim_{P\to\infty} \int d\vec{\boldsymbol{\phi}} \prod_{i=1}^{P} \rho_V^i(\tau/2)\ \rho_V^{i+1}(\tau/2)\ \rho_T^{i,i+1}(\tau) \tag{2.13}$$

where $\vec{\boldsymbol{\phi}} = (\boldsymbol{\phi}^1, ..., \boldsymbol{\phi}^P, \boldsymbol{\phi}^{P+1})$. Here, we need to impose the constraint that the first and last bead be the same ($\boldsymbol{\phi}^1 = \boldsymbol{\phi}^{P+1}$) since we are evaluating the trace. Moreover, we need

to take the limit as $P \to \infty \iff \tau \to 0$ since the Trotter factorization in equation (2.9) is only exact in this limit. Note that Z is still a function of β although we have omitted this dependence in Eq. (2.13) for notational brevity.

We can further factor the kinetic energy (free) propagator since the kinetic energy operator is a sum of commuting operators $\hat{T}_j = \hat{L}_{z,j}$ where j is the index corresponding to the jth rotor in the chain. This yields,

$$\rho_T^{i,i+1}(\tau) = \prod_{j=1}^{N} \langle \phi_j^i | e^{-\tau \hat{T}_j} | \phi_j^{i+1} \rangle \tag{2.14}$$

Noting that the total potential is a sum over pair-wise terms, we can similarly factor the potential energy propagator,

$$\rho_V^i(\tau/2) = \prod_{j=1}^{N-1} e^{-\tau V(\phi_j^i, \phi_{j+1}^i)/2} \tag{2.15}$$

where V in the exponent here denotes the 2-body potential as defined by Eq. (2.3). This gives for Eq. (2.13),

$$Z = \lim_{P\to\infty} \int d\vec{\boldsymbol{\phi}} \prod_{i=1}^{P} \prod_{j=1}^{N-1} \rho_T(\phi_j^i, \phi_j^{i+1}, \tau) \times \rho_V(\phi_j^i, \phi_{j+1}^i, \tau/2)\ \rho_V(\phi_j^{i+1}, \phi_{j+1}^{i+1}, \tau/2) \tag{2.16}$$

This final set of expressions shows that our path integral density is the product of two-variable functions. Consequently, our planar rotor chain system is especially amenable to Markov Chain Monte Carlo (MCMC) methods since the two-variable densities can be easily pre-computed on a grid and stored prior to the simulation. Moreover, as we will show below, the density enters our MCMC algorithms as a quotient. Consequently, for sequential algorithms such as Gibbs sampling that rely on single variable moves, only those terms in the full product that depend on the variable being perturbed need to be computed for each move. This greatly reduces the density calculation overhead for each step.

2.2.3 PIGS Estimators

Having developed our path integral formalism, we can now derive the PIGS ground state energy estimator used for our analysis. To this end, consider again Eq. (2.4) with $\hat{O} = \hat{H}$. Since the density operator commutes with the Hamiltonian, we get,

$$E_0 = \langle \hat{H} \rangle = \lim_{\beta \to \infty} \frac{\langle \psi_T | e^{-\beta \hat{H}} \hat{H} | \psi_T \rangle}{Z_0(\beta)} \tag{2.17}$$

Inserting angular position basis resolutions of identity as before, we get for the energy estimator,

$$E_0 = \frac{1}{Z_0} \int d\vec{\boldsymbol{\phi}} \; \psi_T^*(\boldsymbol{\phi}^1) \rho(\boldsymbol{\phi}^1, \boldsymbol{\phi}^2, \beta) \hat{H} \psi_T(\boldsymbol{\phi}^2) \tag{2.18}$$

Here, $\vec{\boldsymbol{\phi}} = (\boldsymbol{\phi}^1, \boldsymbol{\phi}^2)$. For our simulations, we can pick $\psi_T(\boldsymbol{\phi}) = 1/\sqrt{2\pi}$ to be our trial wavefunction. Then, since the kinetic energy operator is a differential operator, we get,

$$E_0 = \frac{1}{2\pi Z_0} \int d\vec{\boldsymbol{\phi}} \; \rho(\boldsymbol{\phi}^1, \boldsymbol{\phi}^2, \beta) V(\boldsymbol{\phi}^2) \tag{2.19}$$

Because the energy estimator depends on the density operator matrix elements in the position basis, we can again use the convolution property and the Trotter expansion to get,

$$E_0(\beta, P) = \frac{1}{2\pi Z_0(\beta)} \int d\vec{\boldsymbol{\phi}} \prod_{i=1}^{P} \prod_{j=1}^{N-1} \rho_T(\phi_j^i, \phi_j^{i+1}, \tau) \times \rho_V(\phi_j^i, \phi_{j+1}^i, \tau/2) \; \rho_V(\phi_j^{i+1}, \phi_{j+1}^{i+1}, \tau/2) \; V(\boldsymbol{\phi}^{P+1}) \tag{2.20}$$

where $\vec{\boldsymbol{\phi}} = (\boldsymbol{\phi}^1, ..., \boldsymbol{\phi}^P, \boldsymbol{\phi}^{P+1})$ as before. The error in this estimator is $\mathcal{O}(\tau^2)$ arising, as with the partition function, from the Trotter expansion. In the limit of $P \to \infty \iff \tau = \beta/P \to 0$, the estimator converges to the ground state energy. To evaluate the limit computationally, we therefore construct an increasing sequence of time slices, $\mathcal{P} = \{P_k\}$, and compute the above integral for each of those values of P_k. Then, we fit the sequence of energy estimates $\mathcal{E} = \{E_P\}_{P \in \mathcal{P}}$ using a quadratic model and extrapolate to estimate the ground state energy.

For structural properties (functions of position only), the operator $\hat{O}$ doesn't commute with the propagator. Consequently, we must factorize Eq. (2.4) directly. In this work, we also consider the orientational correlation of the system defined as,

$$\hat{C} = \sum_{i=1}^{N-1} \hat{e}_i \cdot \hat{e}_{i+1} = \sum_{i=1}^{N-1} \cos(\hat{\phi}_i - \hat{\phi}_{i+1}) \tag{2.21}$$

where $e_i = (\cos(\phi_i), \sin(\phi_i))$ is the electric dipole corresponding to the ith rotor in the chain. Setting $\hat{O} = \hat{C}$ in Eq. (2.4) and expanding in the position basis gives,

$$\begin{aligned} \langle \hat{C} \rangle = \frac{1}{Z_0} \int d\vec{\boldsymbol{\phi}}\ \psi_T^*(\boldsymbol{\phi}^1) \rho(\boldsymbol{\phi}^1, \boldsymbol{\phi}^2, \beta/2) \\ \times C(\boldsymbol{\phi}^2, \boldsymbol{\phi}^3) \rho(\boldsymbol{\phi}^3, \boldsymbol{\phi}^4, \beta/2) \psi_T(\boldsymbol{\phi}^4) \end{aligned} \tag{2.22}$$

where $\vec{\boldsymbol{\phi}} = (\boldsymbol{\phi}^1, \boldsymbol{\phi}^2, \boldsymbol{\phi}^3, \boldsymbol{\phi}^4)$. Since the correlation is diagonal in the position basis, we get,

$$C(\boldsymbol{\phi}^2, \boldsymbol{\phi}^3) = \langle \boldsymbol{\phi}^2 | \hat{C} | \boldsymbol{\phi}^3 \rangle = \delta(\boldsymbol{\phi}^2 - \boldsymbol{\phi}^3) C(\boldsymbol{\phi}^2) \tag{2.23}$$

where $C(\boldsymbol{\phi}^2)$ is defined by Eq. (2.21). We can now evaluate the integral over $\boldsymbol{\phi}^2$ using the delta function and re-label the integration variables $(1, 2, 3) \rightarrow (1, P/2+1, P+1)$ for convenience. This yields

$$\begin{aligned} \langle \hat{C} \rangle = \frac{1}{2\pi Z_0} \int d\vec{\boldsymbol{\phi}}\ \rho(\boldsymbol{\phi}^1, \boldsymbol{\phi}^{P/2+1}, \beta/2) \\ \times \rho(\boldsymbol{\phi}^{P/2+1}, \boldsymbol{\phi}^{P+1}, \beta/2) C(\boldsymbol{\phi}^{P/2+1}) \end{aligned} \tag{2.24}$$

where we have used our trial function definition $\psi_T(\boldsymbol{\phi}) = 1/\sqrt{2\pi}$. Finally, Trotter expanding both densities in the above equation $P/2$ times each gives the PIGS estimator for the correlation,

$$\begin{aligned} C(\beta, P) = \frac{1}{2\pi Z_0(\beta)} \int d\vec{\boldsymbol{\phi}} \prod_{i=1}^{P} \prod_{j=1}^{N-1} \rho_T(\phi_j^i, \phi_j^{i+1}, \tau) \\ \times \rho_V(\phi_j^i, \phi_{j+1}^i, \tau/2)\ \rho_V(\phi_j^{i+1}, \phi_{j+1}^{i+1}, \tau/2)\ C(\boldsymbol{\phi}^{P/2+1}) \end{aligned} \tag{2.25}$$

It is instructive to note here that P has to be even since we assumed that $P/2$ is an integer during the time-slicing derivation above. Moreover, the density in the correlation

estimator is exactly the same as that for energy and so the same MCMC simulation can be used to estimate both. However, in the case of correlation (or any structural properties) the corresponding position kernel must be evaluated at the middle bead only. This is a distinct feature of PIGS in contrast to finite temperature PIMC where all the beads are equivalent and structural properties can be evaluated on any of the beads due to the existence of closed paths.

2.2.4 Grid Representation: from Path Integrals to Path Sums

Our proposed approach for computing ground state properties relies on discretizing the continuous angular position basis using the Colbert-Miller DVR.[118] In this framework, the discretized angular position basis takes the form,

$$\{|\phi_\alpha\rangle\} = \{|\phi(\alpha)\rangle\} = \{|2\pi\alpha/L\rangle\} = \{|\alpha\rangle\} \tag{2.26}$$

where $L = 2m + 1$ is the total number of grid points, d is the Fourier representation cutoff and α is an integer such that $0 \leq \alpha \leq 2d$. Note that the index α here represents a point on the ϕ grid as opposed to a particle or bead number. Greek subscripts on ϕ will henceforth be reserved for grid indices. We will continue our convention of using Latin subscripts for particle indices. The 1-body kinetic energy matrix elements in the DVR[118] representation take the form,

$$\langle\alpha|T|\alpha'\rangle = \begin{cases} \frac{d(d+1)}{3} & \alpha = \alpha' \\ (-1)^{\Delta\alpha} \frac{\cos(\pi(\Delta\alpha)/L)}{2\sin^2(\pi(\Delta\alpha)/L)} & \alpha \neq \alpha' \end{cases} \tag{2.27}$$

where $\Delta\alpha = \alpha - \alpha'$. In the DVR basis, we can diagonalize the 1-body kinetic energy operator numerically and compute its exponential. This allows us to pre-compute and store the 1-body kinetic energy propagator as a matrix. The 2-body potential energy operator is evaluated on the grid as follows,

$$\langle\alpha_1, \alpha_2|V|\alpha_1', \alpha_2'\rangle = V(\phi(\alpha_1), \phi(\alpha_2))\delta_{\alpha_1,\alpha_1'}\delta_{\alpha_2,\alpha_2'} \tag{2.28}$$

The DVR basis also enables us to store the diagonal entries of the (2-body) potential energy propagator as a matrix. The grid representation maps the $N(P+1)$-dimensional

integrals in Eqs. (2.16) and (2.20) to summations. Therefore, in this framework, the energy estimator yields,

$$E_0(\beta, P) = \frac{1}{2\pi Z} \sum_{\vec{\boldsymbol{\alpha}}} \prod_{i=1}^{P} \prod_{j=1}^{N-1} \rho_T(\alpha_j^i, \alpha_j^{i+1}, \tau) \times \rho_V(\alpha_j^i, \alpha_{j+1}^i, \tau/2)\ \rho_V(\alpha_j^{i+1}, \alpha_{j+1}^{i+1}, \tau/2)\ V(\boldsymbol{\alpha}^{P+1}) \quad (2.29)$$

where $\vec{\boldsymbol{\alpha}}$ is an $N(P+1)$ dimensional vector. Each entry of $\vec{\boldsymbol{\alpha}}$ represents one variable in the path sum and can take integer values between 0 and $2d$. In this "vectorized" form, the p-th bead and n-th rotor orientation is specified by the component with index $k = (p-1)N + n$. $\boldsymbol{\alpha}^{P+1}$ is the sub-tuple of $\vec{\boldsymbol{\alpha}}$ corresponding to the last bead. Note that we have employed the following abuse of notation in specifying Eq. (2.29),

$$\rho_V(\alpha_j^i, \alpha_{j+1}^i, \tau/2) = \rho_V(\phi(\alpha_j^i), \phi(\alpha_{j+1}^i), \tau/2) \quad (2.30)$$

$$\rho_T(\alpha_j^i, \alpha_j^{i+1}, \tau) = \rho_T(\phi(\alpha_j^i), \phi(\alpha_j^{i+1}), \tau) \quad (2.31)$$

$$V(\boldsymbol{\alpha}^{P+1}) = V(\phi(\alpha_1^{P+1}), ..., \phi(\alpha_N^{P+1})) \quad (2.32)$$

As discussed above, one benefit of the DVR grid is that it enables us to pre-compute all three of these components (ρ_T, ρ_V, V) in the discretized angular position basis (Eq. (2.26)) and index them as required during the simulation. Not only does this discretization optimize the efficiency of the MCMC simulation but also enables us to use sampling approaches adapted to discrete probability distribution such as Gibbs sampling.

2.2.5 Gibbs Sampling The Many Body Distribution

MCMC approaches approximate multi-dimensional integrals (such as equation (2.13)) stochastically,

$$\int_\Omega d\boldsymbol{x}\ f(\boldsymbol{x}) p(\boldsymbol{x}) \approx \frac{1}{M} \sum_{\boldsymbol{x}_i \in S} f(\boldsymbol{x}_i) \quad (2.33)$$

where Ω is the multi-dimensional configuration space, $p(\boldsymbol{x})$ is some probability distribution, and S is a set of M points in Ω statistically sampled according to $p(\boldsymbol{x})$. We can also use

this approach to estimate multi-dimensional sums such as Eq. (2.29). For the rotor chain energy estimator in the DVR basis, the probability distribution is

$$p(\vec{\boldsymbol{\alpha}}) = \frac{1}{2\pi Z}\prod_{i=1}^{P}\prod_{j=1}^{N}\rho_T(\alpha_j^i, \alpha_j^{i+1}, \tau) \times \prod_{j=1}^{N-1}\rho_V(\alpha_j^i, \alpha_{j+1}^i, \tau/2)\ \rho_V(\alpha_j^{i+1}, \alpha_{j+1}^{i+1}, \tau/2) \quad (2.34)$$

Owing to the exponential scaling of the number of variables with the number of particles, this N-body distribution is difficult to sample directly. However, we can leverage the factorized form of the density by instead sampling a Markov chain that converges to the desired distribution.

Conventional approaches in this domain involve using the sequential Metropolis-Hastings (M-H) algorithm in which, at each step, a move is proposed and then either accepted or rejected depending on the likelihood of the proposed configuration compared to the previous configuration. This invariably leads to a set of samples with a high degree of redundancy because a large set of proposed moves are rejected. In this work, we adapt the sequential Gibbs sampling algorithm to the planar rotor problem which, by construction, is rejection free and consequently, more efficient than M-H. The algorithm, in steps, is described below:

1. Specify the initial configuration of all the variables:

$$(\vec{\boldsymbol{\alpha}})^0 = \left(\alpha_1^0, ..., \alpha_{(P+1)N}^0\right) \quad (2.35)$$

2. To Sample $(\vec{\boldsymbol{\alpha}})^{k+1}$, given a configuration for the current step $(\vec{\boldsymbol{\alpha}})^k$, loop over all the $(P+1)N$ components, sampling each sequentially. To sample α_j^{k+1}, we use the conditional distribution,

$$p\left(\tilde{\alpha}_j^{k+1} | \alpha_1^{k+1}, .., \alpha_{j-1}^{k+1}, \alpha_{j+1}^k, .., \alpha_{(P+1)N}^k\right) = \frac{1}{Z_G} p\left(\alpha_1^{k+1}, .., \alpha_{j-1}^{k+1}, \tilde{\alpha}_j^{k+1}, \alpha_{j+1}^k, .., \alpha_{(P+1)N}^k\right) \quad (2.36)$$

where $\tilde{\alpha}_j^{k+1}$ are indices $1, ..., N-1$ specifying angular position values on the DVR grid and Z_G is a normalization. The sampled value of $\tilde{\alpha}_j^{k+1}$ is used as a parameter to sample $\tilde{\alpha}_{j+1}^{k+1}$.

3. Repeat step 2 for each pass until the desired statistical accuracy is obtained. Finally, compute the average potential energy over the sampled configurations to estimate the ground state energy.

Note that we have reserved superscripts to denote the sample index and subscripts to denote components of the sample. Therefore, α_j^i denotes the jth component of the ith sample. As shown in Eq. (2.36), the full probability density only enters the algorithm as a quotient. Therefore, the factorized form of the density (Eq. (2.34)) simplifies the single-variable sampling greatly,

$$\begin{aligned} &p\left(\tilde{\alpha}_j^{k+1}|\alpha_1^{k+1},..,\alpha_{j-1}^{k+1},\alpha_{j+1}^{k},..,\alpha_{(P+1)N}^{k}\right) = \\ &p\left(\tilde{\alpha}_{j_{p,n}}^{k+1}|\alpha_{j_{(p+1),n}}^{k},\alpha_{j_{(p-1),n}}^{k+1},\alpha_{j_{p,(n+1)}}^{k},\alpha_{j_{p,(n-1)}}^{k}\right) \end{aligned} \tag{2.37}$$

where the subindex $j_{p,n}$ represents now the "vectorized" index associated with bead p and rotor n given by $j_{p,n} = (p-1)N + n$. Since there is a finite set of values that $\tilde{\alpha}_{j_{p,n}}^{k+1}$ can take, we can sample this conditional via weighted uniform sampling.

It is also instructive to note that in the conditional distribution for the jth variable, samples from step $(k+1)$ are used for the first $j-1$ variables and samples from step k are used for the last $N(P+1)-j$ variables. Therefore, the conditional distribution changes for each variable within each step. This implies that the associated Markov chain is not reversible and the sampler does not satisfy detailed balance (similar to the sequential M-H technique). However, the algorithm does satisfy the balance condition which implies that the associated Markov chain still converges to the desired probability distribution.[119,120]

2.3 Results and Discussion

To assess the utility of the DVR grid as a viable discretization scheme for Gibbs sampling, we first study the imaginary time convergence of the density for small numbers of particles ($N = 2$ and $N = 3$). Then, we extend the approach to larger system sizes ($N = 100$) and study their structural properties. In particular, we find that using the Gibbs-DVR approach results in faster Markov chain convergence due to lower correlations between steps.

Moreover, this methodology is also simpler to optimize than rejection-based techniques such as continuous M-H because it doesn't have a tunable acceptance ratio modulating the efficiency of the simulation.

We studied the convergence of ground state energy for $N = 2$ to determine the minimum required frequency cutoff for ground state properties using the DVR grid. We find that $m = 5$ ($L = 11$ grid points for each rotor) is sufficient. However, as discussed below, for any given value of m, there exists a value of τ such that the density acquires a sign problem due to the presence of positive off-diagonal entries in the Hamiltonian in the position basis. This renders the density unusable for sampling techniques. This issue can be remedied if necessary by increasing the value of m. For our results, $m = 5$ is sufficient since we do not require $\tau < 0.2$ for any of our results to see convergence. The approach described in Ref. 38 is used for the DMRG benchmark calculations. Calculations are performed using the iTensor package.[121]

2.3.1 Imaginary Time Step Convergence

To test convergence with τ, we compute the ground state energy using the DVR grid and the Numerical Matrix Multiplication (NMM) method[122] for $N = 2$ and $N = 3$ and compare with ED results. The purpose of this NMM analysis is to highlight the convergence behavior of the systematic factorization error. As shown in Figs. 2.2 and 2.3, fitting NMM results corresponding to $\tau > 0.17$ results in convergence to ED results. However, below a critical τ value the NMM results diverge. This issue has been raised by Xiao and Poirier.[106,107]

We found that this divergent behavior at small τ values comes from the 1-body kinetic energy only and therefore does not depend on system size N or interaction strength g. The DVR representation of the kinetic energy (see Eq. (2.27)) contains positive entries on the off-diagonals due to the cosine function. This results in the DVR representation of the Hamiltonian having non-negative off-diagonal entries for $m > 1$. Consequently, the Hamiltonian in the DVR basis is non-stoquastic. For small τ, $e^{-\tau H} \approx 1 - \tau H$ which means that the off-diagonal entries of the density matrix are given by: $\langle\phi|e^{-\tau H}|\phi'\rangle \approx -\tau\langle\phi|T|\phi'\rangle$. Therefore, these matrix entries are negative if $\langle\phi|T|\phi'\rangle > 0$. Consequently, we can't interpret the DVR basis representation of the density as a set of transition probabilities and use

them in sampling paradigms such as PIMC when τ is small for this problem. Note that this sign problem doesn't affect NMM. The divergence shown in Figs. 2.2 and 2.3 is due to the fact that we use the absolute values of the propagator matrix entries since PIMC requires a positive-definite density. Finally, it should also be noted that this critical value of τ can be made smaller by increasing m in the DVR representation.

2.3.2 Reciprocal Temperature Convergence

As discussed above, our path integral simulations converge to the ground state operator expectation values in the limit of $\beta \to \infty$. Therefore, we study the convergence of the PIGS estimator as a function of β to determine a finite value β_c such that the associated error for all $\beta \geq \beta_c$ is negligible. To this end, we computed ground state energy estimates $E_0(\tau, \beta)$ using DVR-NMM for $N = 2$ corresponding to a decreasing sequence of τ values: $\{\tau\}_k = \{0.24 - 0.01k\}$ for integers $0 \leq k \leq 7$. Fitting a quadratic model in τ with an additional quartic term ($E(\tau, \beta) = E_0(\beta) + a(\beta)\tau^2 + b(\beta)\tau^4$) for each β, we computed the τ-independent DVR-NMM estimates of the ground state energy associated with logarithmically spaced values of β in the interval $(1.5, 15)$ as shown in Fig. 2.4. We find that at $\beta \approx 4.0$, the error is negligible which is not surprising given the exponential dependence of the propagator on β. Since any value above 4.0 is sufficient, we pick $\beta = 10.0$ for our N-body simulations.

Finally, we also compute the ground state energies as a function of the coupling strength g for $N = 2$ and $N = 3$ by extrapolating in τ as discussed above with $\beta = 10.0$. Comparing this to ED results (see Fig. 2.5), we see that the error is negligible. This suggests that our methodology should be robust to variations in the interaction strength g and the number of rotors in the chain N. We further examine this point in the next section while using our approach to study this system in the large N limit.

2.3.3 Many-Body Extension

To showcase the utility of this approach for studying the ground state properties of large systems, we compute the ground state energy and the orientational correlation function. Since we cannot diagonalize the Hamiltonian for large systems, we compare our results to

DMRG instead. Figure 2.6 below shows the ground state energy for $N = 100$ and Fig 2.7 shows the correlation for $N = 100$. The solid lines show the DMRG results. For both the energy and the correlation, the PIGS estimates converge to the DMRG results within statistical error (estimated using the binning method). For both of these properties, we use $\beta = 10.0$, $P = 49$ and 50000 steps for the PIGS estimates. The simulations for $g < 0.5$ were started with randomly oriented rotors whereas for $g \geq 0.5$, the simulations were started with all the rotors pointing along the chain since we expect all the rotors to be aligned at equilibrium when g is large.

Previous work has shown that there is a phase transition in this system at $g \sim 0.5$ as the ground state moves from the disordered state ($g < 0.5$) to an ordered state ($g > 0.5$).[99] While typically, phase transitions are difficult to study using Monte Carlo simulations due to the critical slow down near the transition, the existence of these two phases in the large N limit for our system can be resolved by our approach as can be seen from Fig. 2.7.

Angular distributions for $N = 100$ are shown in Fig. 2.8. We selected three interaction strength values ($g = 0.1, 0.5, 1.0$). The distributions are uniform when $g = 0.1$, since g is less than the critical value ($g_c = 0.5$). At $g = 0.5$ some localization starts to appear and the chain is polarized at π and 2π when $g = 1.0$.

2.3.4 Correlation analysis

As mentioned above, the Gibbs sampling algorithm yields faster Markov chain decorrelation. Consequently, less Monte Carlo steps are required for a given simulation. To exhibit this, we computed the chain autocorrelation for the M-H algorithm as well as the Gibbs sampling algorithm (see Fig. 2.9) using the orientational correlation as the estimator for $g = 0.1$, $g = 0.5$ and $g = 1.0$. All three simulations used $N = 100$, $P = 48$ and 50000 simulation steps. For $g = 0.1$, the starting configuration is random for each rotor whereas for $g = 0.5$ and $g = 1.0$, the simulation is initiated with all the rotors aligned (pointing along the chain). Then, we computed the decorrelation time $1/\Gamma$ for each simulation:

$$1/\Gamma = \inf\{t \mid \langle \delta C^2 \rangle < 1/e\} \tag{2.38}$$

where t here corresponds to simulation steps, $\langle \delta C^2 \rangle$ is the autocorrelation of the orientational correlation estimator and inf denotes the infimum of the set in question. In all cases, the Gibbs decorrelation time is less than the M-H decorrelation time which implies that the Gibbs sampling algorithm outperforms the M-H algorithm for this system for all phases (ordered as well as disordered).

In the critical region ($g = 0.5$), the decorrelation time for the M-H algorithm is much larger than in the ordered and disordered phases as shown in Fig. 2.9. This is characteristic of critical slowing down near phase transitions. However, it is interesting to note that the Gibbs algorithm autocorrelation decays very fast here as well which allows us to accurately estimate the orientational correlation in the critical region as shown in Fig. 2.7.

2.3.5 Beyond 1d lattices and Nearest Neighbor Interactions

The Gibbs-DVR approach for PIMC is readily applicable to higher dimensional lattices. For such systems, consider the following Hamiltonian,

$$H = \sum_{i=1}^{N} T_i + \sum_{i<j}^{N} V_{ij} \tag{2.39}$$

where T_i is the on-site kinetic energy term and V_{ij} is the interaction between any two lattice sites (not necessarily nearest neighbors). Note here that the summations run over the entire 2 or 3 dimensional lattice which implies that the coupling strength between any two lattice sites depends on the distance between them. The derivation of the partition function in Eq. (2.13) proceeds identically. Then to compute the high temperature density matrix elements, we can again Trotter factorize to obtain,

$$\rho(\boldsymbol{\phi}^i, \boldsymbol{\phi}^{i+1}, \tau) = \langle \boldsymbol{\phi}^i | e^{-\tau T} | \boldsymbol{\phi}^{i+1} \rangle e^{-\tau (V(\phi^i) + V(\phi^{i+1}))/2} \tag{2.40}$$

The free propagator factors into a product of one-body terms,

$$\langle \boldsymbol{\phi}^i | e^{-\tau T} | \boldsymbol{\phi}^{i+1} \rangle = \prod_{j=1}^{N} \rho_T(\phi_j^i, \phi_j^{i+1}, \tau) \tag{2.41}$$

ρ_T is the one-body free propagator which can be computed before the simulation and tabulated as done for the $1d$ chain. For the potential term, we have the following,

$$e^{-\tau V(\phi^i)/2} = \prod_{j<k}^{N} \rho_V(\phi_j^i, \phi_k^i, R_{jk}, \tau/2) \tag{2.42}$$

$$\rho_V(\phi_j^i, \phi_k^i, R_{jk}, \tau/2) = e^{-\tau V_{j,k}(\phi_j^i, \phi_k^i, R_{jk})/2} \tag{2.43}$$

where $V_{j,k}(\phi_j^i, \phi_j^i, R_{jk})$ is the 2-body potential for the pair determined by indices j and k, and R_{jk} is the distance between the associated rotors in the lattice. The final probability distribution that we need to sample in the DVR representation now becomes,

$$p(\vec{\alpha}) = \frac{1}{2\pi Z} \prod_{i=1}^{P} \prod_{j=1}^{N} \rho_T(\alpha_j^i, \alpha_j^{i+1}, \tau)$$

$$\times \prod_{j<k}^{N} \rho_V(\alpha_j^i, \alpha_k^i, R_{jk}, \tau/2)\ \rho_V(\alpha_j^{i+1}, \alpha_k^{i+1}, R_{jk}, \tau/2) \tag{2.44}$$

To Gibbs sample this distribution, we need to compute the conditional probabilities,

$$p\left(\tilde{\alpha}_j^{k+1} | \alpha_1^{k+1}, .., \alpha_{j-1}^{k+1}, \alpha_{j+1}^{k}, .., \alpha_{(P+1)N}^{k}\right), \tag{2.45}$$

$$\tilde{\alpha}_j^{k+1} \in \{0, ..., 2d\} \tag{2.46}$$

The contributions of ρ_T to this can be calculated identically to the 1d case. For ρ_V, since we have relaxed the nearest neighbors restriction, we would need to compute the contributions due to each of the $N(N-1)/2$ pairs of interacting sites in the lattice which requires us to loop over all such pairs. Practically, due to the small value of $2d$ afforded by the DVR basis, this can be done efficiently.

We can also analyze the time-complexity of the higher dimensional lattice algorithm. If the r-dimensional lattice is constructed by copying a single chain of N_1 rotors N_1^{r-1} times, the number of rotors in the higher dimensional lattice would be N_1^r. For a fixed number of MC steps and given number of beads, we know that algorithm for the $1d$ chain with nearest neighbor interactions is polynomial in N_1. So, we can assume that it is $\mathcal{O}(N_1^q)$ for some integer q. Then, if we let the interaction run over all lattice sites of the $1d$ chain, the algorithm would be $\mathcal{O}(N_1^{q+2})$ because of the additional iterative loop. Finally, the effect

of increasing the lattice dimension is to map $N_1 \to N_1^r$ following the construction outlined above. Therefore, the DVR-Gibbs algorithm complexity would become $\mathcal{O}\left(N_1^{rq}\right)$ for the higher-dimensional nearest neigbors case and $\mathcal{O}\left(N_1^{r(q+2)}\right)$ for the all pairs interaction, higher lattice dimension case. This is at most a polynomial slowdown compared to the 1d nearest neighbors case. It is important to note here that this complexity analysis also holds true for the continuous Metropolis-Hastings Monte Carlo approach used typically for simulating rotational degrees of freedom. Since the DVR-Gibbs approach increases efficiency by eliminating rejected moves and by decreasing the auto-correlation times of the Markov chain, we expect that the improvements exhibited in this work should be impervious to the lattice dimension in comparison to continuous Metropolis-Hastings Monte Carlo approaches.

As mentioned above, for this complexity analysis we have assumed that the number of MC steps and the number of beads is constant. While we expect that the higher dimensional lattice with longer range interactions will require larger numbers of beads and MC steps, away from criticality, this should yield another polynomial slowdown factor in the complexity scaling compared to the $1d$ nearest neighbors case. Again, this slowdown would also impact the continuous Metropolis-Hastings approach and so we expect that the DVR-Gibbs technique will retain its efficiency improvements in this context as well in comparison.

2.4 Concluding Remarks

We developed a path integral Monte Carlo simulation approach based on the discretization of continuous degrees of freedom and Gibbs sampling. The method is general and tested on a many-body problem, namely the dipolar planar rotor chain. The DVR is used as a discretization scheme and allows the representation of individual kinetic energy contributions as 1-body off-diagonal density matrices. The interaction potential is diagonal in the DVR which leads to a great simplification of its contribution to the path integral action. One key advantage of the DVR is that the path integral becomes a path sum and each state on the multidimensional grid has a finite probability. One can therefore sample the

configuration space of the path integral by constructing conditional probability tables and systematically sample all degrees of freedom without rejection using Gibbs sampling. The approach was initially tested for small chains with $N \leq 3$ where ED and NMM calculations are feasible. These calculations also allow one to determine the critical τ value above which the 1-body kinetic density matrix remains positive definite. We suggest performing such a test before embarking in many-body simulations with large N values. One can then extrapolate to $\tau \to 0$ by performing a series of simulations with different τ values (numbers of beads) for a given β. The method is tested for a large many-body system consisting of $N = 100$ interacting rotors. Grounds state energies and correlation functions are in excellent agreement with benchmark DMRG calculations for a broad range of g values. This system size is sufficiently large to exhibit a phase transition at a critical value of $g_c \sim 0.5$. Both the disordered phase and the ordered phase are accurately captured by our method. We observe that the use of Gibbs sampling allows for shorter decorrelation times than usual rejection based M-H sampling. This makes the new sampling scheme very advantageous for the simulation of complex materials. Indeed, the approach will be used to study the nature of water molecules trapped in beryl[3,45,97,98] and cordierite[4] in future work.

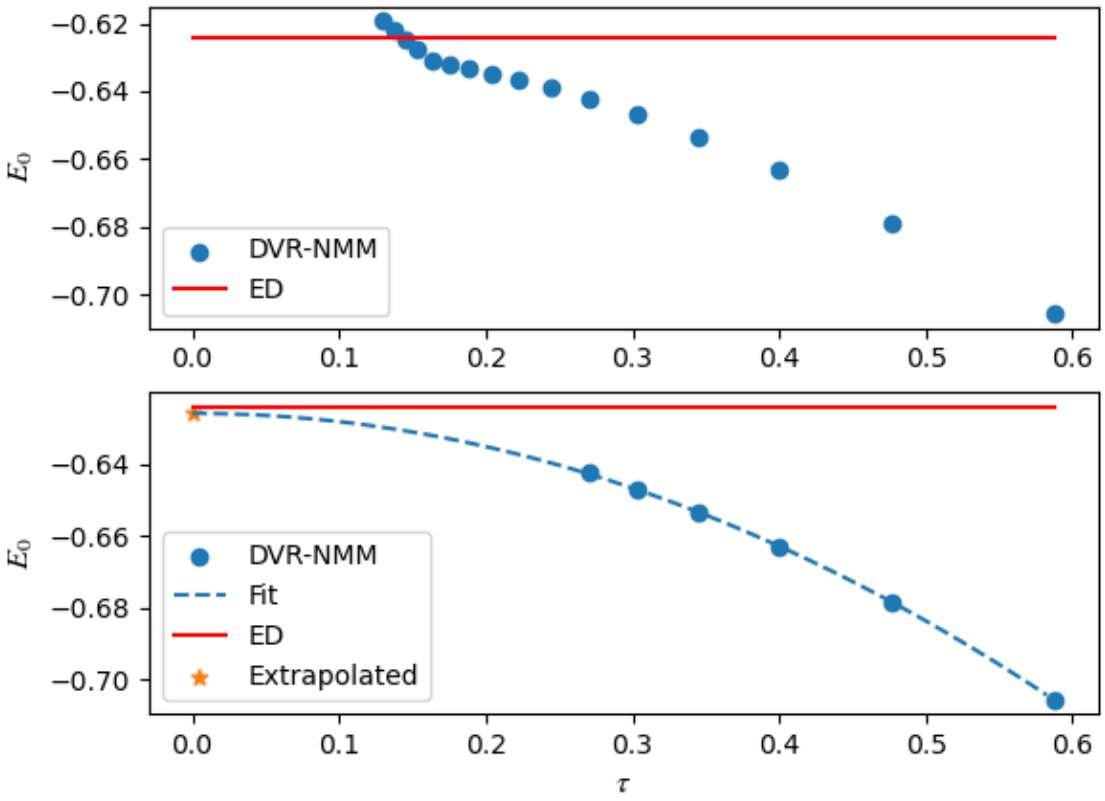


Figure 2.2: Convergence of the DVR-NMM E_0 with τ compared to ED results with maximum number of DVR grid points $L = 11$, $\beta = 10.0$ and $g = 0.6$ for $N = 2$ (top panel). Fit of the $\tau > 0.17$ results and extrapolation to $\tau = 0$ (bottom panel).

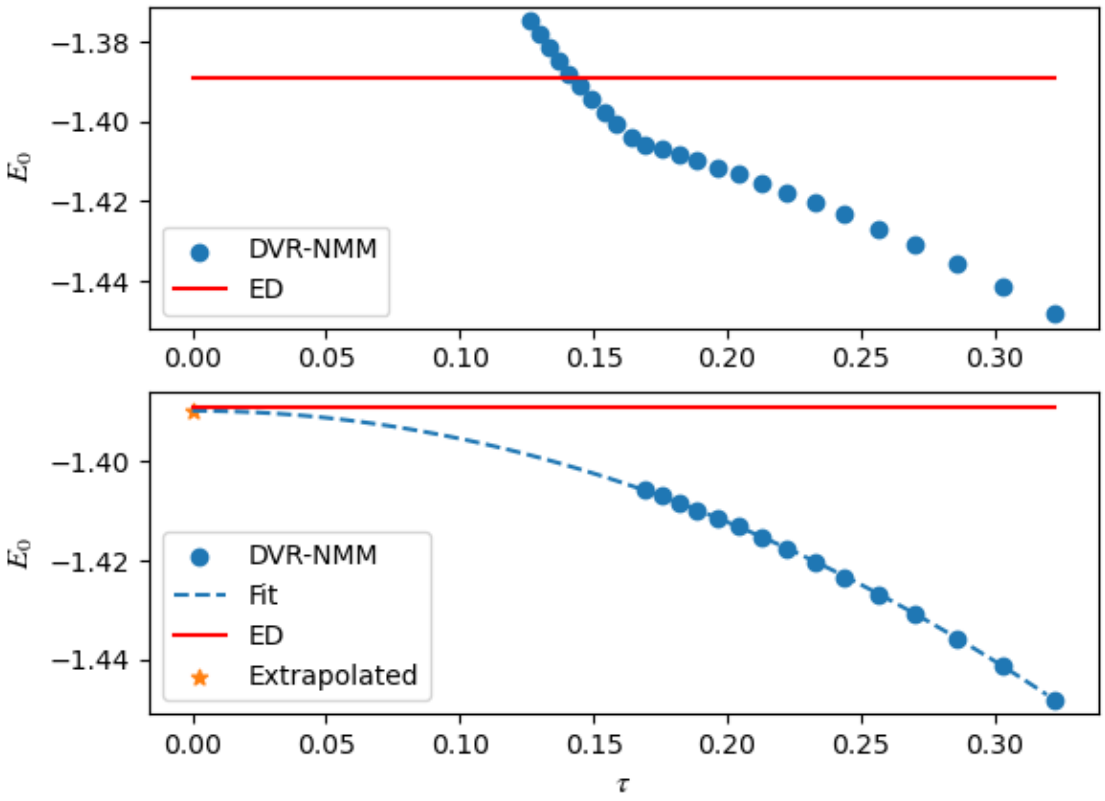


Figure 2.3: Same as Fig. 2.2 for $N = 3$ here.

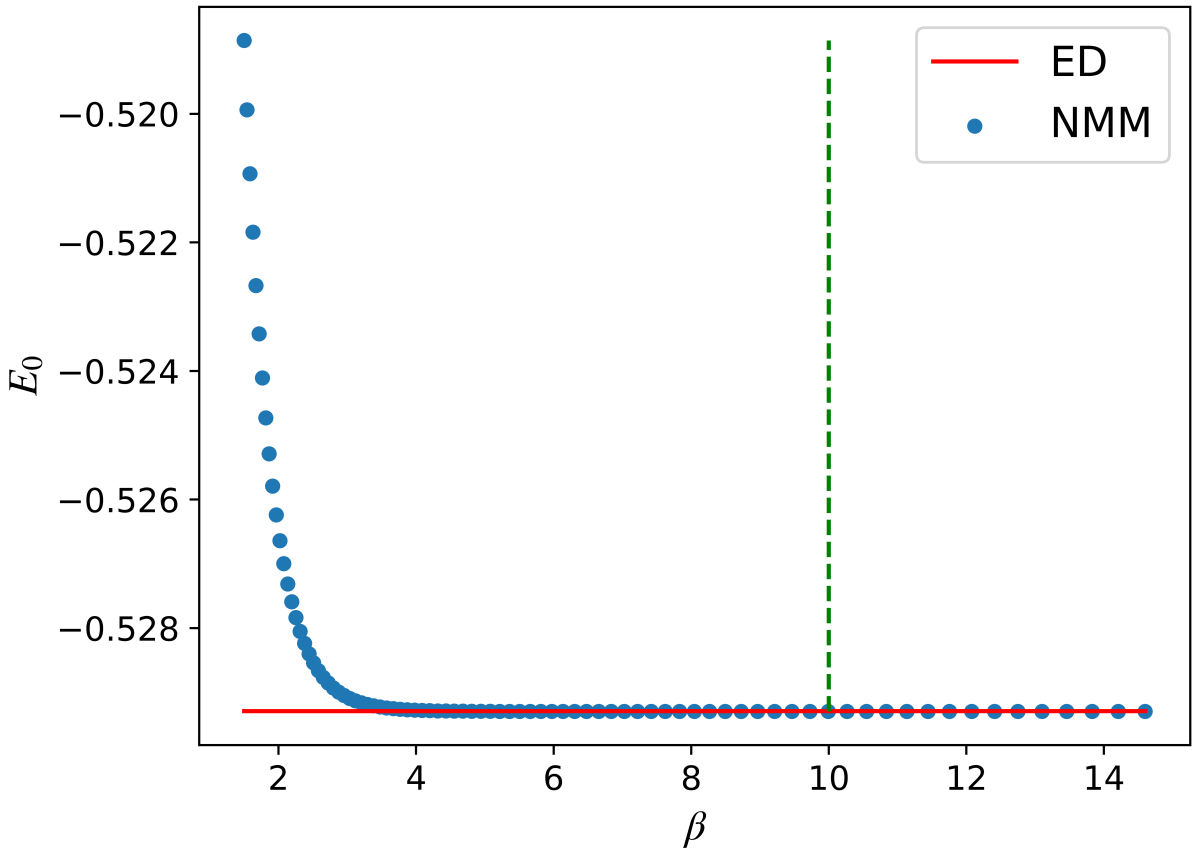


Figure 2.4: Convergence of the DVR-NMM E_0 with β compared to ED for $N = 2$ and $g = 1.0$. The NMM results were computed by fitting a sequence of seven DVR-NMM estimates corresponding to $\tau_t = 0.18 + 0.01t$ for $0 \leq t \leq 7$, $t \in \mathbb{Z}$ using: $E_\tau = E_0 + a\tau^2 + b\tau^4$. $\beta = 4.0$ appears to be sufficient for convergence. We use $\beta = 10.0$ for our analysis (highlighted in the figure).

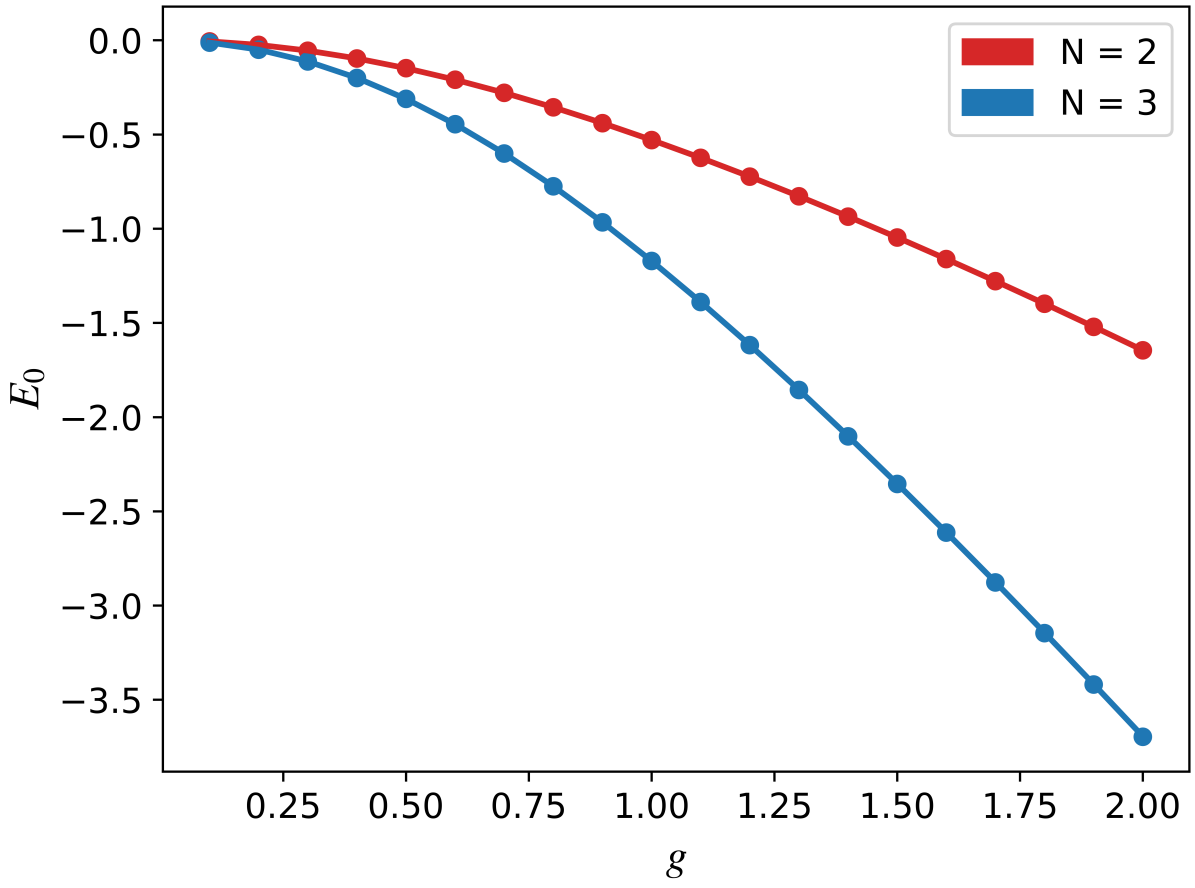


Figure 2.5: Ground state energy as a function of the coupling strength g computed using NMM for $N = 2$ and $N = 3$. The solid lines indicate the ED results while the points specify the NMM estimates (evaluated by extrapolating E_0 NMM estimates for small τ to 0). In both cases, the τ-extrapolated DVR-NMM results converge to the ED results for all $g \in (0.1, 2.0)$.

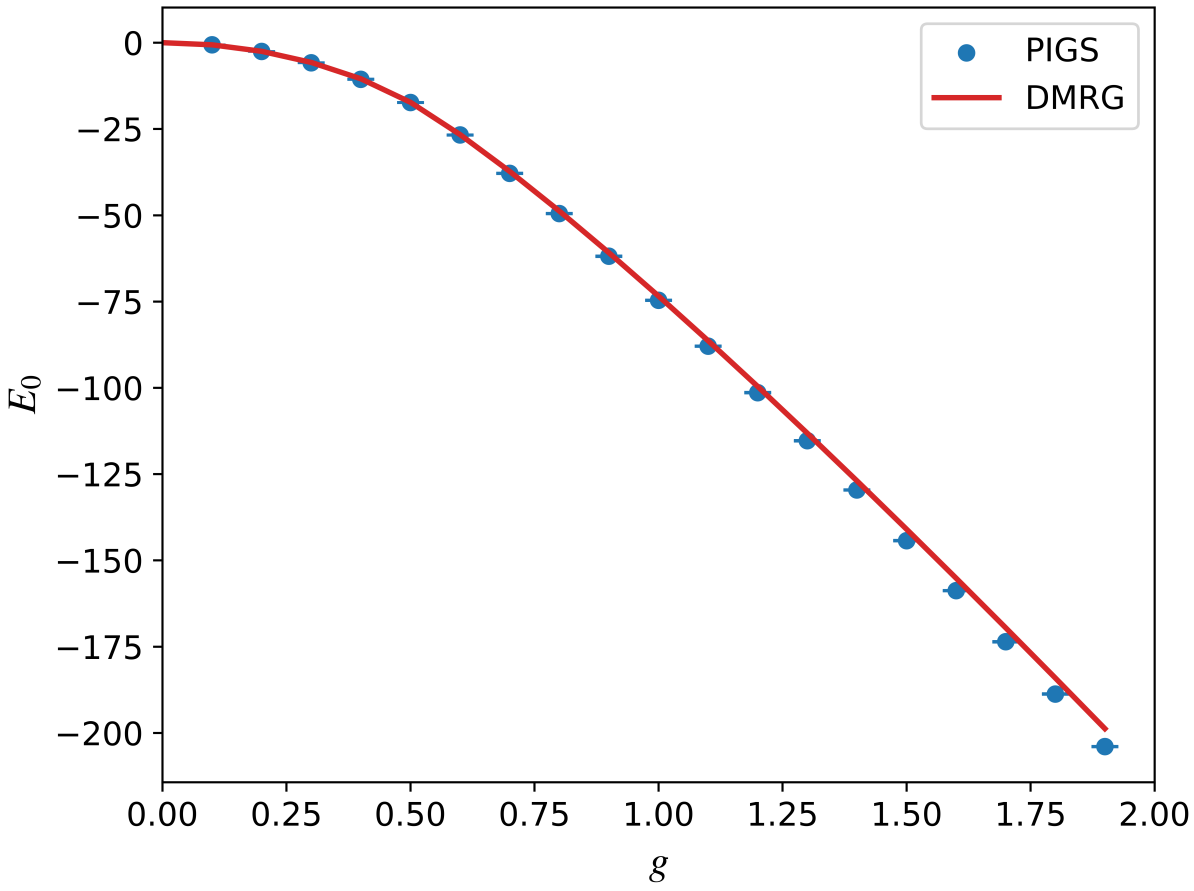


Figure 2.6: Ground state energy for $N = 100$, $P = 49$ computed using PIGS with DVR-Gibbs sampling. DMRG results plotted for comparison.

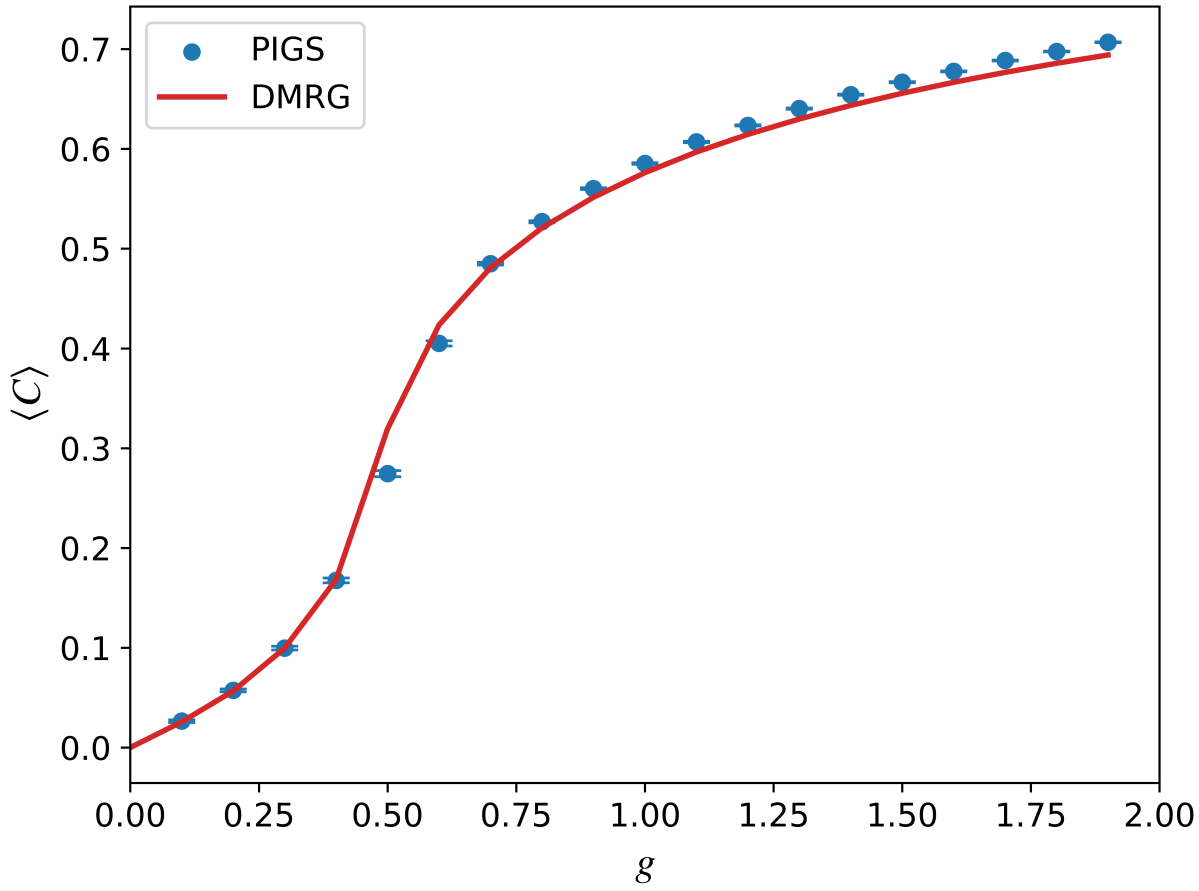


Figure 2.7: Correlation for $N = 100$, $P = 49$ computed using PIGS with DVR-Gibbs sampling. DMRG results are plotted for comparison.

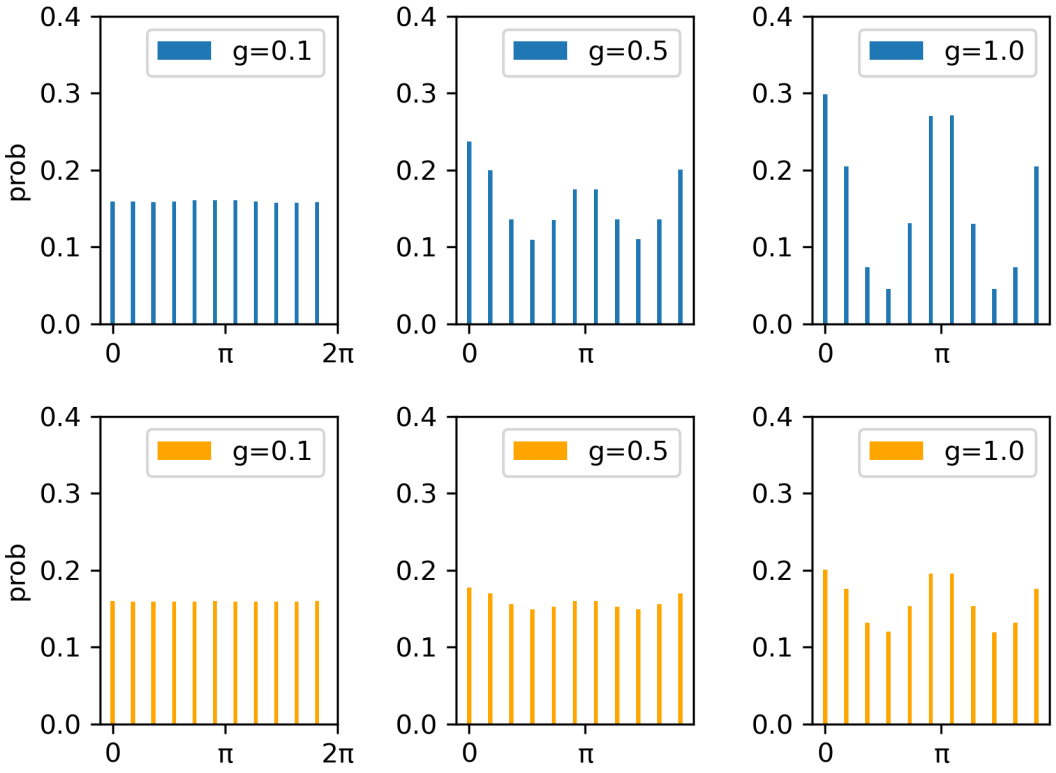


Figure 2.8: Angular distributions of the middlde beads (top panel) and end beads (bottom panel) for $N = 100$ with interactions strengths $g = 0.1, 0.5, 1.0$.

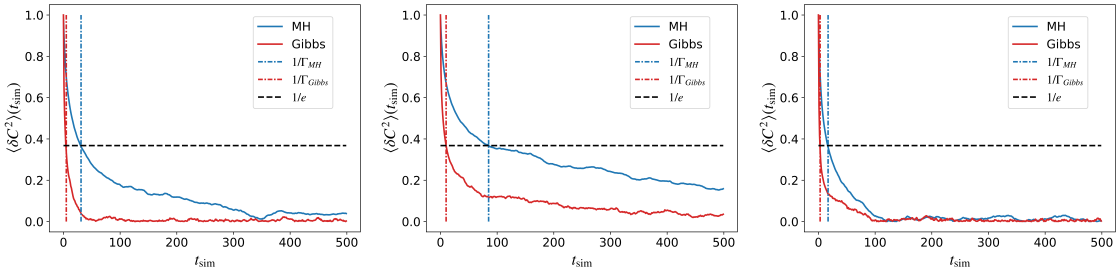
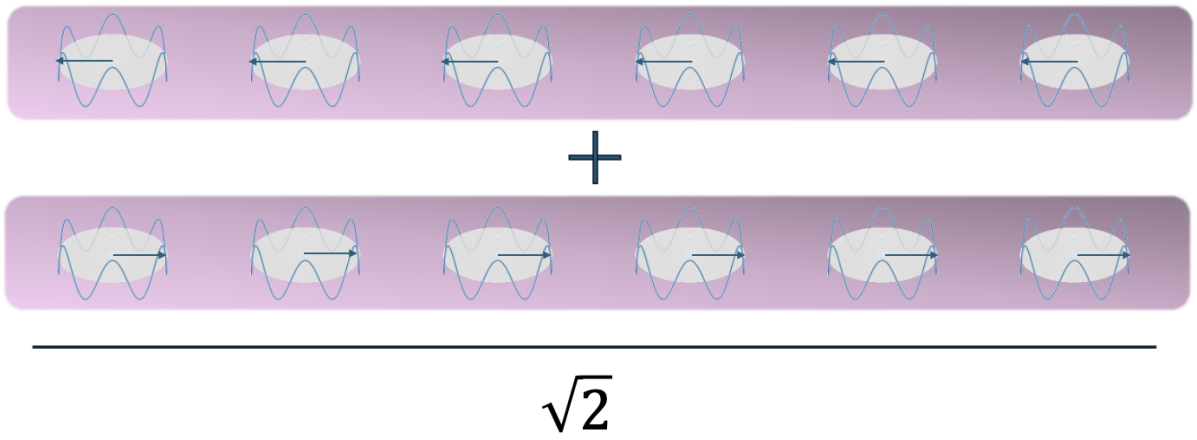


Figure 2.9: Markov chain autocorrelation for the M-H and Gibbs sampling algorithms computed using the orientational correlation for $g = 0.1$ (left panel), $g = 0.5$ (middle panel) and $g = 1.0$ (right panel). All three simulations used $N = 100$, $P = 48$ and 50000 simulation steps.

Chapter 3

Quantum critical behavior in chains of hindered dipolar planar rotors



This chapter has been reproduced from Wenxue Zhang, Muhammad Shaeer Moeed, Estevao De Oliveira, Hui Li, and Pierre-Nicholas Roy, "Quantum critical behavior of chains of hindered dipolar rotor", arXiv:submit/7974507. (submitted to J. Chem. Phys., MS JCP26-AR-03750; arXiv:2608.20501).

We study the ground-state properties of linear chains of dipolar planar rotors hindered by a six-fold on-site potential, a model motivated by water molecules confined in the hexagonal cavities of beryl. Using density matrix renormalization group (DMRG) calculations, we locate the quantum phase transition between the disordered and ferroelectrically ordered phases using the von Neumann entanglement entropy and the Binder ratio of the polarization. A sweep of the six-fold pinning strength shows that increasing hindrance shifts the critical dipolar coupling g_c to smaller values. These results suggest that crystal-field hindrance can promote, rather than suppress, dipolar ordering. This work has implications for ferroelectricity and quantum-device tuning in confined molecular rotors.

3.1 Introduction

Molecules confined in cavities of crystal structures such as beryl and cordierite can host a number of interesting quantum phases,[1–4,6,45,97,98,123] owing to the guest molecules' rotational degrees of freedom. For instance, previous work has suggested that confining water molecules in beryl suppresses the hydrogen bonding typically observed between water molecules. This suppression is caused by the small cavity size of the beryl structure.[7,45,124–127] This can allow the lattice of pinned water molecules to exhibit ferroelectric order, because of dipolar interactions between different (occupied) sites in the crystal.[3,11,128]

The orientational ordering phenomena of confined molecules are well-described by a lattice of rotors with dipolar interactions.[34,39,46] In particular, for pinned molecules in fullerenes, rotor lattices have proven to be a quantitatively accurate platform for examining the phase diagram in $1d$ chains.[9,33,35,38,99] Several computational and theoretical techniques have been developed in the past to study planar rotor assemblies.[34,35,96,99] Relevant examples include the Density Matrix Renormalization Group (DMRG)[100,101] as well as optimized path integral simulation techniques such as Gibbs sampling in a discrete variable representation (DVR).[96,106] DMRG was used to study the critical point of planar dipolar rotor chains with a $\mathbb{Z}_2$ symmetry. It was shown that these exhibit a $(1+1)d$ Ising universality class transition at a critical coupling strength $g_c \approx 0.5$.[99]

In crystals such as beryl, the confining cavity has a hexagonal structure.[123] Moreover,

these cavities are typically only large enough to accommodate a single water molecule each. Recent Inelastic Neutron Scattering (INS) experiments suggest that due to the hexagonal structure of the confining cavity,[45,124] the crystal structure cannot be entirely neglected. Additionally, the distance between the confined molecules and the cage is relatively small. The cavity geometry constrains the dipole along the six edges of the hexagonal cage. This crystal-induced anisotropy can be effectively modeled using a six-fold on-site local potential. This is consistent with the close alignment between the experimental and the six-fold potential model low-energy spectra.[1,3,4,123] While DMRG is ideally suited to the effectively one-dimensional chains considered here, we note that extensions to higher-dimensional lattices will require alternative approaches such as path integral Monte Carlo.[32,39–42,46,57,96,103,129]

In the present work, we perform large-scale DMRG simulations to examine the effect of this six-fold potential on the phase diagram of a coplanar chain of dipolar rotors (see Fig. 3.1). We find that in the $\mathbb{Z}_2$ chain, the strength of the constraining six-fold potential shifts the critical point in the dipolar coupling strength g. Increasing the strength of the six-fold potential shifts the onset of ferroelectric order to smaller values of g. This implies that a larger class of confined molecular species than previously considered has the potential to exhibit spontaneous alignment of dipole moments. To study this quantitatively, we use the Binder ratio[35,130,131] of the polarization, as well as the entanglement entropy.[132–134] These two measures exhibit a sharp transition from the disordered to the ordered phase and are key quantities for the determination of critical points in $(1+1)d$ Ising universality class transitions.[35,51,99,135]

The remainder of this paper is organized as follows: in Sec. 3.2, we discuss the exact form of the Hamiltonian and the behavior of the ground state in various limits. In Sec. 3.3, we quantitatively characterize the effect of the six-fold potential on the critical point using our DMRG calculations. Finally, in Sec. 3.4, we conclude and discuss future research directions.

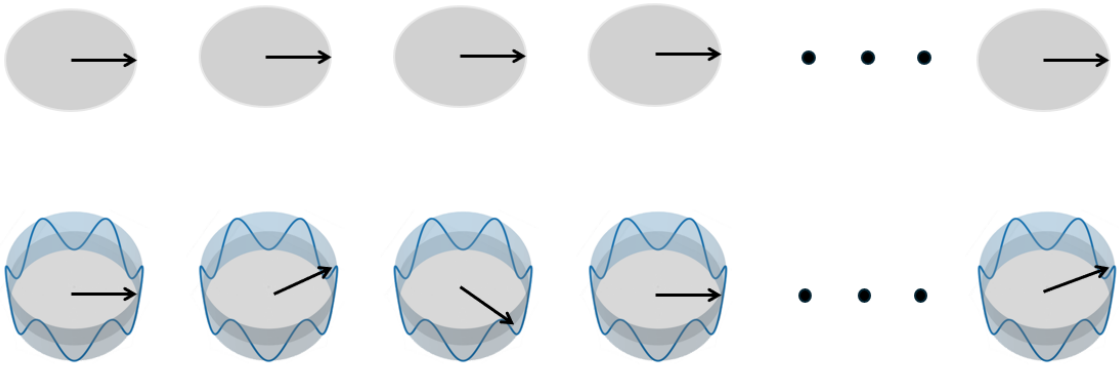


Figure 3.1: Schematic of a coplanar chain of dipolar planar rotors, each subject to a six-fold hindering potential.

3.2 Theory

3.2.1 System Hamiltonian

We consider a one-dimensional ($1d$) chain of N planar rotors with nearest-neighbor dipolar interactions. Each rotor is hindered by a six-fold (hexagonal) on-site potential. This potential models the anisotropy induced by the background crystal structure. The system Hamiltonian is

$$H = \sum_{i=1}^{N} \left(\frac{B}{\hbar^2} \hat{L}_{z,i}^2 - \frac{A'}{2} \big(\cos(6\phi_i) - 1 \big) \right) + \frac{|\mu|^2}{4\pi\epsilon_0 R^3} \sum_{i=1}^{N-1} \hat{V}_{i,i+1}, \tag{3.1}$$

where $\hat{L}_{z,i} = -i\hbar\partial_{\phi_i}$ is the planar rotor angular momentum operator and ϕ_i is the angle that parametrizes the orientation of rotor i. The parameter B is the rotational constant of the rotor, A' is the barrier height of the six-fold hindering potential, μ is the dipole moment of a rotor, and R is the inter-rotor distance.

The nearest-neighbor dipolar interaction, $\hat{V}_{i,i+1}$, is defined as

$$\hat{V}_{i,i+1} = \left[\hat{y}_i\hat{y}_{i+1} - 2\hat{x}_i\hat{x}_{i+1}\right], \tag{3.2}$$

where the constrained Cartesian position operators $(\hat{x}_i, \hat{y}_i)$ of each rotor are conveniently expressed in polar coordinates as $(\cos(\phi_i), \sin(\phi_i))$. With this sign convention, head-to-tail alignment of the dipoles along the chain axis is energetically favored. This alignment determines the structure of the ordered phase discussed below. This representation of the problem is depicted in Fig. 3.1, which shows a chain of rotors, each with its own six-fold localization potential.

Note that the $1/R^3$ dipolar interaction is truncated at nearest neighbors. The neglected next-nearest-neighbor coupling is suppressed by a factor of $2^3 = 8$. We therefore expect only a small quantitative error. Also note that the six-fold potential of Eq. (3.1) places two of its six minima along the chain axis ($\phi = 0, \pi$). These are the orientations favored by the dipolar interaction. This alignment maximizes the cooperation between hindrance and dipolar order. A relative misalignment between the crystal-field minima and the chain axis would weaken this cooperation and may lead to different order. A quantitative study of this effect will be the subject of future work.

It is convenient to work in reduced units by dividing Eq. (3.1) by B. Since the six-fold potential is a single-body operator, it can be absorbed into the monomer Hamiltonian

$$\hat{h}_i^{1\mathrm{B}} = -\frac{\partial^2}{\partial\phi_i^2} \underbrace{-\frac{A}{2}\big(\cos(6\phi_i) - 1\big)}_{\hat{V}_{6,i}}, \tag{3.3}$$

where $A = A'/B$ denotes the reduced barrier height. Defining the dimensionless dipolar coupling strength

$$g = \frac{|\mu|^2}{B\ 4\pi\epsilon_0 R^3}, \tag{3.4}$$

the reduced Hamiltonian takes the compact form

$$\frac{\hat{H}}{B} = \sum_{i=1}^{N} \hat{h}_i^{1\mathrm{B}} + g\sum_{i=1}^{N-1} \hat{V}_{i,i+1}. \tag{3.5}$$

Note that no separate definition of the six-fold potential is required, as the hindering term is contained entirely in $\hat{h}_i^{1B}$ of Eq. (3.3).

For our DMRG calculations, we use the momentum basis, which diagonalizes the angular momentum operator as follows

$$\hat{L}_{z,i}^2 = \sum_{m=-\infty}^{\infty} m^2 |m\rangle\langle m|. \tag{3.6}$$

Previous work has examined ground-state properties of free planar rotor chains with a dipole interaction.[99] There, a symmetric momentum cutoff $l = m_{\max} = -m_{\min} = 4$ was shown to yield quantitatively accurate results. For the chain of hindered rotors with the same dipole interaction, we use a similar approach. However, since the spectrum behaves differently in the presence of the six-fold potential, we anticipate that the value of l needed for convergence will be different. Based on the monomer convergence analysis of Sec. 3.3, we adopt $l = m_{\max} = 16$ in this work.

In this finite momentum representation, the dipole interaction takes the form

$$\begin{aligned}\hat{V}_{i,i+1} = &-\frac{1}{4} \sum_{m_i, m_{i+1}} |m_i + 1, m_{i+1} - 1\rangle\langle m_i, m_{i+1}| \\ &-\frac{3}{4} \sum_{m_i, m_{i+1}} |m_i + 1, m_{i+1} + 1\rangle\langle m_i, m_{i+1}| + h.c.,\end{aligned} \tag{3.7}$$

where the sums over m_i and m_{i+1} go from $-l$ to l. In the same basis, the total six-fold hindering potential, defined through $\hat{V}_{6,i}$ of Eq. (3.3), is represented as

$$\sum_{i=1}^{N} \hat{V}_{6,i} = -\frac{A}{4} \sum_{i=1}^{N} \left(\sum_{m_i=-l}^{l} |m_i + 6\rangle\langle m_i| + h.c. - 2 \right), \tag{3.8}$$

while the kinetic term is diagonal with eigenvalues m_i^2. Under the momentum cutoff, matrix elements with $|m_i + 6| > l$ are discarded.

3.2.2 Estimators

In this work, we are interested in the ground-state phase diagram of the system defined above. For the dipolar chain of free rotors ($A = 0$), previous work has shown that there

is a $(1+1)d$ Ising universality class Quantum Phase Transition (QPT) at $g \approx 0.5$.[35,46,51] This transition separates the disordered ($g < 0.5$) and ordered ($g > 0.5$) phases, in the thermodynamic limit ($N \to \infty$). Note that the dipolar interaction explicitly breaks the $U(1)$ symmetry of the free rotor system down to $\mathbb{Z}_2$. As g increases, this QPT results as a consequence of the spontaneous breaking of this $\mathbb{Z}_2$ symmetry.

To study the phase diagram and the behavior of this transition in the presence of the six-fold potential, we use the Binder ratio and the entanglement entropy. The former is typically used in many-body physics for accurately estimating the critical point.[35,130,131] It is defined as follows:

$$U_x = 1 - \frac{\langle M_x^4 \rangle}{3 \langle M_x^2 \rangle^2}, \tag{3.9}$$

where $M_x = \sum_{i=1}^{N} \cos(\phi_i)/N$ is the polarization of the rotors along the chain. In the ordered phase, the Binder ratio approaches $U_x = 2/3$. It serves as a sharp diagnostic of the QPT, for which the polarization M_x is the order parameter.

Note that deep in the disordered phase, as $N \to \infty$, we expect the polarization to be normally distributed since the ground state is well approximated by the limit:

$$|\psi_0\rangle = \bigotimes_{i=1}^{N} |E_0^i\rangle. \tag{3.10}$$

Here, $|E_0^i\rangle$ is the ground state of the ith rotor. This can be seen by taking the limit $g \to 0$. That limit yields a lattice of non-interacting rotors. In the absence of the six-fold potential, this is simply the angular momentum eigenstate $|m = 0\rangle$. Since the rotors in this limit are decoupled, M_x is the average of N independent and identically distributed random variables. Therefore, M_x tends to a normal distribution in the thermodynamic limit. The Binder ratio is 0 by definition in that case.

Conversely, in the presence of $\mathbb{Z}_2$ order, the ground state for a finite chain in the limit of $g \to \infty$ is:

$$|\psi_0\rangle = \frac{1}{\sqrt{2}} \left(\bigotimes_{i=1}^{N} |\phi_i = 0\rangle + \bigotimes_{i=1}^{N} |\phi_i = \pi\rangle \right). \tag{3.11}$$

To see this, note that the orientations associated with each state in the superposition above correspond to the minima of the dipolar interaction term. That term dominates

the Hamiltonian in the limit $g \to \infty$. It is then clear that $\langle M_x^4 \rangle = \langle M_x^2 \rangle = 1$, which corresponds to $U_x = 2/3$. It is instructive to note that while our discussion here refers to a chain with finite N, the QPT only exists in the limit of $N \to \infty$. Moreover, the spontaneous development of order implies that one of the two states in the superposition in Eq. (3.11) then represents the ground state. This yields a non-zero order parameter (polarization). However, the conclusions about the Binder ratio remain the same in this case since it is an even function of the polarization. This is also why it is an effective probe of the QPT and the ordered phase in finite size systems with large N.

Another useful measure of critical phenomena in this system is the bipartite von Neumann entanglement entropy defined as:

$$S_{\text{vN}} = -\text{Tr}_A(\rho_A \ln(\rho_A)), \quad \rho_A = \text{Tr}_B(\rho). \tag{3.12}$$

Here, ρ_A is the reduced density matrix corresponding to subsystem A, and Tr_A, Tr_B represent the partial trace over subsystems A and B, respectively. At $T = 0$, the density matrix of the entire system is simply determined by the ground state $|\psi_0\rangle$ as: $\rho = |\psi_0\rangle\langle\psi_0|$. For our analysis, we will set subsystems A and B to be the first and second sets of consecutive $N/2$ sites in the N rotor chain, respectively. In the disordered phase, since the ground state (see Eq. (3.10)) is separable, the entanglement entropy is 0. In the ordered phase, for finite N, note that:

$$\rho_A = \frac{1}{2}\left(\bigotimes_{i=1}^{N/2} |0_i\rangle\langle 0_i| + \bigotimes_{i=1}^{N/2} |\pi_i\rangle\langle \pi_i|\right), \tag{3.13}$$

expressed in the position basis, which implies a von Neumann entropy of $S_{\text{vN}} = \ln(2)$. Away from the critical point the chain is gapped and the bipartite entanglement entropy obeys an area law, saturating with subsystem size. At the critical point, however, the gap closes. The entanglement entropy then grows logarithmically with subsystem size, $S_{\text{vN}} \sim (c/6) \ln N$. The central charge is $c = 1/2$ for the $(1+1)d$ Ising universality class.[99,132,134] This logarithmic peak makes the entanglement entropy a powerful probe of the phase diagram of the rotor chain. This is relevant both in the presence and in the absence of the six-fold potential.

3.3 Results and Discussion

3.3.1 Monomer

We first solve the monomer problem to establish the basis size required to converge the first few eigenstates and determine where they lie with respect to the reduced barrier height A. Neutron diffraction difference-Fourier maps of the proton density in beryl reveal a six-fold-modulated, delocalized distribution.[45] This observation motivates a quantitative analysis of the monomer levels in a six-fold potential.

We compute the eigenvalues of the monomer Hamiltonian of Eq. (3.3) for barrier heights up to $A = 80$, the largest value considered in the present work. We report the error in the tunneling splitting, $\Delta = E_1 - E_0$, for $m_{\max} = 16$ in Table 3.1.

Table 3.1: Convergence of the single-rotor tunneling splitting $\Delta = E_1 - E_0$ with respect to the size of the angular-momentum basis. Values obtained at $m_{\max} = 16$ are compared with converged results ($m_{\max} = 90$).

A	Δ (converged)	Δ ($m_{\max} = 16$)	$\lvert\delta\Delta\rvert$	Error (%)
20	0.8498913	0.8498941	2.86×10^{-6}	0.00034
40	0.5728426	0.5729498	1.07×10^{-4}	0.019
60	0.3525340	0.3531961	6.62×10^{-4}	0.188
80	0.2134483	0.2155106	2.06×10^{-3}	0.966

The distribution of energy levels (and their degeneracies) in the six-fold potential is illustrated in Fig. 3.2 for $A = 20$. With this value, six states have an energy below the barrier. As depicted in Fig. 3.3, n_{bb} reaches 6 when $A \approx 18$ and stays on this first plateau until $A \approx 38$. Upon further increase to $A \approx 70$, n_{bb} climbs to 12, forming a second plateau. Each plateau corresponds to a filled manifold of six (nearly degenerate) well-localized states, one per minimum of the six-fold potential. When the six-fold potential is relatively small, as shown in Fig. 3.3, only the ground state lies below the barrier of the cosine potential. To enable the dipole rotor to tunnel from the current orientation to another local minimum, it

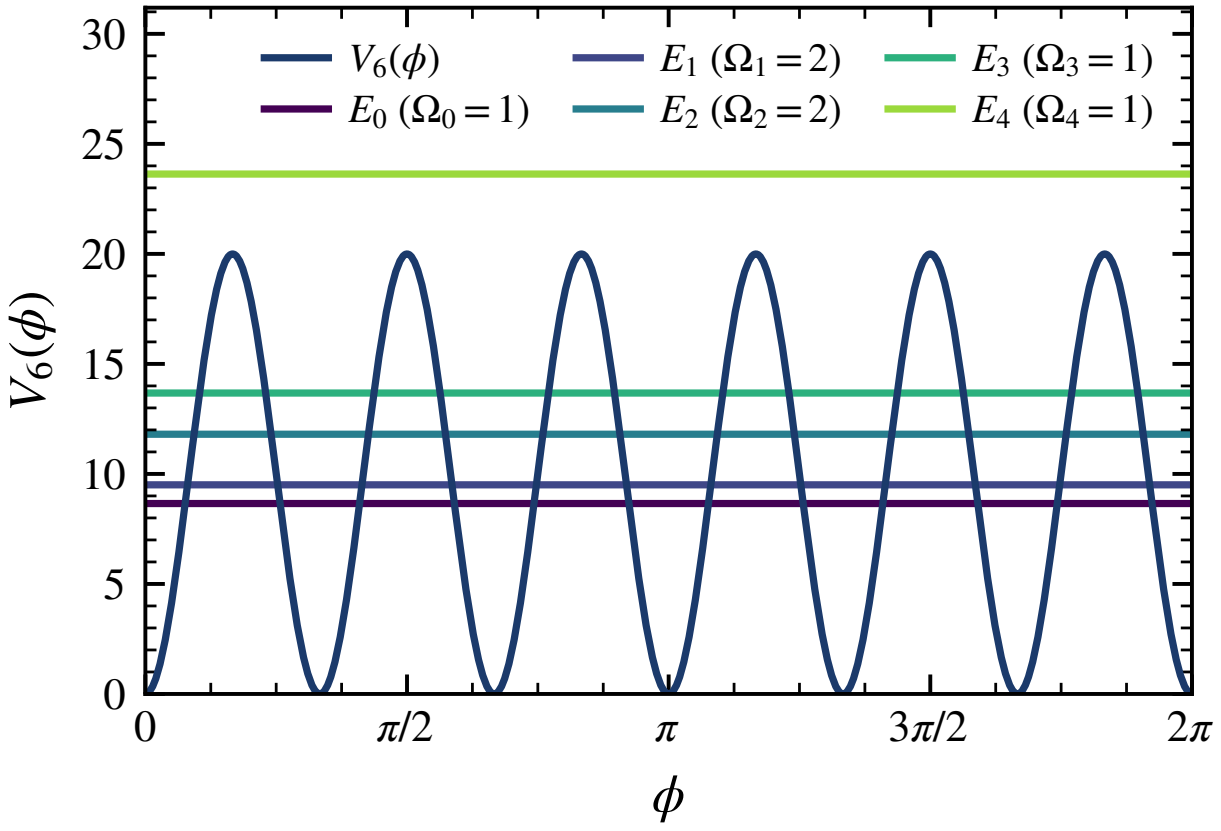


Figure 3.2: Energy levels of a single rotor in a six-fold potential with the barrier height $A = 20$; Ω_i denotes the degeneracy of each level. Based on the convergence tests, $m_{\max} = 16$ is used.

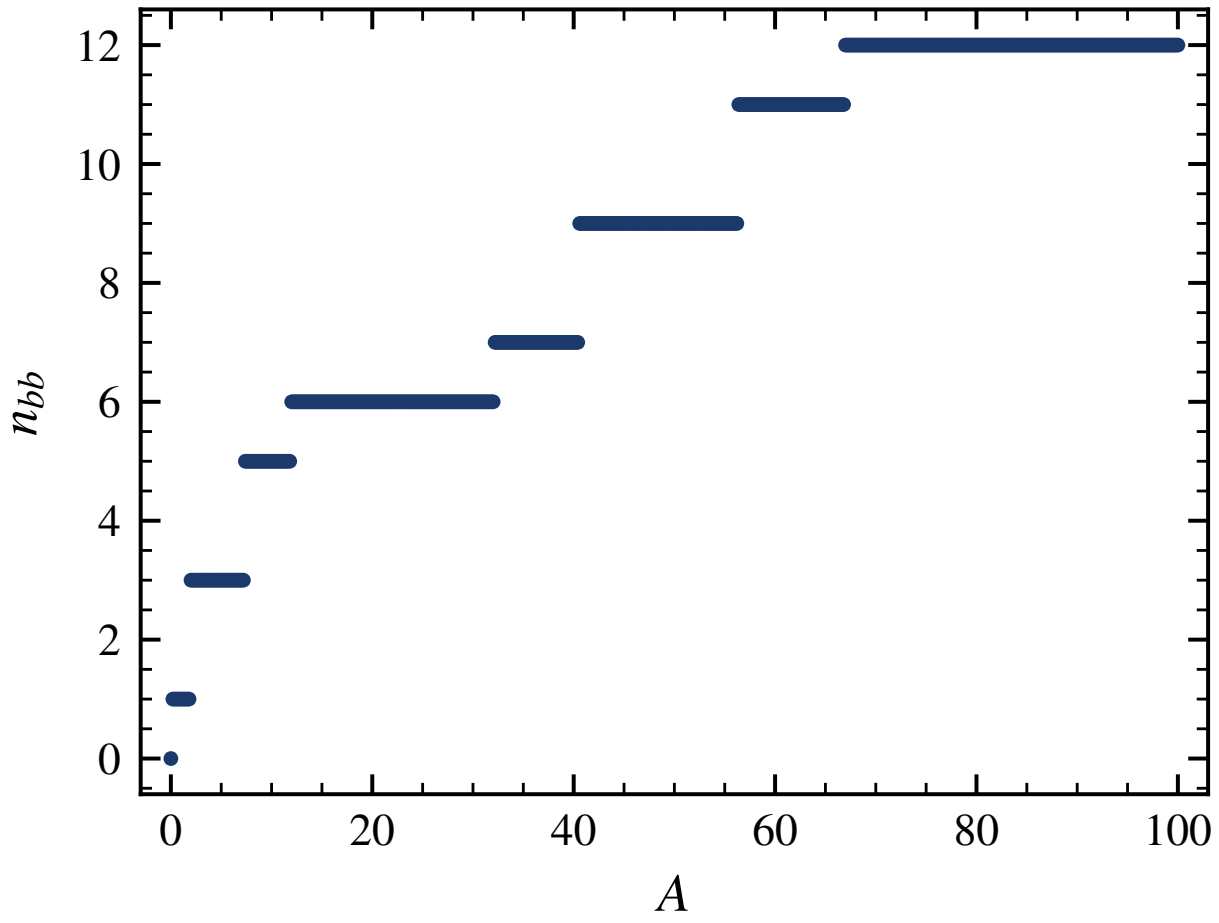


Figure 3.3: Number of states below the barrier (n_{bb}) as a function of the six-fold (reduced) barrier height A.

is sufficient to excite the dipole to the first excited state. Increasing A brings more excited states below the barrier. Model calculations accompanying the INS experiments predict tunneling transitions at 2.7, 10.1 and 16.7 meV, the first two doubly degenerate.[45] Thus, reorientation between wells proceeds either by tunneling within the below-barrier manifold or by kinetic excitation above the barrier. The number of below-barrier states controls which channel dominates.

3.3.2 Longer chains: $N = 50$

In order to optimize the MPS representation of the ground states, we employ a two-site DMRG algorithm as implemented in ITensor.[121] An SVD threshold of 10^{-8} and a relative energy cut-off of 10^{-8} are used. Local Hilbert spaces are described by a plane wave eigenbasis with $m_{\max} = 16$. This basis size was established by converging the monomer eigenstates in the preceding subsection. The maximum bond dimension retained during the sweeps was 200, and 100 sweeps were sufficient to converge the ground-state energy to the stated tolerance. We also verified for representative points at the largest A and g that increasing the momentum cutoff beyond $m_{\max} = 16$ leaves the reported observables unchanged. Deep in the ordered phase the ground state becomes nearly two-fold degenerate. The sweeps reported here converge to the symmetric superposition of Eq. (3.11). This is consistent with the observed plateaus $U_x \to 2/3$ and $S_{\mathrm{vN}} \to \ln 2$. The moments $\langle M_x^2 \rangle$ and $\langle M_x^4 \rangle$ were evaluated directly from the converged MPS as expectation values of the corresponding operator sums.

Fig. 3.4 shows the von Neumann entropy S_{vN} as a function of the dipolar coupling g for several reduced barrier heights A at $N = 50$. As A increases, the transition shifts to smaller g compared with free rotors ($A = 0$), for which $g_c \approx 0.5$.[51,99] In particular, for larger A the entropy reaches its plateau at smaller g. This demonstrates the tuning capability offered by hindered dipolar rotors.

The Binder ratio U_x (Fig. 3.5) is computed for the same barrier heights ($A = 0, 20, 40, 60, 80$) and the same DMRG parameters. It displays the analogous trend. The plateau at $U_x = 2/3$ is reached at smaller g as A increases. The critical couplings $g_c(A)$, extracted from the maximum gradient of the Binder ratio, are collected in the phase diagram of Fig. 3.6.

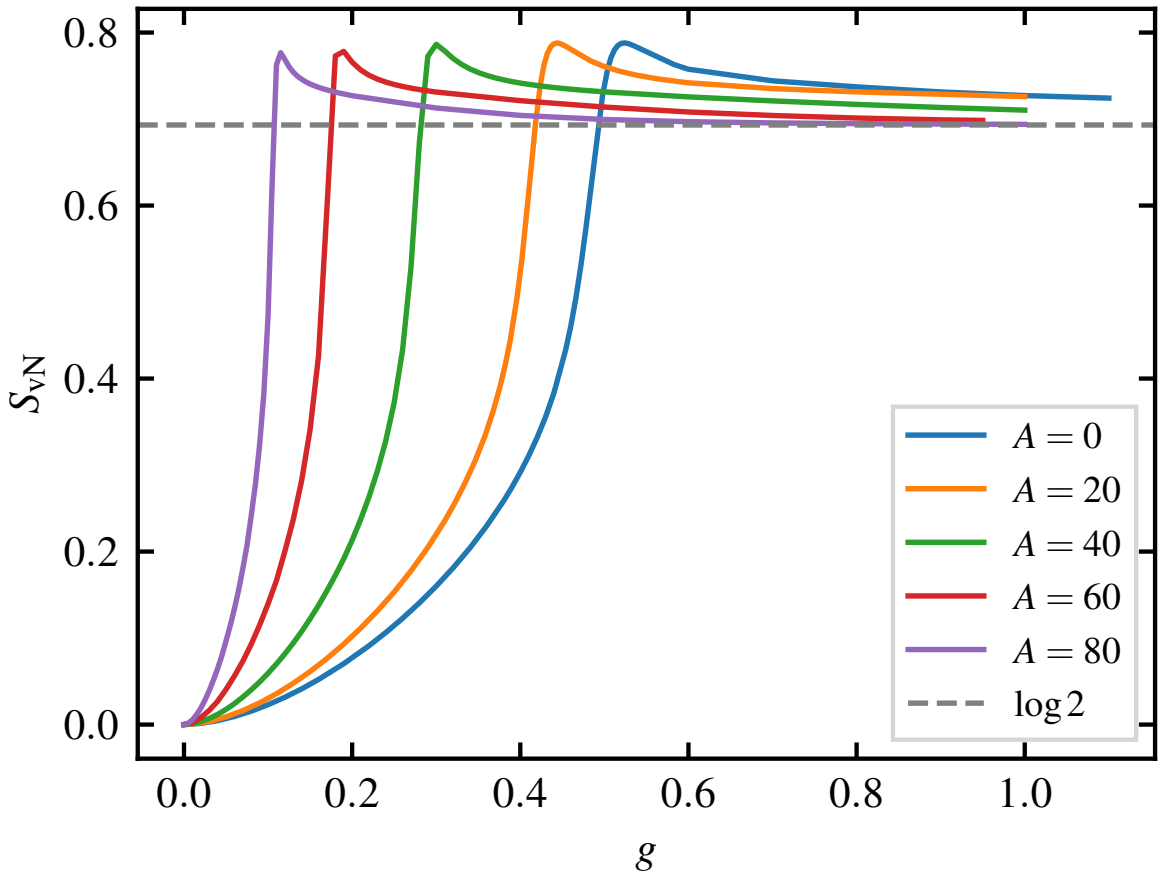


Figure 3.4: Von Neumann entropy S_{vN} as a function of g for $A = 0, 20, 40, 60, 80$, and $N = 50$.

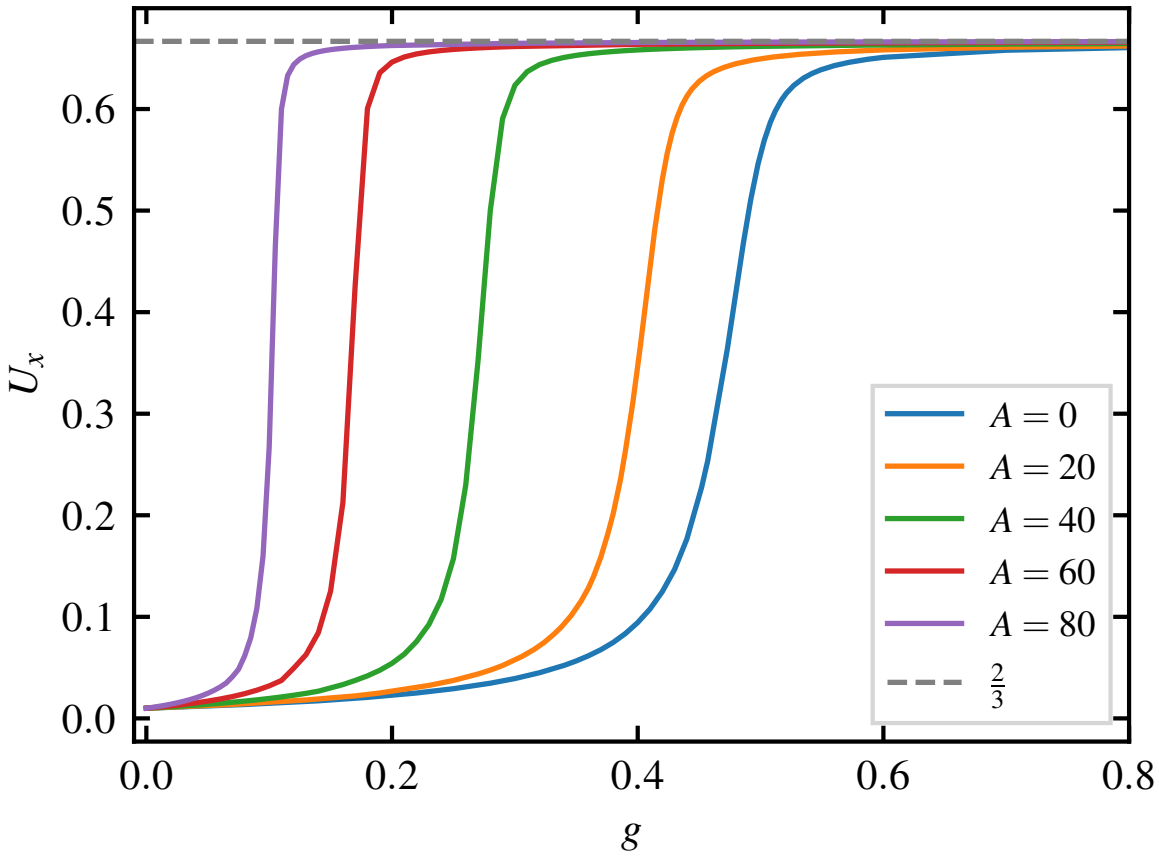


Figure 3.5: Binder cumulant U_x as a function of the dipolar coupling g for $A = 0, 20, 40, 60, 80$ and $N = 50$.

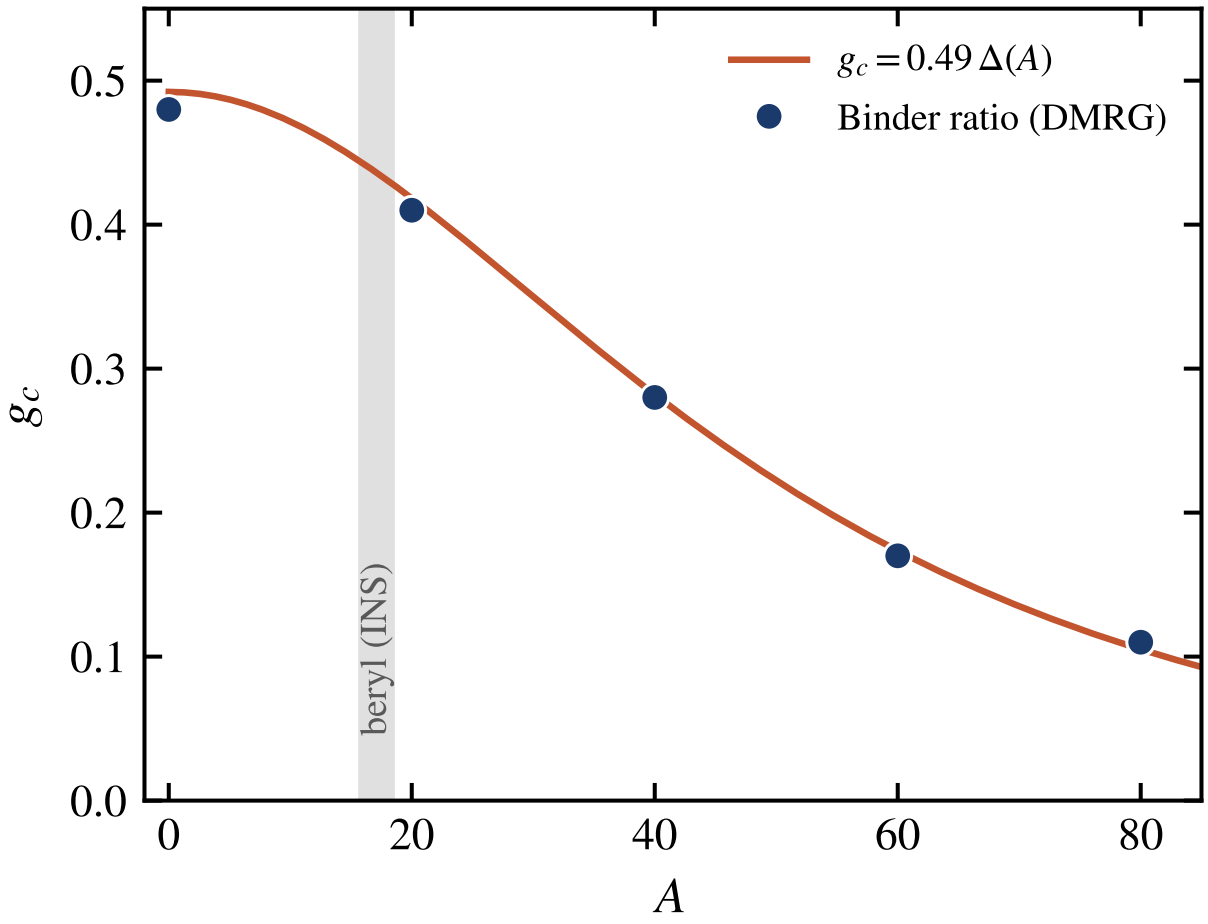


Figure 3.6: Critical coupling g_c as a function of the reduced barrier height A. Symbols: g_c from the maximum gradient of the Binder ratio at $N = 50$ (Fig. 3.5). Solid line: the scaling form $g_c = a\,\Delta(A)$ of Eq. (3.14) with $a = 0.49$, where $\Delta(A) = E_1 - E_0$ is the tunneling splitting of the monomer Hamiltonian of Eq. (3.3). The $A = 0$ point is not included in the fit; the form nevertheless recovers the free-rotor value $g_c \approx 1/2$ there, since $\Delta(0) = 1$. The shaded band marks the beryl barrier range $A \approx 16$–18 from inelastic neutron scattering,[45] where the fit gives $g_c \approx 0.44$.

The dependence of the critical coupling on the barrier height is captured by a simple scaling relation. For each barrier height, g_c is extracted from the maximum gradient of the Binder ratio $U_x(g)$ at $N = 50$ (Fig. 3.5). Independently, the monomer tunneling splitting $\Delta(A) = E_1 - E_0$ is obtained by exact diagonalization of the monomer Hamiltonian of Eq. (3.3). A converged momentum cutoff is used ($m_{\max} = 90$, cf. Table 3.1). The ratio g_c/Δ is found to be constant over the entire range of barriers studied, so that

$$g_c(A) \simeq a\,\Delta(A), \qquad a = 0.49, \tag{3.14}$$

where a is the mean of g_c/Δ over $A = 20$–80. This form interpolates the computed points and fixes both asymptotes. In the free-rotor limit $\Delta(0) = 1$ one recovers $g_c = 1/2$. For large barriers Δ decays exponentially and the ordered phase extends to arbitrarily weak coupling. The relation is analogous to the transverse-field-Ising case. The dipole operator couples the monomer ground state to the first excited level (the dipole-active member of the lowest sextet). At low energies, each hindered rotor therefore acts as a two-level system with gap $\Delta(A)$. Criticality occurs when the dipolar coupling balances this quantum-fluctuation scale at $g_c \simeq \Delta(A)/2$. The solid line in Fig. 3.7 is Eq. (3.14) evaluated on a dense grid of barrier heights. At the beryl-relevant barrier, it yields $g_c \approx 0.43$, well below the estimated physical coupling $g \approx 0.90$.

Table 3.2: Reported values of the in-plane orientational barrier for type-I water in beryl. The different methods extract different quantities (see text). For orientation, 1 meV $\approx$ 8.07 cm^{-1} $\approx$ 11.6 K.

Method	Quantity extracted	Value (meV)
INS (tunneling)[45]	barrier between minima (static)	≈ 176
INS (tunneling)[45]	barrier between minima (vibration-lowered)	48–56
Two-level model[1,2,3]	six-fold barrier V_b (bounds adopted from Ref. 45)	56–176
THz spectroscopy[3]	six-well depth (fit)	1.41 ± 0.05
DFT[3]	six-well depth (DFT)	≈ 0.83
Dielectric relaxation[1,2,4]	reorientation activation energy	170 ± 1.5

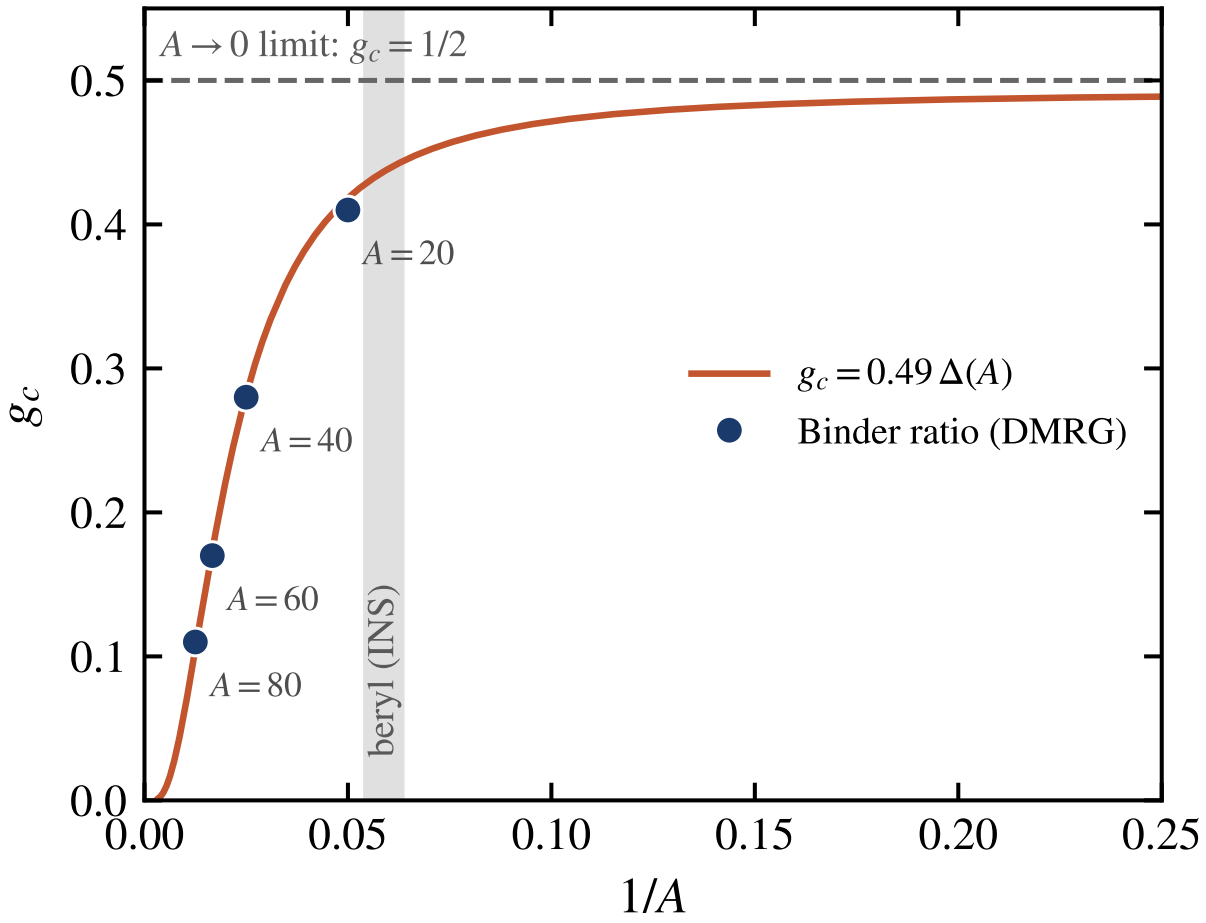


Figure 3.7: Critical coupling g_c as a function of the inverse reduced barrier height $1/A$. Symbols: g_c extracted from the maximum gradient of the Binder ratio at $N = 50$ (Fig. 3.5). Solid line: the single-parameter form $g_c = a\,\Delta(A)$ with $a = 0.49$, where $\Delta(A) = E_1 - E_0$ is the tunneling splitting of the monomer Hamiltonian of Eq. (3.3). The line extrapolates the phase boundary at both ends: for $A \to \infty$ ($1/A \to 0$) the splitting, and with it g_c, vanishes exponentially, while for $A \to 0$ ($1/A \to \infty$) it approaches the free-rotor limit $g_c = 1/2$ (dashed line), since $\Delta(0) = 1$ exactly. The shaded band marks the barrier range $A \approx 16$–18 inferred for water in beryl from inelastic neutron scattering,[45] for which the scaling form gives $g_c \approx 0.43$.

3.3.3 Connection to beryl parameters

Earlier studies on the vibrational energy levels of confined water molecules in beryl demonstrated that these water molecules form virtually negligible hydrogen bonds with the cage wall.[126] Subsequently, Raman spectroscopic analysis indicated that type-I water molecules exhibit a certain degree of motion at a frequency that can be approximated by the "particle-in-a-box" model. The corresponding frequencies suggest that the water molecules undergo anisotropic rotation about at least two of the three possible rotational axes within the cavity.[127] Inelastic neutron scattering (INS) spectra were analyzed to extract the energies and intensities of the excitations. In contrast to water in C_{60},[136,137] the absence of transitions between the para and the ortho states implies the water was trapped in a way that the dipole is perpendicular to the c-axis.[45] Such planar confinement and the multi-well potential energy landscape are further supported by recent investigations on structurally related cordierite lattices. These studies revealed rich single-particle tunneling and collective dipolar excitations within the basal plane.[4] The beryl nano-cage thus provides planar confinement with intrinsic six-fold symmetry. A chain of planar rotors with a six-fold ($\mathbb{Z}_6$) on-site potential is therefore a promising framework to describe the tunneling dynamics of the confined water molecules.

Beryl can accommodate coplanar chains with a distance of $R = 9.2$ Å between the planar rotors.[3,45,123,124] The distance of 9.2 Å corresponds to nearest cages in *adjacent* channels, lying in a common plane perpendicular to the crystal c-axis. It is this in-plane arrangement that realizes the coplanar chain of Fig. 3.1.[3] Cages within a single channel are closer (4.6 Å). For that stacking direction, however, the water dipoles are perpendicular to the inter-rotor separation. In that case, antiparallel alignment is favored and is not described by the coplanar chain model considered here. The chain studied in this work is therefore an idealized subsystem of the full three-dimensional dipolar lattice of beryl. Using a value of $\mu = 1.85$ D for the dipole moment of water along with a rotational constant of $B = 3.04$ meV,[45] we obtain the following value for the interaction strength,

$$g = \frac{|\mu|^2}{B\ 4\pi\epsilon_0 R^3} = 0.90. \tag{3.15}$$

The value of the six-fold barrier itself is less settled, as the available estimates span

two orders of magnitude. Table 3.2 collects the values reported in the literature. The spread largely reflects the fact that the different techniques extract *different* quantities, all loosely referred to as *the barrier*. The INS tunneling analysis yields a static barrier between minima of the orientational potential of $\approx$ 176 meV. That quantity is lowered to 48–56 meV ($\approx$ 390–450 cm^{-1}, $\approx$ 560–650 K) when the coupling to cage vibrations is taken into account.[45] The lower and upper bounds of 56 and 176 meV used in a subsequent theoretical study[123] are not an independent measurement. They are obtained directly from that INS analysis where the upper bound is the static barrier and the lower bound is the vibration-lowered value. In that study the potential is written in a coupled two-level form rather than as a plain $\cos(6\phi)$ term. Conversely, the much smaller THz-derived value of 1.41 ± 0.05 meV (with ≈ 0.83 meV from DFT)[3] is the depth parameter of the six-well surface probed by the dipole-active transitions. This is a different quantity from the barrier through which the proton density tunnels. Broadband dielectric relaxation measurements[124] yield an Arrhenius activation energy for dipole reorientation of 16.4 ± 0.14 kJ/mol ($\approx$ 170 meV). Again, this is a kinetic rather than a static quantity. Its value is quite close to the static INS barrier.[45] Reconciling these observables within a single six-fold potential remains an open question.

Here, we adopt the INS-based barrier range of 48–56 meV.[45,123] The corresponding (reduced) dimensionless barrier is $A = A'/B \simeq 48/3.04$ to $56/3.04 \approx 16$–18. We can extract the critical coupling from the phase diagram shown in Fig. 3.6 at this barrier value. We obtain $g_c \simeq 0.4$. Since the physical coupling $g \approx 0.90$ exceeds g_c, this estimated value places coplanar chains of water in beryl in the ordered (ferroelectric) phase. We note that this conclusion is robust against the uncertainty in the barrier height. Even in the nearly-free-rotor limit suggested by the THz analysis ($A \approx 1.41/3.04 \approx 0.5$), the critical coupling is $g_c \approx 0.5$. The estimated $g \approx 0.90$ still exceeds that number. Barriers larger than the INS value only shift g_c to smaller values. For instance, $A \approx 176/3.04 \approx 58$ for the upper bound of Ref. 123, a value well within the range of Fig. 3.6. Coplanar water chains in beryl are therefore predicted to lie in the ordered phase for the entire reported range of barrier heights.

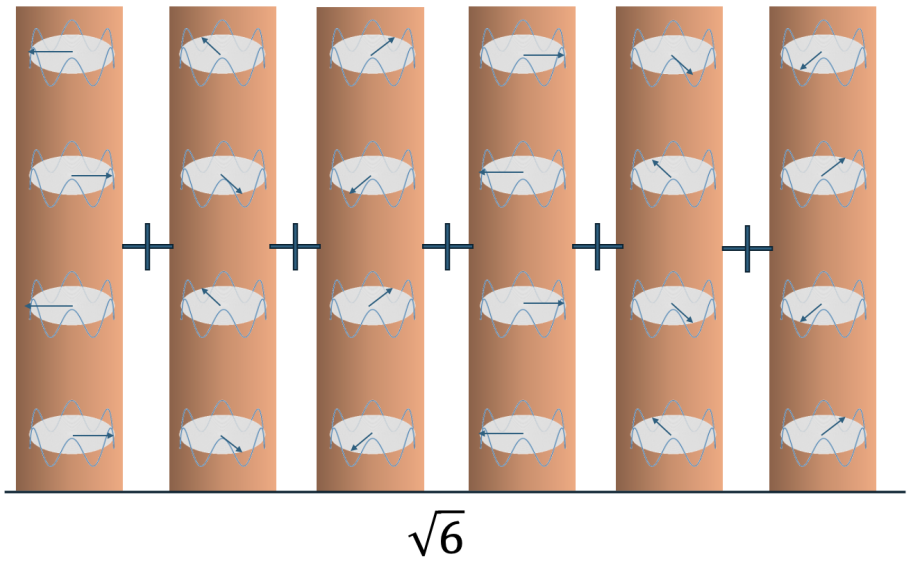
3.4 Concluding Remarks

We have studied the energetic, structural, and entanglement properties of a chain of hindered planar rotors with a six-fold potential of reduced barrier height A. The monomer energy levels were first computed for $A = 20$. The number of states below the barrier (n_{bb}) exhibits a regular staircase structure as a function of the reduced barrier height A. The rotor chain composed of these planar rotors undergoes a quantum phase transition from the disordered to the ordered phase as the dipolar coupling increases. The transition was characterized using the von Neumann entropy and the Binder cumulant. It reflects the competition between the dipolar interaction and the single-rotor kinetic energy. A clear trend emerges: as A increases, the von Neumann entropy of Fig. 3.4 reaches its plateau near $\ln 2$ at weaker interaction strength g. The Binder cumulant U_x, shown in Fig. 3.5, exhibits a similar trend. Indeed, U_x approaches its plateau of 2/3 at smaller g as A increases. Previous works using a number of these techniques suggest that the ground state of a dipolar planar rotor chain admits an ordered phase as well as a disordered phase.[99] Both phases can be accessed by tuning the dipolar coupling strength. Increasing the reduced barrier height from $A = 0$ to $A = 80$ lowers the critical coupling from $g_c \approx 0.5$ to substantially smaller values. A central result of this work is the collapse of the hindered-chain phase boundary onto the monomer tunneling splitting, $g_c \simeq \Delta(A)/2$. This relation is simple and physically transparent, and it should prove useful beyond the beryl application considered here. Our parameter estimates place a coplanar chain of water molecules in beryl in the ordered (ferroelectric) phase. Whether the idealized coplanar chains can be found in beryl samples remains an open question.

Experimentally, however, beryl shows only incipient ferroelectricity, with no long-range order down to sub-kelvin temperatures.[3,98] The absence of order may reflect partial cage occupancy or frustrating inter-chain couplings. The current results reveal a crossover behavior at finite N. Future work will include the required finite-size-scaling studies in order to obtain critical exponents. We also plan to perform finite-temperature path integral simulations for higher-dimensional lattices.[46,96,129]

Chapter 4

Orientational ordering of stacked chains of dipolar rotors in a hexagonal crystal field



We study the ground state of a chain of dipolar planar rotors stacked along the channel axis of a beryl-like host. Each rotor is hindered by a six-fold on-site potential. Because the

dipoles lie perpendicular to the line joining neighboring cages, the dipolar coupling reduces to a function of the difference of the two orientations alone. The total angular momentum is therefore conserved. The continuous U(1) symmetry of the chain is therefore broken not by the interaction, as in the coplanar geometry, but by the crystal field alone. What remains is the cyclic group $\mathbb{Z}_6$. The ordered phase is correspondingly six-fold degenerate and antiferroelectric. The entanglement entropy saturates at $\ln 6$ and the Binder ratio of the staggered polarization at 1/2. We first solve the two-rotor problem exactly. To study a ten-rotor chains, we use the density matrix renormalization group. We find that orientational order is strongly cooperative. Indeed, the longer chain reaches the ordered regime with a coupling that is around seven times smaller than in the case of 2 rotors.

4.1 Introduction

Molecules trapped in the nanometre-scale cavities of minerals such as beryl and cordierite realize interacting quantum rotors in an unusually clean setting.[1–4,6,45,97,98,123] The channels of beryl accommodate one water molecule per cage. The cages are far enough apart that the hydrogen bonding which dominates bulk water is largely suppressed.[7,45,124–127] What remains between neighboring guests is essentially the electrostatic dipole–dipole interaction. An array of pinned molecules can therefore develop electric order of its own.[3,11,128] Terahertz and dielectric measurements have reported precisely this predicted incipient ferroelectric behavior.[3,43,98]

Lattices of dipolar rotors reproduce this physics quantitatively. In one dimension, it possible to accurately predict the properties of systems of this kind.[9,33–35,38,39,46,99,138] The density matrix renormalization group (DMRG)[35,38,100,101] and path-integral techniques[57,96,106] have both been applied to these chains. For the unhindered chain, the dipolar coupling reduces the continuous U(1) symmetry of an isolated planar rotor to $\mathbb{Z}_2$. The ground state undergoes a transition belonging to the $(1+1)d$ Ising universality class.[35,51,99]

The beryl cage is not isotropic. It is hexagonal, and small enough that its walls confine the molecular dipole towards the six edges. This anisotropy is captured by a six-fold on-

site potential. The low-energy spectrum of a rotor place in this potential matches inelastic neutron scattering data.[1,3,4,45,123,124] In a companion study[139] we added such a term to a *coplanar* chain. In that geometry, the rotors are arranged along a line lying in their own plane of rotation. It was found that raising the barrier moves the critical coupling to smaller values. The rotor hindrance promotes orientational order rather than suppressing it.

Beryl is a three-dimensional crystal. A coplanar chain is only one of the one-dimensional cuts that can be taken through it. Our aim is to understand water in beryl one dimension at a time. The present work takes the orthogonal cut where rotors *stacked* along the channel axis. Each dipole i rotates in a plane perpendicular to the line joining it to its neighbors ($i \pm 1$). The change of geometry modifies the interaction qualitatively. In the coplanar arrangement, the separation vector lies in the plane of the dipoles. The dipolar tensor gives $\hat{y}_i\hat{y}_{i+1} - 2\hat{x}_i\hat{x}_{i+1}$. In the stacked arrangement, sketched in Fig. 4.1, every dipole is orthogonal to the separation vector. The terms involving $\boldsymbol{\mu} \cdot \hat{\boldsymbol{R}}$ vanish identically, and the coupling simplifies to the dot product $\boldsymbol{\mu}_i \cdot \boldsymbol{\mu}_{i+1}$. More precisely, the interaction becomes

$$\hat{V}_{i,i+1} \;\propto\; \hat{x}_i\hat{x}_{i+1} + \hat{y}_i\hat{y}_{i+1} \;=\; \cos(\phi_i - \phi_{i+1}). \tag{4.1}$$

The resulting symmetry is different. This is the central point of the present work. The coplanar interaction depends on the two angles separately and by itself breaks U(1) down to $\mathbb{Z}_2$. The transition studied previously is the spontaneous breaking of that $\mathbb{Z}_2$.[139] The stacked interaction of Eq. (4.1) depends only on the *difference* of the two angles. It is therefore invariant under a rigid rotation of the entire stack. The interaction therefore conserves the total angular momentum exactly. It does not break U(1) at all. In this geometry the symmetry breaking originates entirely in the crystal field. Because that field is six-fold, the remaining symmetry is not $\mathbb{Z}_2$ but rather the cyclic group $\mathbb{Z}_6$. The conserved quantum number is the total angular momentum modulo six. We are therefore in the presence of a broken U(1) rather than a broken $\mathbb{Z}_2$. A clock symmetry is obtained instead of an Ising one.[140,141]

The ordered state is now of different nature compared to the coplanar arrangement. The positive coupling of Eq. (4.1) is minimized when neighboring dipoles are antiparallel. The

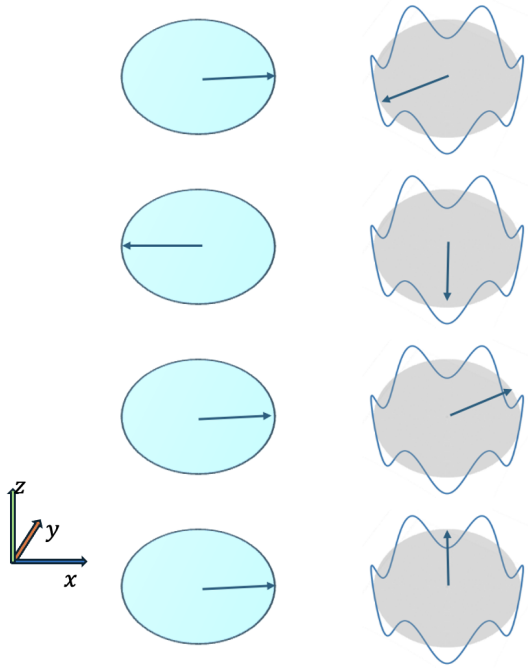


Figure 4.1: Schematic of the stacked chain, each panel showing one rotor of the stack viewed along the channel axis. The dipole of rotor i is the in-plane unit vector $(\hat{x}_i, \hat{y}_i) = (\cos\phi_i, \sin\phi_i)$, drawn as an arrow. Left: the free chain, in which the rotor may point in any direction and the dipolar coupling alone acts, leaving the continuous U(1) symmetry unbroken. Right: the same chain with the six-fold crystal field superimposed, whose six minima confine the dipole towards the edges of the hexagonal cage and reduce U(1) to $\mathbb{Z}_6$.

order along a stack is antiferroelectric rather than the head-to-tail ferroelectric arrangement of the coplanar chain. The ordered state is six-fold rather than two-fold degenerate. The saturation values of the usual diagnostics shift correspondingly. The bipartite entanglement entropy[132–134] goes to $\ln 6$ instead of $\ln 2$. The Binder ratio[35,130,131] of the staggered polarization approaches $1/2$ instead of the $2/3$ value of the coplanar arrangement.

That $\mathbb{Z}_6$ is abelian is useful in practice, because the corresponding quantum number can be conserved explicitly in a DMRG simulation. Deep in the ordered phase, the six states of the degenerate manifold are separated by splittings far below the resolution of the calculation. An unconstrained optimization becomes unreliable and can favor symmetry-broken solutions. The true finite-size ground state is totally symmetric and the use of quantum number conservation is a key aspect of the present work.

The remainder of this paper is organized as follows: Section 4.2 introduces the Hamiltonian of the stacked chain in reduced units and the residual $\mathbb{Z}_6$ symmetry is shown. Section 4.3 contains the ground-state results, based on exact diagonalization for a the $N = 2$ case. Chains of $N = 10$ rotors are studied using DMRG. Concluding remarks are presented in Sec. 4.4.

4.2 The model and its symmetry

4.2.1 System Hamiltonian

We treat a one-dimensional chain of N planar rotors coupled to their nearest neighbors. Each rotor is hindered by a six-fold on-site potential representing the anisotropy of the surrounding crystal. We write $\hat{L}_i = -i\,\partial_{\phi_i}$ for the angular momentum of rotor i in units of $\hbar$. The angle ϕ_i represents the orientation of the rotor. The eigenstate of $\hat{L}_i$ are,

$$\hat{L}_i\,|m_i\rangle = m_i\,|m_i\rangle\,. \tag{4.2}$$

The ladder operators that step between these states are,

$$\hat{E}_i^{\pm}\,|m_i\rangle = |m_i \pm 1\rangle\,. \tag{4.3}$$

The Hamiltonian is then defined as

$$H = \sum_{i=1}^{N} \left(B\,\hat{L}_i^2 - \frac{A'}{2}\big(\cos(6\phi_i) - 1\big) \right) + \frac{|\mu|^2}{4\pi\epsilon_0 R^3} \sum_{i=1}^{N-1} \hat{V}_{i,i+1}, \tag{4.4}$$

in which B is the rotational constant, A' the height of the six-fold barrier, μ the dipole moment of a single rotor and R the separation between neighbors. The above is the same Hamiltonian as the one introduced for the coplanar case.[139]

The two-body dipolar term now has the following form

$$\hat{V}_{i,i+1} = \hat{x}_i\hat{x}_{i+1} + \hat{y}_i\hat{y}_{i+1} = \cos(\phi_i - \phi_{i+1}), \tag{4.5}$$

where the constrained Cartesian operators of a rotor are $(\hat{x}_i, \hat{y}_i) = (\cos\phi_i, \sin\phi_i)$. Because the dipole interaction is of the dot product form, it is invariant under a rigid rotation of the whole chain. The total angular momentum is therefore conserved by this two-body term. This is the U(1)-symmetric interaction. The related coplanar chain has an unmodified dipole–dipole coupling of the form $\hat{y}_i\hat{y}_{i+1} - 2\hat{x}_i\hat{x}_{i+1}$.[139] It therefore has a lower symmetry.

Dividing Eq. (4.4) by B puts the problem in reduced units. Since the hindering potential acts on one rotor at a time it is absorbed into a monomer Hamiltonian,

$$\hat{h}_i^{1B} = -\frac{\partial^2}{\partial\phi_i^2} \underbrace{-\frac{A}{2}\big(\cos(6\phi_i) - 1\big)}_{\hat{V}_{6,i}}, \tag{4.6}$$

with $A = A'/B$ the reduced barrier height and $-\partial^2/\partial\phi_i^2 = \hat{L}_i^2$ by Eq. (4.2). Introducing the dimensionless coupling

$$g = \frac{|\mu|^2}{B\,4\pi\epsilon_0 R^3}, \tag{4.7}$$

the Hamiltonian becomes

$$\frac{\hat{H}}{B} = \sum_{i=1}^{N} \hat{h}_i^{1B} + g \sum_{i=1}^{N-1} \hat{V}_{i,i+1}. \tag{4.8}$$

No separate statement of the six-fold potential is needed, as it is carried entirely by $\hat{h}_i^{1B}$. Note that the constant in Eq. (4.6) fixes the zero of energy at the bottom of a well, and A is the full height of the barrier separating neighboring minima.

4.2.2 Momentum representation

The calculations are carried out in the momentum basis, in which the kinetic operator is diagonal,

$$\hat{L}_i^2 = \sum_{m=-\infty}^{\infty} m^2 \, |m\rangle \langle m| \,, \tag{4.9}$$

truncated symmetrically at $|m| \le l \equiv m_{\max}$. The ground state is obtained by the density-matrix renormalization group[101] in its matrix-product-state formulation.[100] For the chain of free rotors a cutoff of $l = 4$ is known to suffice; the six-fold potential changes the spectrum substantially, and the monomer convergence analysis reported separately leads us to adopt $l = 16$.

Both terms of Eq. (4.8) are conveniently written with the ladder operators of Eq. (4.3). Since $\hat{x}_i = (\hat{E}_i^+ + \hat{E}_i^-)/2$ and $\hat{y}_i = (\hat{E}_i^+ - \hat{E}_i^-)/2i$, the interaction reduces to a single pair of terms,

$$\hat{V}_{i,i+1} = \frac{1}{2}\left(\hat{E}_i^+ \hat{E}_{i+1}^- + \hat{E}_i^- \hat{E}_{i+1}^+\right), \tag{4.10}$$

one rotor gaining the unit of momentum that its neighbor loses. The products $\hat{E}_i^+ \hat{E}_{i+1}^+$ and $\hat{E}_i^- \hat{E}_{i+1}^-$, which would move the total momentum by two units, cancel identically between $\hat{x}_i\hat{x}_{i+1}$ and $\hat{y}_i\hat{y}_{i+1}$.

The hindering potential is diagonal in ϕ and becomes a sixth power of the same operators. Using $\cos 6\phi_i = ((\hat{E}_i^+)^6 + (\hat{E}_i^-)^6)/2$,

$$\hat{V}_{6,i} = -\frac{A}{4}\left((\hat{E}_i^+)^6 + (\hat{E}_i^-)^6 - 2\right), \tag{4.11}$$

so that the crystal field shifts the momentum of a single rotor by six units while the interaction exchanges one unit between neighbors. Matrix elements that would leave the retained range, $|m_i \pm 6| > l$ or $|m_i \pm 1| > l$, are discarded, which is the only effect of the truncation on these expressions.

4.2.3 Residual symmetry

Equation (4.10) makes the symmetry of the chain explicit. The interaction moves one unit of momentum from a rotor to its neighbor and so leaves the total $M = \sum_i m_i$ unchanged.

In the case of crystal field potential, Eq. (4.11) changes M by ± 6. The continuous U(1) symmetry of the coupling is therefore reduced by the crystal field to the cyclic group $\mathbb{Z}_6$. The conserved quantum number is

$$Q \;=\; \Big(\sum_i m_i\Big) \bmod 6. \tag{4.12}$$

Equivalently, $\cos 6\phi$ is invariant under a global rotation $\phi_i \to \phi_i + \alpha$ only for $\alpha = 2\pi n/6$.

Deep in the ordered phase the antiferromagnetic ground state is six-fold degenerate. The six states are related by the $\mathbb{Z}_6$ rotations. The symmetry-adapted combinations are their discrete Fourier transforms, labelled by $Q = 0, \ldots, 5$. The ground state is the totally symmetric combination and is the $Q = 0$ sector.

4.3 Results

We report ground-state properties of the stacked chain at reduced barrier heights $A = 20$, 40 and 60. Results are obtained with the momentum cutoff $l = 16$ established by the monomer convergence analysis. Two chain lengths are considered. The two-rotor problem is small enough to be solved exactly and is treated in Sec. 4.3.1. This $N = 2$ system serves both as a physical limit and as a reference against which the variational calculations can be assessed. Longer chains, for which exact diagonalization is intractable, are treated by DMRG in Sec. 4.3.2.

4.3.1 Two rotors: exact diagonalization

For $N = 2$ the Hilbert space is spanned by the product states $|m_1\rangle \otimes |m_2\rangle$ with $|m_i| \le l$. The total dimension is $(2l+1)^2 = 1089$ for $l = 16$. A problem of this size can be diagonalized explicitely. The Hamiltonian matrix is constructed in the product basis from Eqs. (4.10) and (4.11),

$$\frac{\hat{H}}{B} = \hat{h}_1^{1B} + \hat{h}_2^{1B} + \frac{g}{2}\left(\hat{E}_1^{+}\hat{E}_2^{-} + \hat{E}_1^{-}\hat{E}_2^{+}\right), \tag{4.13}$$

and is extremely sparse. The kinetic term is diagonal, the crystal field connects only m to $m \pm 6$, and the interaction only (m_1, m_2) to $(m_1 \pm 1, m_2 \mp 1)$. We therefore obtain the ground state by a Lanczos iteration rather than by full diagonalization. We seed each coupling with the converged eigenvector of the preceding one. The two routes agree to machine precision but the iterative one reduces the cost of a complete scan from tens of minutes to under a minute.

From the ground-state vector $\psi_{m_1 m_2}$ every quantity of interest can be obtained in closed form. The ground state eigenvector ψ can be viewed as a matrix indexed by m_1 and m_2. The singular value decomposition of that matrix is precisely the Schmidt decomposition across the single bond. The Schmidt values λ_n are the squared singular values and the entanglement entropy is $S_{vN} = -\sum_n \lambda_n \ln \lambda_n$. The Binder ratio is obtained from the staggered polarization $\hat{M}_x = -\hat{x}_1 + \hat{x}_2$ as $U_x = 1 - \langle \hat{M}_x^4 \rangle / 3 \langle \hat{M}_x^2 \rangle^2$.

As a first check, at $g \to 0$ the two rotors decouple and the ground-state energy must be twice the monomer value. The computed energies at $g = 0.01$ are 17.30985, 30.07253 and 39.83142 for $A = 20$, 40 and 60, which are indeed twice the corresponding single-rotor energies.

Table 4.1: Approach of the two-rotor ground state to the ordered limit. g_S and g_U are the couplings at which the entanglement entropy and the Binder ratio first come within 1% of $\ln 6$ and $1/2$. The last two columns give their values at the largest coupling computed, $g_{\max}$.

A	g_S	g_U	$g_{\max}$	$S_{vN}(g_{\max})$	$U_x(g_{\max})$
20	65.9	11.1	70.0	1.7821	0.49938
40	49.0	7.4	55.0	1.7799	0.49960
60	28.0	4.5	35.0	1.7804	0.49970

The approach to the ordered limit is shown in Fig. 4.2 and summarized in Table 4.1. Both diagnostics move towards the values expected of the six-fold symmetric state. The entanglement entropy tends towards $\ln 6$ and the Binder ratio towards $1/2$. Both do so at smaller coupling as the barrier is raised since the crystal field pre-localizes each rotor in

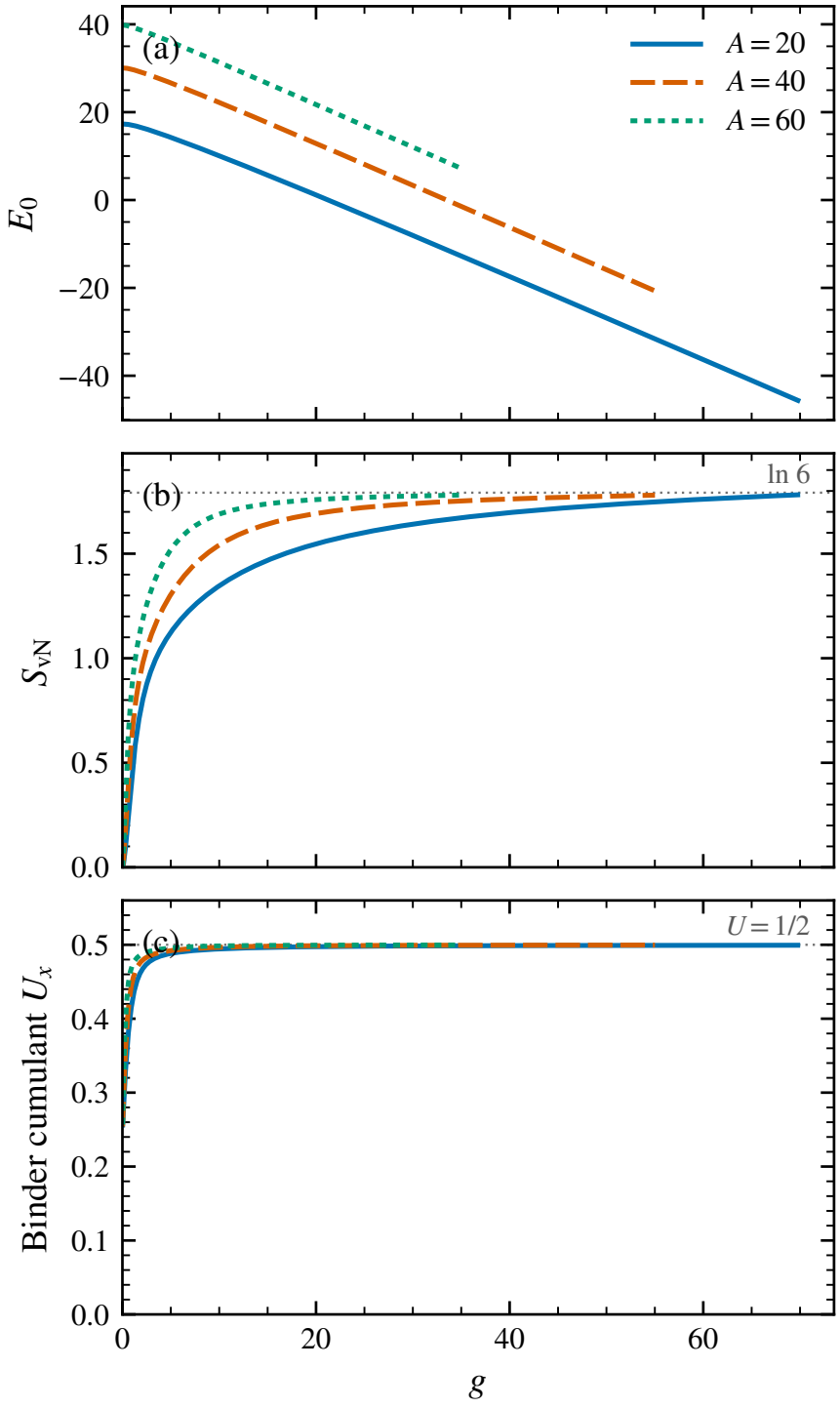


Figure 4.2: Exact results for two rotors at barrier heights $A = 20$, 40 and 60: (a) ground-state energy E_0, (b) entanglement entropy S_{vN} across the single bond, and (c) Binder ratio U_x of the staggered polarization, against the dipolar coupling g. Dashed lines indicate the ordered-phase values $\ln 6$ and $1/2$.

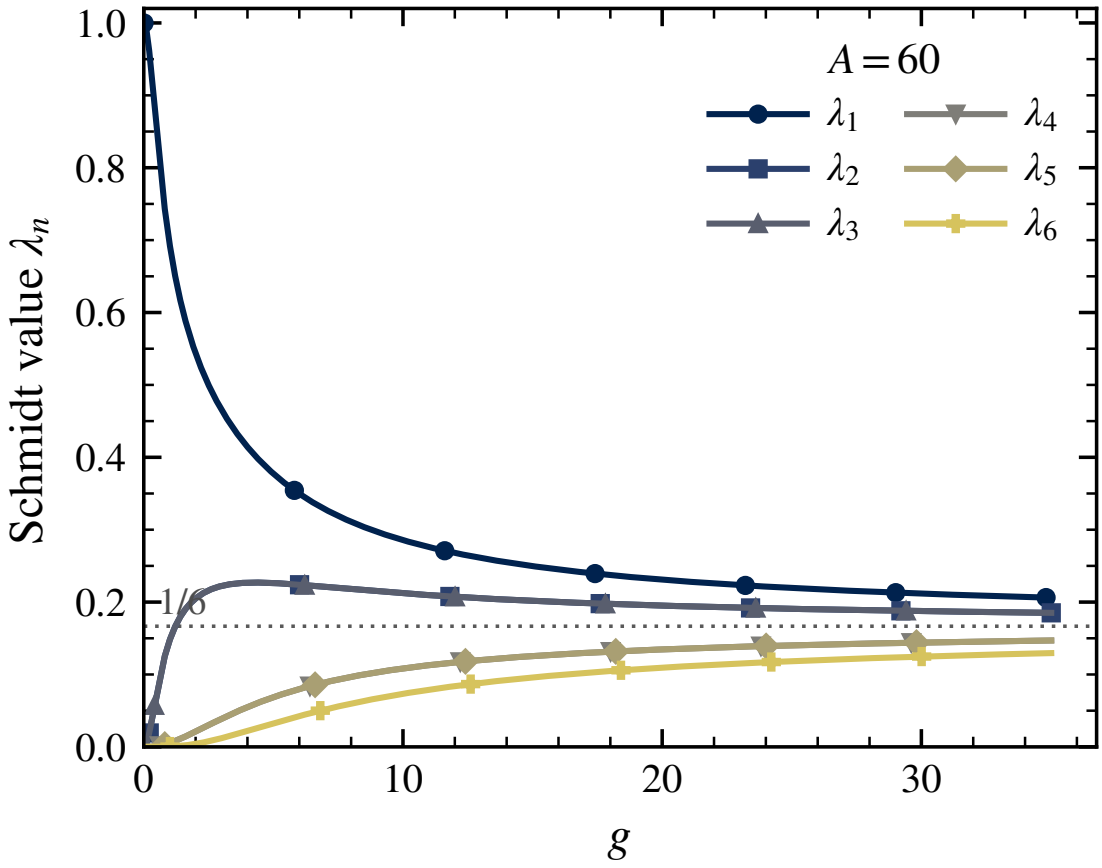


Figure 4.3: The six largest Schmidt values λ_n across the bond of the two-rotor chain at $A = 60$, against g. The dashed line marks 1/6. The weights approach a common value in the pattern 1–2–2–1 λ_2 and λ_3 coincide, as do λ_4 and λ_5, and the markers of each degenerate pair are offset along g so that both remain visible.

its wells. This means that less interaction is required to correlate them. This mirrors the trend found for the coplanar chain,[139] where raising the barrier lowers the critical coupling.

We observe that the Binder ratio is within 1% of 1/2 by $g \approx 11$, 7 and 5 for the three barriers. But the entanglement entropy requires couplings five to six times larger. The reason is that the Binder ratio depends only on the distribution of the order parameter. The latter becomes six-fold as soon as each rotor is localized. The entanglement entropy, however, also counts how sharply the six configurations are distinguished. This continues to improve well beyond that point where the Binder has settled.

The mechanism behind the entropy is visible in the entanglement spectrum, Fig. 4.3. At small g, a single Schmidt value carries all the probability and the two rotors are uncorrelated. As the coupling grows, five further weights rise and all six converge towards 1/6. This is what produces $S_{vN} \to \ln 6$ since the six equally weighted Schmidt states are the six orientations of the ordered pair.

One point should be noted about the entropy at very large coupling. S_{vN} does not approach $\ln 6$ from below and remain there. The entanglement entropy crosses $\ln 6$ and continues to rise, reaching 1.828 at $g = 100$ for $A = 20$ against $\ln 6 = 1.7918$.

The excess is not a truncation artifact, as calculations at $l = 24$ agree to 4×10^{-5}. Its origin is that the interaction locks only the relative angle of the two rotors. Once locked, each rotor within its well still has correlated fluctuations with the other rotor. That contribution is additional to the six-fold one. For two rotors sharing a single bond this excess is not negligible, and $\ln 6$ should be viewed as the value at which the six-fold structure is complete rather than as a strict upper bound. This is a finite size effect.

4.3.2 Longer chains: DMRG

For chains beyond a few rotors the Hilbert space grows as $(2l+1)^N$ and exact diagonalization is no longer possible. We therefore turn to DMRG. The $\mathbb{Z}_6$ symmetry is imposed directly on the tensors, using the quantum-number conserving block-sparse machinery of the ITensor library.[121,142] Each momentum state $|m\rangle$ is labelled by m mod 6, the simulation is started in the sector $Q = 0$, and the optimization is confined to that sector throughout.

This requires the interaction to be written in the ladder form of Eq. (4.10) where one rotor gains a unit of angular momentum its neighbor loses. With a product of dipole operators, neither conserves Q on its own. The calculations use a two-site algorithm with an SVD threshold of 10^{-7}, a relative energy convergence criterion of 10^{-7}, and a maximum bond dimension of 200. That bond dimension is never reached in our calculations. The largest bond dimension observed is well below that ceiling and the entanglement saturates at $\ln 6$. The entropy and Schmidt weights are taken at the central bond.

Figure 4.4 shows the same three quantities as for two rotors, and Table 4.2 contains the couplings at which each reaches its ordered-phase value. The qualitative behavior is the same as both diagnostics approach $\ln 6$ and $1/2$. They do so at smaller coupling as the barrier is raised. The entanglement spectrum, Fig. 4.5, again shows six weights merging on $1/6$ with the 1–2–2–1 degeneracy of the $\mathbb{Z}_6$ irreducible representations. At the largest coupling, the six weights are 0.174, 0.170, 0.170, 0.163, 0.163, 0.159 for $A = 60$. They are similar for $A = 40$.

Table 4.2: Couplings at which the entanglement entropy and the Binder ratio of the ten-rotor chain first come within 1% of $\ln 6$ and $1/2$, with their values at the largest coupling computed. The corresponding two-rotor couplings from Table 4.1 are repeated for comparison.

	$N = 10$				$N = 2$	
A	g_S	g_U	$S_{vN}(g_{\max})$	$U_x(g_{\max})$	g_S	g_U
20	9.3	8.5	1.8015	0.4977	65.9	11.1
40	4.5	4.5	1.7953	0.4987	49.0	7.4
60	2.4	2.5	1.7943	0.4985	28.0	4.5

Compared to the two-rotor problem, the ten-rotor chain reaches the ordered limit at a coupling roughly seven times smaller, g_S falling from 65.9 to 9.3 at $A = 20$ and from 28.0 to 2.4 at $A = 60$. Each interior rotor is held by two neighbors rather than one, and the alignment propagates along the chain. This means that far less coupling is needed to establish the six-fold ordered manifold. Orientational order in these systems is thus strongly cooperative. The two-rotor problem substantially overestimates the coupling at

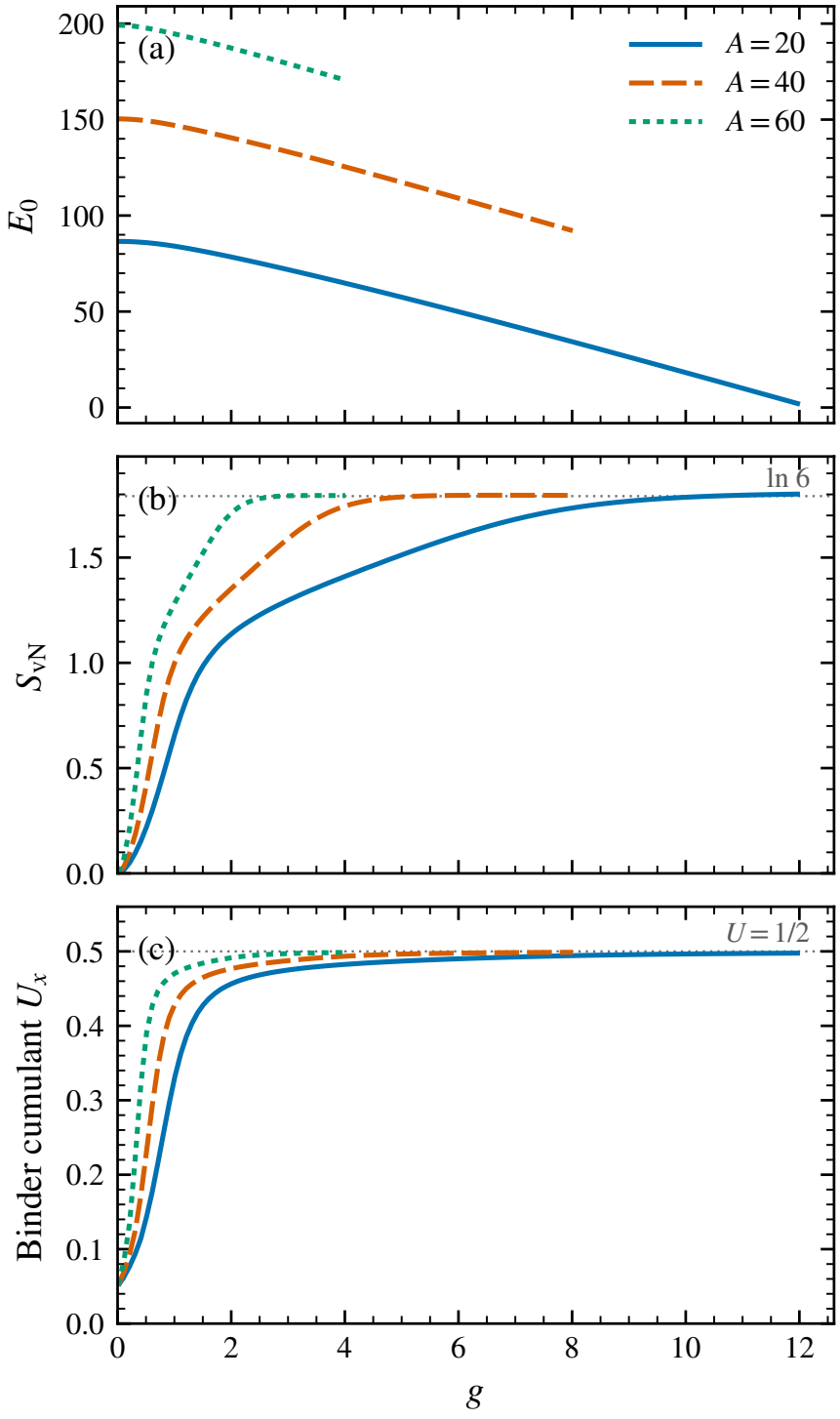


Figure 4.4: Ground-state energy E_0, entanglement entropy S_{vN} at the central bond, and Binder ratio U_x of the staggered polarization, against the dipolar coupling g for $A = 20$, 40 and 60 at $N = 10$. Dashed lines mark $\ln 6$ and $1/2$.

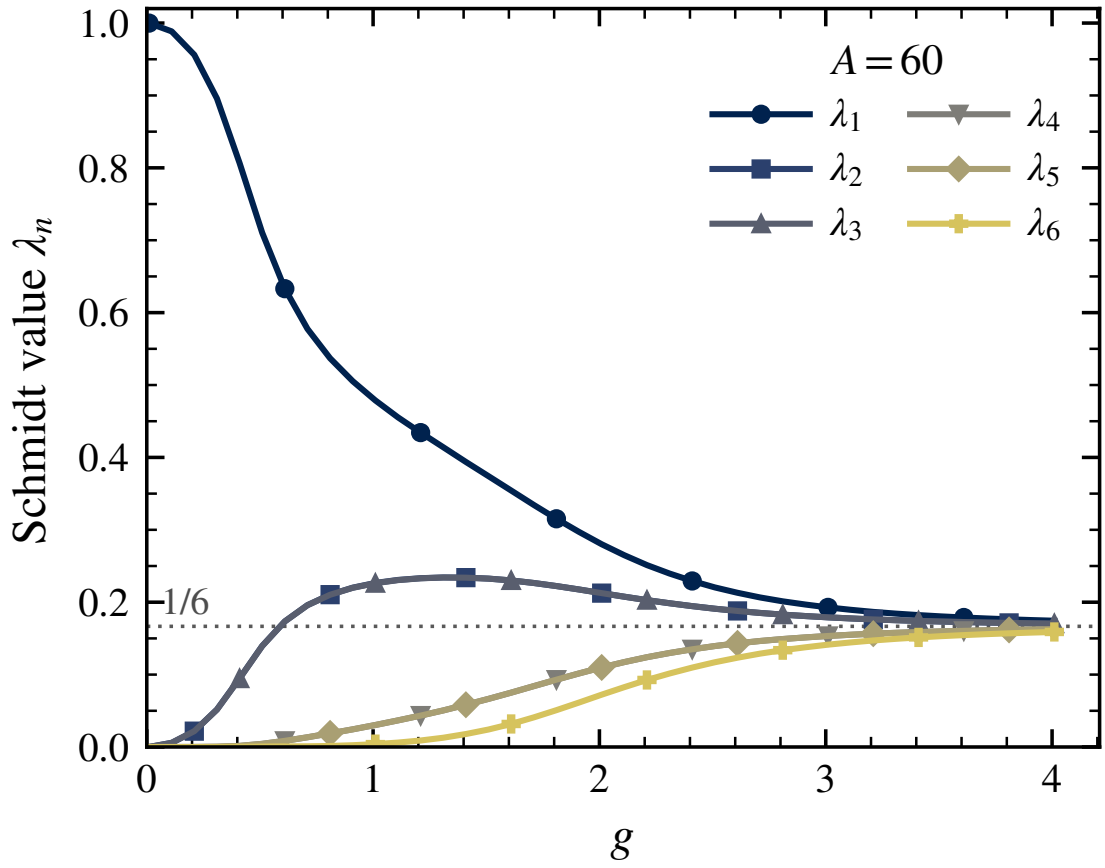


Figure 4.5: The six largest Schmidt values at the central bond against g, for $A = 60$ at $N = 10$. The dashed line marks 1/6. As in the two-rotor case, the weights approach a common value in the pattern 1–2–2–1.

which it sets in because no site has 2 neighbors.

For two rotors the entanglement entropy lagged far behind the Binder ratio, requiring five to six times the coupling. For ten rotors, the two nearly coincide, with g_S and g_U agreeing to within the grid spacing at $A = 40$ and 60. With a single bond, the entropy must resolve the six configurations sharply before it saturates, whereas at the central bond of a longer chain the six-fold structure of the ordered manifold is already reflected in the reduced density matrix as soon as the chain orders. The entanglement entropy is therefore a much more direct probe of the ordering transition in the longer chain than the two-rotor results alone would suggest.

The exact two-rotor results of Sec. 4.3.1 also provide a check on the DMRG itself. Comparing the two for $N = 2$ over the couplings computed, the energies agree to 10^{-6} away from the first point of the scan, which is seeded by the non-interacting warm-up rather than by its neighbor and is the least converged point of any run. The entanglement entropy agrees less closely, differing by up to 3×10^{-3} near the crossover. This ordering is expected as the energy is variational and therefore second order in the error of the state. The entropy on the other hand is first order. This makes it the more sensitive diagnostic of convergence of a DMRG calculation.

4.3.3 Connection to beryl parameters

The geometry of the stacked chain yields a different rotor-rotor distance compared to the coplanar case. The nano-channels of beryl is aligned along the crystallographic c axis and are arranged hexagonally with a separation of 9.2 Å between neighboring channels.[45,123,124] Within a single channel the cages that host the water molecules are stacked at intervals of 4.6 Å. This corresponds to half the lattice constant c, as shown in Fig. 1a of Gorshunov and coworkers.[3] The two geometries therefore sample different distances. The difference is a simple factor of 2,

$$R_{\text{stacked}} = \tfrac{1}{2} R_{\text{coplanar}}, \qquad 4.6\ \text{Å} = \tfrac{1}{2}\left(9.2\ \text{Å}\right). \tag{4.14}$$

Using the dipole moment of water $\mu = 1.85$ D and the rotational constant $B = 3.04$ meV,[45]

the dimensionless coupling of Eq. (4.7) becomes

$$g = \frac{|\mu|^2}{B\, 4\pi\epsilon_0 R^3} = 7.2 \tag{4.15}$$

for the stacked chain. That number was $g = 0.90$ for the coplanar chain with the same μ and B.[139] Since g scales as R^{-3} and Eq. (4.14) halves R exactly, the stacked coupling is larger by exactly a factor of $2^3 = 8$. The same crystal, the same molecule and the same rotational constant therefore yield couplings an order of magnitude apart depending on the choice of chain axis. Water in beryl is far more strongly coupled along a channel than between channels. This is what makes the stacked direction the one that favors order the most.

Table 4.3: Critical coupling g_c of the stacked chain at $N = 10$, taken from the steepest gradient of the Binder ratio. Comparison is made with the coupling $g = 7.2$ estimated for water in beryl.

A	g_c	g/g_c
20	0.81	8.9
40	0.51	14
60	0.31	23

To place this on the phase diagram we extract the critical coupling from the steepest gradient of the Binder ratio, as was done for the coplanar chain.[139] The resulting values, Table 4.3, are $g_c = 0.81$, 0.51 and 0.31 for $A = 20$, 40 and 60, and follow the same trend. A higher barrier moves the transition to weaker coupling.

A barrier that corresponds to actual beryl can be obtained from the inelastic neutron scattering estimate of 48–56 meV for the six-fold barrier.[45] In reduced units, the value is $A = A'/B \simeq 16$–18. This lies just below the smallest barrier computed here where $g_c = 0.81$. The critical coupling at $A \approx 17$ is therefore of order unity. The estimated physical coupling $g \approx 7.2$ exceeds it by nearly an order of magnitude. The stacked water chains in beryl are well inside the ordered phase based on this prediction. This conclusion is not sensitive to the considerable uncertainty in the barrier height. Indeed, raising A only lowers g_c further, and even in the nearly free-rotor limit suggested by the terahertz

analysis, the critical coupling remains of order one half. This value is still an order of magnitude below 7.2.

Two limitations of this estimate should be stated. The couplings in Table 4.3 are obtained at $N = 10$ and are therefore crossover values rather than critical points of the thermodynamic limit. The results of Sec. 4.3.2 show that the onset of order moves to smaller coupling as the chain lengthens. We also treat the stacked chain as isolated while in the crystal, each channel is surrounded by others at 9.2 Å. The inter-channel coupling is eight times weaker but not zero. We can view our simulated system as partially water-filled beryl crystal.

4.4 Concluding Remarks

We have studied the ground state of a chain of dipolar planar rotors stacked along the channel axis of a beryl-like host. Each rotor is hindered by a six-fold on-site potential of reduced barrier height A. Stacking places every dipole perpendicular to the line joining neighboring cages. The dipolar coupling therefore reduces to a function of the difference of the two orientations alone. The total angular momentum is therefore conserved exactly by the dipolar interactions. The continuous U(1) symmetry of the chain is broken by the crystal field alone rather than by the interaction. The remaining symmetry is $\mathbb{Z}_6$ instead of the $\mathbb{Z}_2$ of the coplanar geometry. The ordered phase has six-fold degeneracy and is antiferroelectric rather than head-to-tail ferroelectric.

The two-rotor problem was solved exactly by direct diagonalization in the momentum basis. For $N = 10$ chains, we used DMRG with the $\mathbb{Z}_6$ quantum number conserved explicitly. Both give the same picture of the approach to the ordered regime. The von Neumann entropy rises towards $\ln 6$ and the Binder ratio of the staggered polarization towards 1/2. We observed that the six largest Schmidt values merge on 1/6 in the 1–2–2–1 pattern. Raising the barrier from $A = 20$ to $A = 60$ moves the onset of order to smaller coupling. The same trend was reported for the coplanar chain[139] where the crystal field pre-localizes each rotor in its wells. Less interaction is therefore required to correlate neighbors. This reinforces the conclusion that hindrance promotes orientational

order rather than suppressing it.

Comparing the two chain lengths shows the ordering to be strongly cooperative. Ten rotors reach the ordered regime at roughly seven times smaller coupling than two, the entropy criterion falling from $g \approx 66$ to $g \approx 9$ at $A = 20$ and from $g \approx 28$ to $g \approx 2.4$ at $A = 60$. The relationship between the two diagnostics also changes with length: for two rotors the entanglement entropy lags the Binder ratio by a factor of five to six, whereas for ten they coincide to within the grid spacing, so the entropy is a much more direct probe of the ordering in the longer chain. A two-rotor calculation, though exactly solvable, therefore substantially overestimates the coupling at which order sets in.

Applying the model to beryl itself, the cages along a channel are stacked 4.6 Å apart, half the 9.2 Å separating neighboring channels, so the coupling along a stack is larger by a factor of eight: $g \approx 7.2$ against 0.90 for the coplanar chain. Taking the critical coupling from the steepest gradient of the Binder ratio gives $g_c = 0.81$, 0.51 and 0.31 at $A = 20$, 40 and 60, and the barrier inferred from neutron scattering corresponds to $A \approx 16$–18. The physical coupling therefore exceeds the critical one by roughly an order of magnitude, placing stacked water chains in beryl well inside the ordered phase, and considerably more decisively than in the coplanar geometry.

Future work will involve the simulation of longer chains and a finite-size scaling analysis to locate the critical coupling and establish the universality class. For a $\mathbb{Z}_6$ clock symmetry, the Ising class found in the coplanar case remains to be confirmed.[135,140,141] There is the possibility of an intermediate critical phase observed for clock models with more than four states. Answering this question is a natural extension for this geometry. Taken together with the coplanar chain, the stacked geometry treated here provides the second of the one-dimensional cuts through the beryl lattice. Combining the two is a promising route towards the full three-dimensional problem of water confined in beryl.

Chapter 5

Conclusions

The goal of this thesis is to develop and test methods for chains of confined rotors and learn their limits. We also adapted DMRG for coplanar and stacked rotor chains to observe the nature of the symmetry breaking. Earlier PIGS work used continuous angles with MH sampling.[39–41] A main contribution of this thesis is the replacement of MH sampling with rejection-free Gibbs sampling, which is particularly effective in the region of the phase transition. We systematically studied the properties of planar rotor chains and investigated the critical behavior of water in both the presence and absence of a six-fold potential, using a newly developed PIMC-DVR method designed for the system. A comprehensive set of results shows that a higher potential barrier leads to a higher ground state energy and an earlier phase transition.

Because electronic behavior depends critically on nuclear configuration, contemporary ab initio simulations integrate DFT to determine electronic properties. As a robust computational strategy, MD is uniquely equipped to investigate both the spatial trajectories and statistical mechanics of confined molecular systems, including CNT. The scaling and improvement of MD methodologies have progressed rapidly with high-performance computing (HPC) and parallelized software frameworks. This provides favorable conditions for our research. When classical mechanics fails to describe microscopic systems adequately, a quantum-mechanical treatment becomes essential. In systems containing light nuclei, these deviations often manifest as pronounced nuclear quantum effects, such as zero-point mo-

tion and tunneling. At low temperatures, within the Hilbert-space formulation of quantum mechanics, the properties of a system are largely governed by its ground state and low-lying excitations, making an accurate description of the ground-state manifold particularly important. With the aid of high-throughput computations, one can efficiently sample energies over a wide range of atomic configurations and thereby construct the corresponding potential energy surfaces, providing a robust foundation for materials science.

In Chapter 2, we introduced a path integral Monte Carlo simulation framework which was established by implementing a discrete variable representation. This algorithm improves sampling efficiency by generating conditional probability tables, thereby shortening the Markov chain autocorrelation time. The ground state energy results at imaginary time for a few rotors (N=2 and N=3) were shown to converge, after extrapolation, against exact ED and Numerical Matrix Multiplication (NMM) results. The maximum discretized angular momentum basis $m_{max} = 5$ (L=11 grid points) is shown to be sufficient for the convergence. In this case, DVR is seen to have a sign problem due to the positive off-diagonal entries of the Hamiltonian in the position basis for small time steps ($\tau < 0.2$). A bigger m_{max} pushes this limit down. Then the approach was extended to a longer chain with N=100 rotors. The PIMC ground state energy at $N = 100$ was found to be in good agreement with the DMRG benchmark. However, further study of the correlation function with PIMC was hindered by critical slowing down near the transition. Gibbs sampling, on the contrary, shortens the autocorrelation time. The key is that Gibbs sampling can systematically update all degrees of freedom owing to its rejection-free character, in contrast to the MH algorithm.

In Chapter 3, we focus on simulating the energy and entropy of a partial beryl system, where a single cavity is simplified using a planar rotor model under a six-fold potential (V_6). We first evaluated the monomer energy levels for a potential barrier of $A = 20$, which established the required basis convergence ($m_{max} = 16$). The chain was then treated with DMRG for a system of $N = 50$ rotors. This is a completely new attempt to solve the six-fold crystal field for a coplanar rotor chain with DMRG. Statistical analysis of the number of states below the barrier (n_{bb}) reveals a regular staircase structure as a function of the magnitude of V_6. Furthermore, a rotor chain composed of these planar rotors can undergo a quantum phase transition from a disordered to an ordered phase as g increases. According

to the scaling law, $g_c(A) \approx 0.49\Delta(A)$, and the coplanar chain in beryl displays an ordered phase with $g \approx 0.9$, which is far larger than the critical point. By studying longer chains and conducting finite-size scaling analysis, it should be possible in the future to pinpoint the critical coupling more accurately and clarify its universality class. For systems with $\mathbb{Z}_6$ clock symmetry, their universal behavior may not necessarily belong to the Ising class observed in coplanar systems; furthermore, whether this geometric structure also supports the intermediate critical phase commonly observed in clock models with more than four states is another natural and important question. In addition to ground-state properties, finite-temperature path integral simulations, quantum bit mappings of rotor chains, and predictions of observables from inelastic neutron scattering will all help to establish a more direct correspondence between the results of this study and experimental observations. Experiments, however, observe only incipient ferroelectricity. We speculate this may be due to partial occupation of the cages or to inter-chain coupling.

In Chapter 4, we studied the features of the stacked rotor chain in terms of ground state energy, Schmidt values and the Binder ratio. We obtained exact results at $N = 2$ and benchmarked $N = 10$ with DMRG (the N=10 values are cross-over values, not the true critical points). As in the coplanar chain, the critical coupling of the stacked chain also decreases with the barrier height. For the interaction strength in the stacked chain in beryl, $g \approx 7.2$ is eight times the coplanar strength, with single cages 4.6 apart. The 10-rotor chain orders at about 7 times smaller coupling (g_S: 65.9→9.3 at A=20). While the underlying interaction preserves the continuous $\mathbb{U}(1)$ symmetry, the presence of a crystal field explicitly reduces this to the discrete $\mathbb{Z}_6$ subgroup; furthermore, at sufficiently large coupling g, the dipolar interaction breaks the residual $\mathbb{Z}_6$ symmetry, ultimately driving the system into an antiferroelectric ordered state. The Binder ratio U_x, computed from the staggered polarization as a function of the dipolar coupling g, goes to 1/2 for stacked rotors, not 2/3. The von Neumann entropy S_{vN} as a function of g goes to $\ln 6$. The relationship between these two methods of diagnosis also differs with length: for $N = 2$, the entanglement entropy saturates at a coupling 5-6 times larger than the Binder ratio; while for $N = 10$, the two measures overlap within the g-scan grid spacing range; therefore, entropy is a more straightforward indicator of order in longer chains. Furthermore, whether this geometry supports the intermediate critical phase seen in clock models with more than four states

is also a natural question. Combined with the results for coplanar chains, the stacked geometric structure discussed in this thesis can be viewed as a second one-dimensional cross-section through the beryl lattice; considering both together represents a natural path toward a complete three-dimensional study of the "water trapped in beryl" problem. An identical barrier trend emerges across both configurations, while geometry serves as the primary determinant of the symmetry and order type of the system. The geometric layout dictates the coupling strength (yielding 0.9 in the coplanar arrangement and 7.2 in the stacked configuration). Both one-dimensional cuts point toward a robust ordered phase in beryl.

5.1 Future Work

In this section, we discuss various future research directions for the further study of planar rotors. Chapters 2–4 span the research from the rotation of a water monomer to two typical rotor chains - coplanar and stacked. However, this research still has limitations. The scope of the study is limited to partial structures of beryl with finite values of N. In Chapter 2, we studied 2, 3, up to 100 rotors. In Chapter 3 we studied 50 rotors, and in Chapter 4 we studied 2 and 10 rotors. They are sufficient to observe a cross-over behavior, but a single system size is not enough to study criticality for a phase transition. Furthermore, the actual study of bulk beryl remains to be solved in future work. For 3-dimensional simulation (bulk beryl for example), the PIMC algorithm needs further development to handle the computational cost growth during the simulation.[46,129,143,144] The methodology corresponding to finite temperature is also an important question for future study.

5.1.1 Finite-size scaling

The transition point itself is characterized by diverging correlation lengths which cause the many-body physics to become invariant under scale transformations. This allows one to construct a macroscopic theory (via the so-called renormalization group flow) to describe the statistical mechanics of critical systems near the continuous phase transitions. The

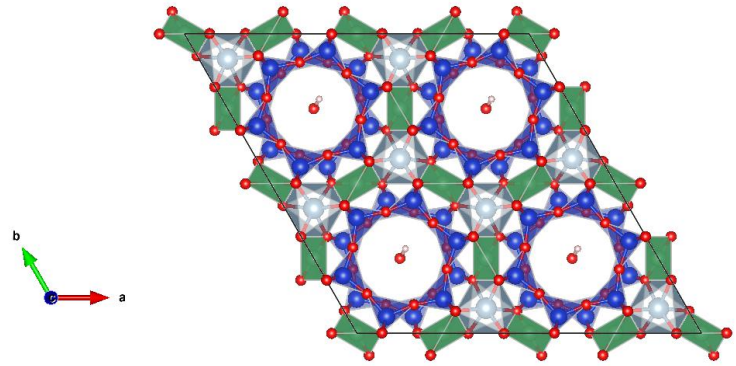


Figure 5.1: Periodically arranged water molecules in beryl of cross-section perpendicular to the cavity channel.

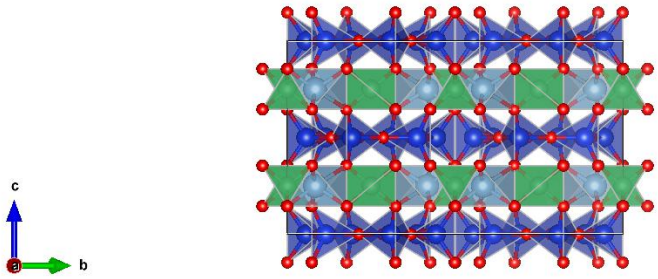


Figure 5.2: Periodically arranged water molecules in beryl of cross-section horizontal to the cavity channel.

resulting effective field theories abstract away the microscopic details of the systems they model and classify the large-scale behavior of a wide array of strikingly different Hamiltonians into a handful of universality classes. A powerful example is the 3D XY universality class, which can describe both the continuous superfluid phase transition of helium-4 and the superconductor-insulator phase transition in the fermion Hubbard model. Towards the latter objective, various computational techniques have been developed over the past five decades to circumvent the exponential scaling of exact matrix diagonalization with system size, such as the DMRG, coupled cluster approaches and PIMC methods. Since path integral techniques suffer from a slowdown in convergence near continuous phase transitions while scaling polynomially with lattice dimensions, this system provides an excellent testing ground for optimizing QMC techniques targeting molecular rotations restricted to a plane. The phase diagram of this system has been investigated in the past both computationally as well as theoretically using renormalization group analysis due to its rich structure. Depending on the order of discretization (d) and the existence of a chiral symmetry breaking term, the model admits either 2 or 3 distinct phases. For large d, a gapless phase exists between the two gapped phases: one that preserves the $\mathbb{Z}_d$ symmetry and another that breaks it. For small d, the phase diagram contains only the two gapped phases, with a continuous phase transition separating them. Our future finite-size-scaling study will determine which scenario applies to our chains. This is interesting because the universality class of the transition in the quantum clock model depends on d. It is this need to optimize our simulation techniques for planar rotor lattices that motivated the work contained in this thesis.

5.1.2 Finite-temperature simulations

The ground state under finite-temperature simulation can be determined by inspection. The potential energy is minimized by any linear combination of the states $|\psi = (0, \cdots, 0)\rangle$ and $|\psi = (\pi, \cdots, \pi)\rangle$. Therefore, the ground state is two-fold degenerate and the $\mathbb{Z}_2$ symmetry preserving state is given by:

$$|\psi\rangle = \frac{1}{\sqrt{2}}(|\psi = (0, \cdots, 0)\rangle + |\psi = (\pi, \cdots, \pi)\rangle) \tag{5.1}$$

In the absence of perturbations, the exact ground state is specified by the above equation. The full Hamiltonian is given by:

$$H = \sum_{i=1}^{N} B\hat{L}_i^2 + g\sum_{i=1}^{N-1}\hat{V}_{i,i+1} - h\sum_{i=1}^{N}\cos(\phi_i) \tag{5.2}$$

The symmetry is spontaneously broken in the thermodynamic limit ($N \to \infty$) due to external perturbations, which yields a non-zero net polarization. We can apply a small external field as a mathematical device ($|h| \ll 1$) to make it visible.

$$H' = \sum_{i=1}^{N-1}(\sin(\phi_i)\sin(\phi_{i+1}) - 2\cos(\phi_i)\cos(\phi_{i+1})) - h\sum_{i=1}^{N}\cos(\phi_i) \tag{5.3}$$

The calculation of the expectation value of the polarization in these cases yields the following:

$$\langle M\rangle_{h>0} = \frac{1}{N}\sum_{i=1}^{N}\cos(0) = 1, \quad \langle M\rangle_{h<0} = \frac{1}{N}\sum_{i=1}^{N}\cos(\pi) = -1 \tag{5.4}$$

The symmetry broken ground states that result as a consequence of the external perturbation have less symmetry than the Hamiltonian. This yields a non-zero polarization for large interaction strength g. On the contrary, for the symmetry preserving state in the two-fold degenerate ground state, the polarization is identically zero. In theoretical models, this spontaneous symmetry breaking presents as an order of limits phenomenon. One way to see this is by analyzing the relative probability of the system being in a positive polarization ($\langle M\rangle = 1$) in the presence of an external perturbation. To this end, let us first introduce a finite temperature canonical ensemble to compute the required probabilities (similar to our construction of the imaginary-time path integral in an earlier Chapter). In order to compute the relative probability in future work, we first consider canonical ensemble probabilities:

$$P(M=-1) = \frac{1}{Z}e^{-\beta H'} = \frac{1}{Z}e^{-\beta hN}$$
$$P(M=1) = \frac{1}{Z}e^{-\beta H'} = \frac{1}{Z}e^{\beta hN}$$

The expectation value operator $\langle\cdot\rangle$ for M has been suppressed in the above equations. Note that $\langle M\rangle = 1$ implies $\phi = (0, \cdots, 0)$ and $\langle M\rangle = -1$ implies $\phi = (\pi, \cdots, \pi)$. Since

$H_0'[(0,\cdots,0)] = H_0'[(\pi,\cdots,\pi)]$, the relative probability only depends on the perturbation term and is given by:

$$P = \frac{P(M=-1)}{P(M=1)} = \frac{e^{-\beta h N}}{e^{\beta h N}} = e^{-2\beta h N} \tag{5.5}$$

In future analysis, the first thing that needs to be considered is taking the thermodynamic limit ($N \to \infty$), after which the $h \to 0$ limit is adopted; spontaneous symmetry breaking manifests only in this order of limits. Under this limit, the symmetry preserving ground state is an unstable fixed point. Consequently, for a system in the thermodynamic limit, whether increasing g drives the ground state from a disordered (symmetry preserving) state to an ordered (symmetry breaking) state, as we predicted in earlier chapters, needs to be confirmed. It is the crossover between these two regimes that yields the (1+1)d Ising universality class phase transition for this system. It is instructive to note that the above non-rigorous analysis, provided to motivate the existence of a continuous phase transition, can be formalized using DMRG calculations.

5.1.3 Extension toward a three-dimensional beryl model

In these confined molecular systems, at low temperatures, the vibrational degrees of freedom of each molecule are restricted to their respective ground states. The orientational statistical mechanics of the many-body lattice is mostly determined by the rotational degrees of freedom of pinned molecules. Such effective Hamiltonians govern the properties of crystals such as beryl and cordierite. The recent DMRG studies pertaining to 1d lattices of planar rotors interacting with a nearest neighbor dipole-dipole coupling have shown that the system admits a quantum phase transition when the interaction strength between the rotors is approximately 0.5. PIMC techniques have been used to study rotational motion because a pair-product approximation for the angular coordinates in the propagation scheme inherently accounts for all two-body correlations exactly. Moreover, these techniques have successfully been used for chains of planar rotors with a minimal computational cost. This method can be easily extended to higher dimensional lattices, enabling the study of the ground state properties of real crystals such as beryl. This system has been shown to exhibit ferroelectric behavior in experiments. The pure chains studied here are unlikely in the real crystal, but they are the right starting point. The actual study of

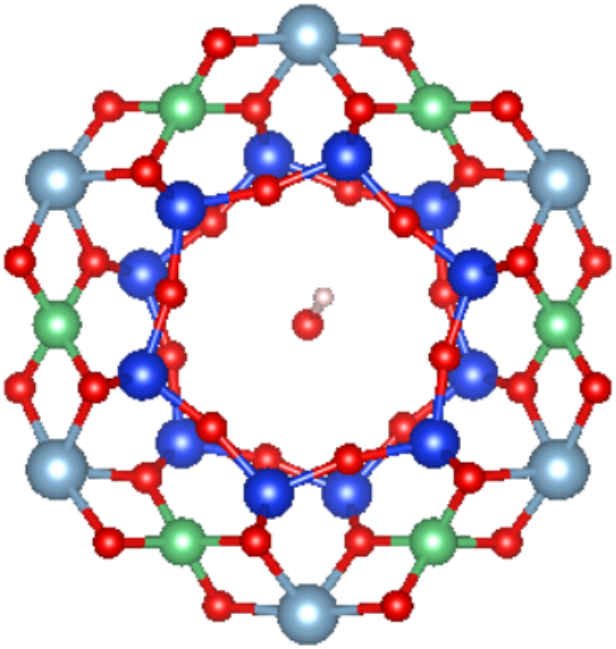


Figure 5.3: Schematic diagram of hexagonal beryl crystal cavity shows a cross-section along the channel direction.

beryl belongs in future work. The limitation of DMRG is that it is only feasible for 1D chains due to the area law. The only methods that can probably be deployed in three-dimensional (3D) are PIGS and PIMC. Another promising future direction would be to explore the phase diagram of such systems as a function of temperature as well as the interaction strength using Monte Carlo (MC) simulations. Since this would require simulating a large number of rotors for a range of different parameters, the pair approximation with Gibbs sampling would be a promising candidate for calculating ground state properties efficiently. As our next step, DFT calculations will be performed with the CP2K package.[145] CP2K is an atomistic simulation package with powerful features for simulating solid-state, liquid, molecular, periodic, crystalline and biological systems. Preliminary results from the calculation with CP2K show a doublet-of-triplets structure in the localized monomer potential.

Figure 5.3 shows a model of the rotation of a water monomer in a single cavity of beryl

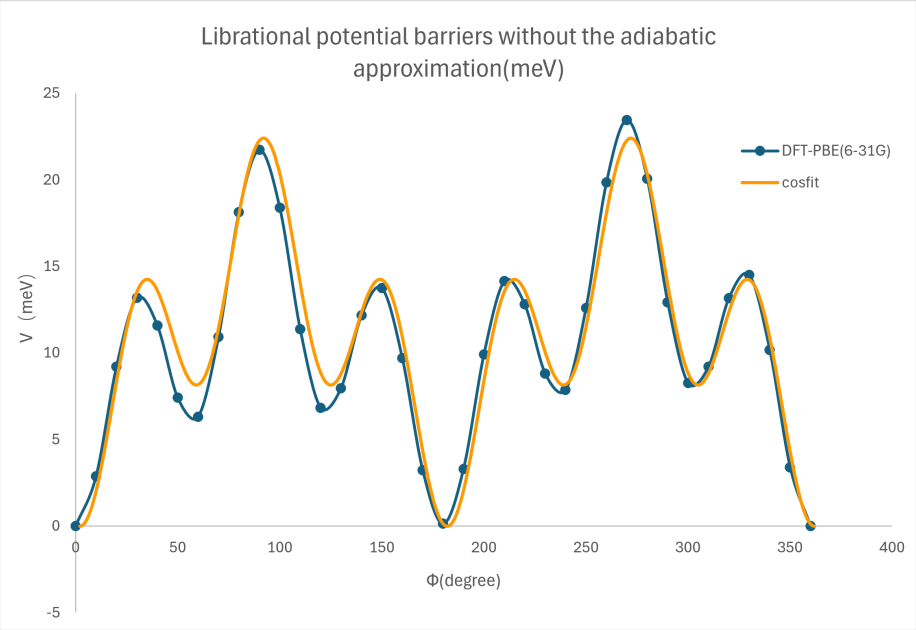


Figure 5.4: The potential well inside a single cavity of beryl is calculated in CP2K with the PBE functional and the 6-31(G) basis set.

with DFT. The pristine hexagonal crystal cells are cleaved and reconstructed using the Atomic Simulation Environment (ASE) package.[146] For the energy force calculation and potential well scan, we use the CP2K program with the `6-31(G)` basis set and the `PBE` exchange-correlation (XC) functional. The relaxation and energy convergence behaviors of the *HexVacancy* system can be monitored in real time via continuous output logs.

The energy profile landscape shown in Fig. 5.4 features non-equivalent periodic wells separated by a primary global barrier (maximum barrier height around 16.1 cm^{-1}) and a secondary local barrier at about 10 cm^{-1}. DFT calculations of water-beryl display a strong field created by the beryllium and aluminum (the electrostatic interactions formed by the silicon-oxygen framework were neglected). According to the Fourier transform, the Free Induction Decay (FID) signal intensity ($I(\alpha)$) of the entire doublet-of-triplets system can be written as the superposition of the two signals.

$$I(\alpha) \propto -\cos(3\alpha) - \cos(\alpha) + 2 \tag{5.6}$$

In channels like those in beryl, α is the rotation angle of the water molecule within the plane in which it lies. The confined molecule is not in a void of space, but rather conforms to the host lattice constraint and the axial local-field anisotropy. As mentioned in previous chapters, beryl exhibits $\mathbb{Z}_6$ (hexagonal) rotational symmetry. When a water molecule faces the cross-section of a channel, if it were a perfectly symmetrical molecule (such as water simplified to a single dipole), it would experience a V_6 (hexagonal) symmetry. However, the water molecule is actually an asymmetric triangle (with C_{2v} symmetry). When a C_{2v} water molecule is placed in a $\mathbb{Z}_6$ channel, because the two hydrogen atoms and one oxygen atom of the water molecule alternately form hydrogen bonds (attraction) and electrostatic repulsion with the oxygen atoms on the channel walls as they rotate, the periodicity of its lowest energy state is often reduced from six-fold to three-fold symmetry. This is the physical origin of the $-\cos(3\alpha)$ term, the localized potential well imparted by the lattice. In addition, $\cos(\alpha)$ typically represents the anisotropic local field generated by neighboring charges (or neighboring water dipole moments). Assume that a charge-balancing Na^+ ion is located somewhere deep within the channel, or that water molecules on adjacent lattice sites have spontaneously broken their symmetry to point in a specific direction. It remains to be investigated how the long-range dipole field they generate will interact with the water molecule at the current location, thereby forming a tilted onefold potential field of $-\cos(\alpha)$. The underlying cause of this symmetry breaking remains to be further investigated, as well as the finite size scaling in the bulk beryl crystal. For future work, we want to apply the proposed grid method and more advanced algorithms to study confined species such as water in nanotubes or in a C_{60} fullerene cage.[147] Intermolecular forces should be considered to simulate the motion and orientation of water molecules in a nanotube.

References

[1] Y Finkelstein, R Moreh, SL Shang, Y Wang, and ZK Liu. Quantum behavior of water nano-confined in beryl. *J. Chem. Phys.*, 146:124307, 2017.

[2] Boris P Gorshunov, Elena S Zhukova, Victor I Torgashev, Vladimir V Lebedev, Gil'man S Shakurov, Reinhard K Kremer, Efim V Pestrjakov, Victor G Thomas, Dimitry A Fursenko, and Martin Dressel. Quantum behavior of water molecules confined to nanocavities in gemstones. *J. Phys. Chem. Lett.*, 4:2015–2020, 2013.

[3] BP Gorshunov, VI Torgashev, ES Zhukova, VG Thomas, MA Belyanchikov, C Kadlec, F Kadlec, M Savinov, T Ostapchuk, J Petzelt, et al. Incipient ferroelectricity of water molecules confined to nano-channels of beryl. *Nat. Commun.*, 7:12842, 2016.

[4] MA Belyanchikov, ZV Bedran, M Savinov, P Bednyakov, P Proschek, J Prokleska, VA Abalmasov, ES Zhukova, VG Thomas, A Dudka, et al. Single-particle and collective excitations of polar water molecules confined in nano-pores within a cordierite crystal lattice. *Phys. Chem. Chem. Phys.*, 24:6890–6904, 2022.

[5] Chuanfu Luo, Wei Fa, Jian Zhou, Jinming Dong, and Xiao Cheng Zeng. Ferroelectric ordering in ice nanotubes confined in carbon nanotubes. *Nano Lett.*, 8:2607–2612, 2008.

[6] Elena S Zhukova, Victor I Torgashev, Boris P Gorshunov, Vladimir V Lebedev, Gil'man S Shakurov, Reinhard K Kremer, Efim V Pestrjakov, Victor G Thomas,

Dimitry A Fursenko, Anatoly S Prokhorov, et al. Vibrational states of a water molecule in a nano-cavity of beryl crystal lattice. *J. Chem. Phys.*, 140:224317, 2014.

[7] Martin Dressel, Elena S Zhukova, Victor G Thomas, and Boris P Gorshunov. Quantum electric dipole lattice: water molecules confined to nanocavities in beryl. *J. Infrared Millim. Terahertz Waves*, 39:799–815, 2018.

[8] Gerhard Hummer, Jayendran C Rasaiah, and Jerzy P Noworyta. Water conduction through the hydrophobic channel of a carbon nanotube. *Nature*, 414(6860):188–190, 2001.

[9] Tobias Serwatka and Pierre-Nicholas Roy. Ferroelectric water chains in carbon nanotubes: Creation and manipulation of ordered quantum phases. *J. Chem. Phys.*, 157:234301, 2022.

[10] Hai-Xia Zhao, Xiang-Jian Kong, Hui Li, Yi-Chang Jin, La-Sheng Long, Xiao Cheng Zeng, Rong-Bin Huang, and Lan-Sun Zheng. Transition from one-dimensional water to ferroelectric ice within a supramolecular architecture. *Proc. Natl. Acad. Sci. U.S.A.*, 108:3481–3486, 2011.

[11] Wen-Hui Zhao, Jaeil Bai, Lan-Feng Yuan, Jinlong Yang, and Xiao Cheng Zeng. Ferroelectric hexagonal and rhombic monolayer ice phases. *Chem. Sci.*, 5:1757–1764, 2014.

[12] Xuedan Ma, Sofie Cambré, Wim Wenseleers, Stephen K Doorn, and Han Htoon. Quasiphase transition in a single file of water molecules encapsulated in (6, 5) carbon nanotubes observed by temperature-dependent photoluminescence spectroscopy. *Phys. Rev. Lett.*, 118:027402, 2017.

[13] J. HernandeZ J. Calvo and Gomez Llorente J.M. Confinement effects on water clusters inside carbon nanotubes. *J. Phys. Chem. C*, 116(17019-17028):10, 2012.

[14] J Holakovskỳ. A new type of the ferroelectric phase transition. *Phys. Status Solidi B*, 56:615–619, 1973.

[15] Kei Kurotobi and Yasujiro Murata. A single molecule of water encapsulated in fullerene c60. *Science*, 333:613–616, 2011.

[16] Horsewill Anthony. Symmetry-breaking in the endofullerene $h_2o@c_{60}$ revealed in the quantum dynamics of ortho and para-water: a neutron scattering investigation. *Phys. Chem. Chem. Phys.*, 2014.

[17] Peter M Felker and Zlatko Bačić. Accurate quantum calculations of translation-rotation eigenstates in electric-dipole-coupled h2o@ c60 assemblies. *Chem. Phys. Lett.*, 683:172–178, 2017.

[18] Yulia N Kalugina and Pierre-Nicholas Roy. Potential energy and dipole moment surfaces for hf@ c60: Prediction of spectral and electric response properties. *J. Chem. Phys.*, 147:244303, 2017.

[19] Tom Halverson, Dmitri Iouchtchenko, and Pierre-Nicholas Roy. Quantifying entanglement of rotor chains using basis truncation: Application to dipolar endofullerene peapods. *J. Chem. Phys.*, 148:074112, 2018.

[20] Clément Wespiser, Thomas Putaud, Yulia Kalugina, Armand Soldera, Pierre-Nicholas Roy, Xavier Michaut, and Patrick Ayotte. Ro-translational dynamics of confined water. i. the confined asymmetric rotor model. *J. Chem. Phys.*, 156:074304, 2022.

[21] Tobias Serwatka, Spencer Yim, Patrick Ayotte, and Pierre-Nicholas Roy. On the nature of the schottky anomaly in endohedral water. *J. Chem. Phys.*, 158(12), 2023.

[22] T Putaud, J-C Chartrand, Y Kalugina, X Michaut, P-N Roy, and P Ayotte. A simple confined rotor model to describe the ro-translational dynamics of water endofullerenes and to assign the ro-vibrational spectra of solid h2o@ c60. *J. Chem. Phys.*, 162(14), 2025.

[23] Kevin P Bishop and Pierre-Nicholas Roy. Quantum mechanical free energy profiles with post-quantization restraints: Binding free energy of the water dimer over a broad range of temperatures. *J. Chem. Phys.*, 148(10), 2018.

[24] Dmitri Iouchtchenko, Kevin P Bishop, and Pierre-Nicholas Roy. The quantum mechanical potential of mean force: density matrix formulation, estimators, and constrained path integral molecular dynamics integrators. *Mol. Phys.*, 124(9-10):e2577825, 2026.

[25] CJ Burnham, GF Reiter, J Mayers, T Abdul-Redah, H Reichert, and H Dosch. On the origin of the redshift of the oh stretch in ice ih: Evidence from the momentum distribution of the protons and the infrared spectral density. *Phys. Chem. Chem. Phys.*, 8(34):3966–3977, 2006.

[26] Joseph A Morrone, Varadharajan Srinivasan, Daniel Sebastiani, and Roberto Car. Proton momentum distribution in water: an open path integral molecular dynamics study. *J. Chem. Phys.*, 126(23), 2007.

[27] Joseph A Morrone and Roberto Car. Nuclear quantum effects in water. *Phys. Rev. Lett.*, 101(1):017801, 2008.

[28] Ross H McKenzie, Christiaan Bekker, Bijyalaxmi Athokpam, and Sai G Ramesh. Effect of quantum nuclear motion on hydrogen bonding. *J. Chem. Phys.*, 140(17), 2014.

[29] Thomas E Markland and Michele Ceriotti. Nuclear quantum effects enter the mainstream. *Nat. Rev. Chem.*, 2(3):0109, 2018.

[30] Müser M. H. Marx D. Path integral simulations of rotors: theory and applications. *J. Phys.: Condens. Matter*, 11(117-155):118, 1998.

[31] Tapas Sahoo, Dmitri Iouchtchenko, CM Herdman, and Pierre-Nicholas Roy. A path integral ground state replica trick approach for the computation of entanglement entropy of dipolar linear rotors. *J. Chem. Phys.*, 152:184113, 2020.

[32] Tapas Sahoo and Gautam Gangopadhyay. Effect of neighbouring molecules on ground-state properties of many-body polar linear rotor systems. *Mol. Phys.*, page e2242967, 2023.

[33] Tobias Serwatka and Pierre-Nicholas Roy. Ground state of asymmetric tops with dmrg: Water in one dimension. *J. Chem. Phys.*, 156:044116, 2022.

[34] Tobias Serwatka and Pierre-Nicholas Roy. Quantum criticality and universal behavior in molecular dipolar lattices of endofullerenes. *J. Phys. Chem. Lett.*, 14:5586–5591, 2023.

[35] T. Serwatka, R. G. Melko, A. Burkov, and P.-N. Roy. Quantum phase transition in the one-dimensional water chain. *Phys. Rev. Lett.*, 130:026201, Jan 2023.

[36] Tobias Serwatka and Pierre-Nicholas Roy. Quantum criticality and universal behavior in molecular dipolar lattices of endofullerenes. *J. Phys. Chem. Lett.*, 14:5586–5591, 2023.

[37] Tobias Serwatka and Pierre-Nicholas Roy. Optimized basis sets for dmrg calculations of quantum chains of rotating water molecules. *J. Chem. Phys.*, 158(21), 2023.

[38] Tobias Serwatka and Pierre-Nicholas Roy. Ground states of planar dipolar rotor chains with recurrent neural networks. *J. Chem. Phys.*, 160:224103, 2024.

[39] BP Abolins, RE Zillich, and KB Whaley. A ground state monte carlo approach for studies of dipolar systems with rotational degrees of freedom. *J. Low Temp. Phys.*, 165:249–260, 2011.

[40] BP Abolins, RE Zillich, and KB Whaley. Erratum to: A ground state monte carlo approach for studies of dipolar systems with rotational degrees of freedom. *J. Low Temp. Phys.*, 170:131–131, 2013.

[41] Brendan P Abolins, Robert E Zillich, and K Birgitta Whaley. Quantum phases of dipolar rotors on two-dimensional lattices. *J. Chem. Phys.*, 148:102338, 2018.

[42] Tapas Sahoo, Tobias Serwatka, and Pierre-Nicholas Roy. A path integral ground state approach for asymmetric top rotors with nuclear spin symmetry: Application to water chains. *J. Chem. Phys.*, 154:244305, 2021.

[43] YT Chan, E Uykur, MA Belyanchikov, M Dressel, VA Abalmasov, V Thomas, ES Zhukova, and B Gorshunov. Effect of hydrostatic pressure on the quantum paraelectric state of dipolar coupled water molecular network. *Phys. Rev. Res.*, 4:023205, 2022.

[44] Donald A. McQuarrie. *Quantum Chemistry-2nd ed.* UNIVERSITY SCIENCE BOOKS, 2008.

[45] Alexander I Kolesnikov, George F Reiter, Narayani Choudhury, Timothy R Prisk, Eugene Mamontov, Andrey Podlesnyak, George Ehlers, Andrew G Seel, David J Wesolowski, and Lawrence M Anovitz. Quantum tunneling of water in beryl: a new state of the water molecule. *Phys. Rev. Lett.*, 116:167802, 2016.

[46] Estêvão VB de Oliveira, Muhammad Shaeer Moeed, and Pierre-Nicholas Roy. Path integral monte carlo in the angular momentum basis for a chain of planar rotors. *J. Chem. Phys.*, 163:144112, 2025.

[47] Sam McArdle, Suguru Endo, Alán Aspuru-Guzik, Simon C Benjamin, and Xiao Yuan. Quantum computational chemistry. *Rev. Mod. Phys.*, 92(1):015003, 2020.

[48] Cornelius Lanczos. An iteration method for the solution of the eigenvalue problem of linear differential and integral operators. *J. Res. Natl. Bur. Stand.*, 45:255–282, 1950.

[49] Jane K Cullum and Ralph A Willoughby. *Lanczos algorithms for large symmetric eigenvalue computations: Vol. I: Theory*. SIAM, 2002.

[50] Richard B Lehoucq, Danny C Sorensen, and Chao Yang. *ARPACK users' guide: solution of large-scale eigenvalue problems with implicitly restarted Arnoldi methods*. SIAM, 1998.

[51] Dmitri Iouchtchenko and Pierre-Nicholas Roy. Ground states of linear rotor chains via the density matrix renormalization group. *J. Chem. Phys.*, 148:134115, 2018.

[52] Samrit Mainali, Fabien Gatti, Dmitri Iouchtchenko, Pierre-Nicholas Roy, and Hans-Dieter Meyer. Comparison of the multi-layer multi-configuration time-dependent

hartree (ml-mctdh) method and the density matrix renormalization group (dmrg) for ground state properties of linear rotor chains. *J. Chem. Phys.*, 154:174106, 2021.

[53] Dan Kalman. A singularly valuable decomposition: the svd of a matrix. *Coll. Math. J.*, 27(1):2–23, 1996.

[54] Jacob Eisenstein. *Introduction to natural language processing*. MIT press, 2019.

[55] James B Anderson. A random-walk simulation of the schrödinger equation: H+ 3. *J. Chem. Phys.*, 63(4):1499–1503, 1975.

[56] Jonathon K Gregory and David C Clary. Calculations of the tunneling splittings in water dimer and trimer using diffusion monte carlo. *J. Chem. Phys.*, 102(20):7817–7829, 1995.

[57] David M Ceperley. Path integrals in the theory of condensed helium. *Rev. Mod. Phys.*, 67:279–355, 1995.

[58] Nicholas V Blinov, Pierre-Nicholas Roy, and Gregory A Voth. Path integral formulation of centroid dynamics for systems obeying bose–einstein statistics. *J. Chem. Phys.*, 115(10):4484–4495, 2001.

[59] Nicholas Blinov and Pierre-Nicholas Roy. Operator formulation of centroid dynamics for bose–einstein and fermi–dirac statistics. *J. Chem. Phys.*, 115(17):7822–7831, 2001.

[60] Nicholas Blinov and Pierre-Nicholas Roy. Connection between the observable and centroid structural properties of a quantum fluid: Application to liquid para-hydrogen. *J. Chem. Phys.*, 120(8):3759–3764, 2004.

[61] Nicholas Blinov, XiaoGeng Song, and Pierre-Nicholas Roy. Path integral monte carlo approach for weakly bound van der waals complexes with rotations: Algorithm and benchmark calculations. *J. Chem. Phys.*, 120(13):5916–5931, 2004.

[62] Saverio Moroni, Nicholas Blinov, and Pierre-Nicholas Roy. Quantum monte carlo study of helium clusters doped with nitrous oxide: Quantum solvation and rotational dynamics. *J. Chem. Phys.*, 121(8):3577–3581, 2004.

[63] W Topic, W Jäger, N Blinov, P-N Roy, M Botti, and Saverio Moroni. Rotational spectrum of cyanoacetylene solvated with helium atoms. *J. Chem. Phys.*, 125(14):144310, 2006.

[64] Yunjie Xu, Nicholas Blinov, Wolfgang Jäger, and Pierre-Nicholas Roy. Recurrences in rotational dynamics and experimental measurement of superfluidity in doped helium clusters. *J. Chem. Phys.*, 124(8), 2006.

[65] Zheng Li, Lecheng Wang, Hong Ran, Daiqian Xie, N Blinov, P-N Roy, and Hua Guo. Path integral monte carlo study of co2 solvation in he4 clusters. *J. Chem. Phys.*, 128:224513, 2008.

[66] Hui Li, Nicholas Blinov, Pierre-Nicholas Roy, and Robert J Le Roy. Path-integral monte carlo simulation of $\nu 3$ vibrational shifts for co2 in (he) n clusters critically tests the he–co2 potential energy surface. *J. Chem. Phys.*, 130(14), 2009.

[67] Hui Li, Robert J Le Roy, Pierre-Nicholas Roy, and ARW McKellar. Molecular superfluid: Nonclassical rotations in doped para-hydrogen clusters. *Phys. Rev. Lett.*, 105:133401, 2010.

[68] Lecheng Wang, Daiqian Xie, Hua Guo, Hui Li, Robert J Le Roy, and Pierre-Nicholas Roy. Superfluid response of 4hen–n2o clusters probed by path integral monte carlo simulations. *J. Mol. Spectrosc.*, 267(1-2):136–143, 2011.

[69] Tao Zeng, Hui Li, and Pierre-Nicholas Roy. Simulating asymmetric top impurities in superfluid clusters: A para-water dopant in para-hydrogen. *J. Phys. Chem. Lett.*, 4(1):18–22, 2013.

[70] Tao Zeng, Grégoire Guillon, Joshua T Cantin, and Pierre-Nicholas Roy. Probing the superfluid response of para-hydrogen with a sulfur dioxide dopant. *J. Phys. Chem. Lett.*, 4(14):2391–2396, 2013.

[71] Tao Zeng and Pierre-Nicholas Roy. Microscopic molecular superfluid response: theory and simulations. *Rep. Prog. Phys.*, 77:046601, 2014.

[72] Tao Zeng, Nicholas Blinov, Grégoire Guillon, Hui Li, Kevin P Bishop, and Pierre-Nicholas Roy. Moribs-pimc: A program to simulate molecular rotors in bosonic solvents using path-integral monte carlo. *Comput. Phys. Commun.*, 204:170–188, 2016.

[73] Hui Li, Xiao-Long Zhang, Tao Zeng, Robert J Le Roy, and Pierre-Nicholas Roy. Suppression of parahydrogen superfluidity in a doped nanoscale bose fluid mixture. *Phys. Rev. Lett.*, 123(9):093001, 2019.

[74] Alexander Ibrahim, Lecheng Wang, Tom Halverson, Robert J Le Roy, and Pierre-Nicholas Roy. Equation of state and first principles prediction of the vibrational matrix shift of solid parahydrogen. *J. Chem. Phys.*, 151(24), 2019.

[75] Alexander Ibrahim and Pierre-Nicholas Roy. Equation of state of solid parahydrogen using ab initio two-body and three-body interaction potentials. *J. Chem. Phys.*, 157(17), 2022.

[76] Alexander Ibrahim and Pierre-Nicholas Roy. Three-body potential energy surface for para-hydrogen. *J. Chem. Phys.*, 156(4):044301, 2022.

[77] Alexander Ibrahim and Pierre-Nicholas Roy. A neural network-based four-body potential energy surface for parahydrogen. *J. Chem. Phys.*, 160(24), 2024.

[78] Alexander Ibrahim and Pierre-Nicholas Roy. Path-integral monte carlo simulations of solid parahydrogen using two-body, three-body, and four-body ab initio interaction potential energy surfaces. *J. Chem. Phys.*, 162(16), 2025.

[79] CM Herdman, P-N Roy, RG Melko, and A Del Maestro. Particle entanglement in continuum many-body systems via quantum monte carlo. *Phys. Rev. B*, 89(14):140501, 2014.

[80] C.M. Herdman, Stephen Inglis, P.-N. Roy, R. G. Melko, and A. Del Maestro. Path-integral monte carlo method for rényi entanglement entropies. *Phys. Rev. E*, 90:013308, 2014.

[81] Dmitri Iouchtchenko and Pierre-Nicholas Roy. Estimating ground state entanglement entropy using path integral molecular dynamics. In *Recent Progress in Quantum Monte Carlo*, pages 145–154. American Chemical Society, 2016.

[82] CM Herdman, P-N Roy, RG Melko, and A Del Maestro. Spatial entanglement entropy in the ground state of the lieb-liniger model. *Phys. Rev. B*, 94(6):064524, 2016.

[83] CM Herdman, P-N Roy, RG Melko, and A Del Maestro. Entanglement area law in superfluid 4 he. *Nat. Phys.*, 13(6):556–558, 2017.

[84] A Sarsa, KE Schmidt, and WR Magro. A path integral ground state method. *J. Chem. Phys.*, 113(4):1366–1371, 2000.

[85] Javier E Cuervo, Pierre-Nicholas Roy, and Massimo Boninsegni. Path integral ground state with a fourth-order propagator: Application to condensed helium. *J. Chem. Phys.*, 122(11), 2005.

[86] Javier Eduardo Cuervo and Pierre-Nicholas Roy. Path integral ground state study of finite-size systems: Application to small (parahydrogen) n (n= 2–20) clusters. *J. Chem. Phys.*, 125:124314, 2006.

[87] Javier Eduardo Cuervo and Pierre-Nicholas Roy. On the solid-and liquidlike nature of quantum clusters in their ground state. *J. Chem. Phys.*, 128(22), 2008.

[88] Javier Eduardo Cuervo and Pierre-Nicholas Roy. Weakly bound complexes trapped in quantum matrices: Structure, energetics, and isomer coexistence in (para-h2) n (ortho-d2) 3 clusters. *J. Chem. Phys.*, 131(11), 2009.

[89] Steve Constable, Matthew Schmidt, Christopher Ing, Tao Zeng, and Pierre-Nicholas Roy. Langevin equation path integral ground state. *J. Phys. Chem. A*, 117(32):7461–7467, 2013.

[90] Nabil Faruk, Matthew Schmidt, Hui Li, Robert J Le Roy, and Pierre-Nicholas Roy. First-principles prediction of the raman shifts in parahydrogen clusters. *J. Chem. Phys.*, 141(1), 2014.

[91] Matthew Schmidt, Steve Constable, Pierre-Nicholas Roy, et al. Inclusion of trial functions in the langevin equation path integral ground state method: Application to parahydrogen clusters and their isotopologues. *J. Chem. Phys.*, 140(23), 2014.

[92] Matthew Schmidt, José M Fernández, Nabil Faruk, Marcel Nooijen, Robert J Le Roy, Juan H Morilla, Guzmán Tejeda, Salvador Montero, and Pierre-Nicholas Roy. Raman vibrational shifts of small clusters of hydrogen isotopologues. *J. Phys. Chem. A*, 119(50):12551–12561, 2015.

[93] Matthew Schmidt and Pierre-Nicholas Roy. Path integral molecular dynamic simulation of flexible molecular systems in their ground state: Application to the water dimer. *J. Chem. Phys.*, 148(12), 2018.

[94] Matthew Schmidt and Pierre-Nicholas Roy. On the accuracy and efficiency of different methods to calculate raman vibrational shifts of parahydrogen clusters. *J. Chem. Phys.*, 156(8), 2022.

[95] Matthew Schmidt and Pierre-Nicholas Roy. Ground state chemical potential of parahydrogen clusters of size n= 21–40. *J. Chem. Phys.*, 156(1), 2022.

[96] Wenxue Zhang, Muhammad Shaeer Moeed, Andrew Bright, Tobias Serwatka, Estevao De Oliveira, and Pierre-Nicholas Roy. Path integral monte carlo in a discrete variable representation with gibbs sampling: Dipolar planar rotor chain. *J. Chem. Phys.*, 162:014106, 2025.

[97] Elena S Zhukova, Mikhail A Belyanchikov, Maxim Savinov, Peter Bednyakov, Jan Prokleška, Stanislav Kamba, Zakhar V Bedran, Victor G Thomas, Victor I Torgashev, Ece Uykur, et al. Quantum critical behavior of nanoconfined water molecules. In *2019 44th International Conference on Infrared, Millimeter, and Terahertz Waves (IRMMW-THz)*, pages 1–2. IEEE, 2019.

[98] MA Belyanchikov, M Savinov, ZV Bedran, P Bednyakov, P Proschek, J Prokleska, VA Abalmasov, J Petzelt, ES Zhukova, VG Thomas, et al. Dielectric ordering of water molecules arranged in a dipolar lattice. *Nat. Commun.*, 11:3927, 2020.

[99] Tobias Serwatka and Pierre-Nicholas Roy. Quantum criticality in chains of planar rotors with dipolar interactions. *J. Chem. Phys.*, 160:104302, 2024.

[100] Ulrich Schollwöck. The density-matrix renormalization group in the age of matrix product states. *Ann. Phys.*, 326:96–192, 2011.

[101] Steven R White. Density matrix formulation for quantum renormalization groups. *Phys. Rev. Lett.*, 69:2863–2866, 1992.

[102] J. A. Barker. A quantum-statistical Monte Carlo method; path integrals with boundary conditions. *J. Chem. Phys.*, 70:2914–2918, 03 1979.

[103] Dominik Marx and Martin H Müser. Path integral simulations of rotors: theory and applications. *J. Phys.: Condens. Matter*, 11:R117, 1999.

[104] JC Light, IP Hamilton, and JV Lill. Generalized discrete variable approximation in quantum mechanics. *J. Chem. Phys.*, 82:1400–1409, 1985.

[105] John C Light and Tucker Carrington Jr. Discrete-variable representations and their utilization. *Adv. Chem. Phys.*, 114:263–310, 2000.

[106] Yingsheng Xiao and Bill Poirier. Using discrete variable representation path integral monte carlo with metropolis sampling to compute ground state wavefunctions. *J. Theor. Comput. Chem.*, 6:309–321, 2007.

[107] Yingsheng Xiao. *Efficient full quantum calculations for small molecules using novel phase space optimized discrete variable representation path integral Monte Carlo Methods*. PhD thesis, Texas Tech University, 2007.

[108] Nancy Makri. Improved feynman propagators on a grid and non-adiabatic corrections within the path integral framework. *Chem. Phys. Lett.*, 193:435–445, 1992.

[109] Maria Topaler and Nancy Makri. Quasi-adiabatic propagator path integral methods. exact quantum rate constants for condensed phase reactions. *Chem. Phys. Lett.*, 210:285–293, 1993.

[110] Maria Topaler and Nancy Makri. System-specific discrete variable representations for path integral calculations with quasi-adiabatic propagators. *Chem. Phys. Lett.*, 210:448–457, 1993.

[111] Maria Topaler and Nancy Makri. Quantum rates for a double well coupled to a dissipative bath: Accurate path integral results and comparison with approximate theories. *J. Chem. Phys.*, 101:7500–7519, 1994.

[112] Nancy Makri. Numerical path integral techniques for long time dynamics of quantum dissipative systems. *J. Math. Phys.*, 36:2430–2457, 1995.

[113] Nancy Makri. Communication: Modular path integral: Quantum dynamics via sequential necklace linking. *J. Chem. Phys.*, 148:101101, 2018.

[114] Nancy Makri. Modular path integral methodology for real-time quantum dynamics. *J. Chem. Phys.*, 149:214108, 2018.

[115] Stuart Geman and Donald Geman. Stochastic relaxation, gibbs distributions, and the bayesian restoration of images. *IEEE Trans. Pattern Anal. Mach. Intell.*, PAMI-6:721–741, 1984.

[116] Alan E. Gelfand and Adrian F. M. Smith. Sampling-based approaches to calculating marginal densities. *J. Am. Stat. Assoc.*, 85:398–409, 1990.

[117] Antonio Sarsa, Kevin E. Schmidt, and William R. Magro. A path integral ground state method. *J. Chem. Phys.*, 113:1366, 2000.

[118] Daniel T Colbert and William H Miller. A novel discrete variable representation for quantum mechanical reactive scattering via the s-matrix kohn method. *J. Chem. Phys.*, 96:1982–1991, 1992.

[119] Vasilios I. Manousiouthakis and Michael W. Deem. Strict detailed balance is unnecessary in monte carlo simulation. *J. Chem. Phys.*, 110:2753, 1999.

[120] Fahim Faizi, George Deligiannidis, and Edina Rosta. Efficient irreversible monte carlo samplers. *J. Chem. Theory Comput.*, 16:2124, 2020.

[121] Matthew Fishman, Steven White, and Edwin Stoudenmire. The itensor software library for tensor network calculations. *SciPost Phys. Codebases*, page 004, 2022.

[122] Devarajan Thirumalai, Eric J. Bruskin, and Bruce J. Berne. An iterative scheme for the evaluation of discretized path integrals. *J. Chem. Phys.*, 79:5063–5069, 11 1983.

[123] Antonín Klíč, Václav Janiš, and Filip Kadlec. Orientational ordering of water molecules confined in beryl: A theoretical study. *Phys. Rev. B*, 108:064101, 2023.

[124] Lawrence M Anovitz, Eugene Mamontov, Paul ben Ishai, and Alexander I Kolesnikov. Anisotropic dynamics of water ultraconfined in macroscopically oriented channels of single-crystal beryl: A multifrequency analysis. *Phys. Rev. E*, 88:052306, 2013.

[125] Boris P. Gorshunov, Elena S. Zhukova, Victor I. Torgashev, Elizaveta A. Motovilova, Vladimir V. Lebedev, Anatoly S. Prokhorov, Gil'man S. Shakurov, Reinhard K. Kremer, Vladimir V. Uskov, Efim V. Pestrjakov, Victor G. Thomas, Dimitri A. Fursenko, Christelle Kadlec, Filip Kadlec, and Martin Dressel. Thz–ir spectroscopy of single h2o molecules confined in nanocage of beryl crystal lattice. *Phase Transit.*, 87:966–972, 2014.

[126] BA Kolesov and CA Geiger. The orientation and vibrational states of h2o in synthetic alkali-free beryl. *Phys. Chem. Miner.*, 27:557–564, 2000.

[127] Boris Kolesov. Vibrational states of h2o in beryl: Physical aspects. *Phys. Chem. Miner.*, 35:271–278, 2008.

[128] A Barati Farimani, Yanbin Wu, and NR Aluru. Rotational motion of a single water molecule in a buckyball. *Phys. Chem. Chem. Phys.*, 15:17993–18000, 2013.

[129] Muhammad Shaeer Moeed, Tobias Serwatka, and Pierre-Nicholas Roy. Pair approximating the action for molecular rotations in path integral monte carlo. *J. Chem. Phys.*, 162:024113, 01 2025.

[130] Kurt Binder. Finite size scaling analysis of ising model block distribution functions. *Z. Phys. B: Condens. Matter*, 43:119–140, 1981.

[131] Kurt Binder. Critical properties from monte carlo coarse graining and renormalization. *Phys. Rev. Lett.*, 47:693–696, 1981.

[132] Pasquale Calabrese and John Cardy. Entanglement entropy and quantum field theory. *J. Stat. Mech.: Theory Exp.*, 2004:P06002, 2004.

[133] Luigi Amico, Rosario Fazio, Andreas Osterloh, and Vlatko Vedral. Entanglement in many-body systems. *Rev. Mod. Phys.*, 80:517–576, 2008.

[134] Jens Eisert, Marcus Cramer, and Martin B Plenio. Colloquium: Area laws for the entanglement entropy. *Rev. Mod. Phys.*, 82:277–306, 2010.

[135] Subir Sachdev. *Quantum Phase Transitions*. Cambridge University Press, Cambridge, 2 edition, 2011.

[136] Peter M. Felker, Vojtěch Vlček, Isaac Hietanen, Stephen FitzGerald, Daniel Neuhauser, and Zlatko Bačić. Explaining the symmetry breaking observed in the endofullerenes h2c60, hfc60, and h2oc60. *Phys. Chem. Chem. Phys.*, 19:31274–31283, 2017.

[137] Hal Suzuki, Motohiro Nakano, Yoshifumi Hashikawa, and Yasujiro Murata. Rotational motion and nuclear spin interconversion of h2o encapsulated in c60 appearing in the low-temperature heat capacity. *J. Phys. Chem. Lett.*, 10:1306–1311, 2019.

[138] Shi-Peng Shen, Jia-Chuan Wu, Jun-Da Song, Xue-Feng Sun, Yi-Feng Yang, Yi-Sheng Chai, Da-Shan Shang, Shou-Guo Wang, James F Scott, and Young Sun. Quantum electric-dipole liquid on a triangular lattice. *Nat. Commun.*, 7:10569, 2016.

[139] Wenxue Zhang, Estevao De Oliveira, Muhammad Shaeer Moeed, Hui Li, and Pierre-Nicholas Roy. Quantum critical behavior in chains of hindered dipolar planar rotors. *arXiv preprint arXiv:XXXX.XXXXX*, 2026. Preprint; arXiv identifier to be assigned.

[140] Jorge V José, Leo P Kadanoff, Scott Kirkpatrick, and David R Nelson. Renormalization, vortices, and symmetry-breaking perturbations in the two-dimensional planar model. *Phys. Rev. B*, 16:1217–1241, 1977.

[141] John Michael Kosterlitz and David James Thouless. Ordering, metastability and phase transitions in two-dimensional systems. *J. Phys. C: Solid State Phys.*, 6:1181–1203, 1973.

[142] Sukhwinder Singh, Robert N. C. Pfeifer, and Guifre Vidal. Tensor network states and algorithms in the presence of a global u(1) symmetry. *Phys. Rev. B*, 83:115125, 2011.

[143] Muhammad Shaeer Moeed, James Brown, Alexander Ibrahim, Estêvão VB de Oliveira, and Pierre-Nicholas Roy. Qubit encodings for lattices of dipolar planar rotors. *J. Chem. Phys.*, 163:174103, 2025.

[144] Estêvão VB de Oliveira, Muhammad Shaeer Moeed, and Pierre-Nicholas Roy. Effective theory of quantum phases in the dipolar planar rotor chain. *J. Chem. Phys.*, 165(10), 2026.

[145] Thomas D Kühne, Marcella Iannuzzi, Mauro Del Ben, Vladimir V Rybkin, Patrick Seewald, Frederick Stein, Teodoro Laino, Rustam Z Khaliullin, Ole Schütt, Florian Schiffmann, et al. Cp2k: An electronic structure and molecular dynamics software package-quickstep: Efficient and accurate electronic structure calculations. *J. Chem. Phys.*, 152(19), 2020.

[146] Ask Hjorth Larsen, Jens Jørgen Mortensen, Jakob Blomqvist, Ivano E Castelli, Rune Christensen, Marcin Dułak, Jesper Friis, Michael N Groves, Bjørk Hammer, Cory Hargus, et al. The atomic simulation environment—a python library for working with atoms. *J. Phys.: Cond. Matt.*, 29(27):273002, 2017.

[147] J Hernández-Rojas, F Calvo, J Bretón, and JM Gomez Llorente. Confinement effects on water clusters inside carbon nanotubes. *J. Phys. Chem. C*, 116(32):17019–17028, 2012.